Department of Precision and Microsystems Engineering

Focusing of Ultrasound for Photo-Acoustic Subsurface Imaging in AFM Cantilever tip

Gourab Chakraborty

Report no	: 2022.037
Coach	: Dr. Gerard Verbiest
Professor	: Dr. Gerard Verbiest
Specialisation	: High-Tech Engineering
Type of report	: Msc Thesis Report
Date	: July 28, 2022

Focusing of Ultrasound for Photo-Acoustic Subsurface Imaging in AFM Cantilever tip

Msc Report

by:

Gourab Chakraborty

to obtain the degree of Master of Science
at the Delft University of Technology,
to be defended publicly on Wednesday August 10, 2022 at 1300 hours.

Student number:	5189950	
Project duration:	September 1, 2021 – August 31, 2022	
Thesis Supervisors:	Ruben Guis,	PME,TU Delft
	Dr. Martin Robin,	PME,TU Delft
	Dr. Gerard Verbiest,	PME,TU Delft
	Dr. Ir. Umit Arabul,	ASML
	Dr. Ir. Zili Zhou,	ASML

TU Delft ASML

Abstract

Over the past few years, sub-surface imaging techniques at nano-scale has become increasingly important in the semiconductor industry, whereby voids, cracks and other heterogenous features can be detected using disturbances in penetrating waves inside the substrate. The depth resolution that can be achieved with subsurface imaging techniques is set by the frequency or wavelength of the acoustic wave in the sample. A certain modality called photo-acoustic subsurface Atomic Force Microscopy (passAFM) which uses Picosecond Ultrasonics, is currently in development at the DMN group in TU Delft. Picosecond Ultrasonics is capable of generating and detecting of acoustic waves in Si samples at 100 nm depth resolution. However the requirement of aiming the acoustic waves inside a Si cantilever tip to obtain a lateral resolution of the order of wavelength makes the reflected acoustic signal too weak to detect. This necessitates focusing these waves within a spot width of a few hundreds of nm inside the tip. In this research, we improved the passAFM setup to detect acoustic waves with higher Signal-to-Noise Ratio on the AFM cantilever body. Consequently we expect to detect a signal at the tip by truncating it upto 11 μm without focusing, since the acoustic echoes are reflected from a larger tip area (3.3-3.6 μm tip size). For focusing at narrower tip areas, we design diffractive metasurfaces like Fresnel Zonal Plate (FZP) layers on the AFM cantilever tip. We estimate a gain factor upto 5-6 in the detected acoustic signal by focusing with conventional FZPs on larger truncated tips of 15.5 μm (800nm tip size). With Focused Ion Beam (FIB) milling, we truncate the AFM tips and fabricate FZP structures on the cantilever body and tip. We use the designs on the body to experimentally study the effect of focusing and verify the numerical results, and on the tip to study the gain in signal due to focusing capabilities of the FZP. Furthermore we discovered that the losses in the acoustic echoes inside the cantilever body not only comes from the ultrasonic damping in Si, but also due to the imperfect adhesion at the interface between the Si layer and the metal coating of the AFM cantilever. The latter effect induces an additional loss factor of roughly 24% with every round trip of the acoustic echo on the cantilever body, but because there is only one round trip on the tip, the transmission loss at the interface will take place only once there. Hence we can expect to detect almost 2 times higher signal on the tip than we calculate from the measured echoes on the cantilever body.

Contents

1 Introduction **1**
- 1.1 Subsurface imaging . . . 1
- 1.2 State of the Art . . . 3
- 1.3 Research Questions and Planning . . . 4
  - 1.3.1 Knowledge Gap . . . 4
  - 1.3.2 Research Questions . . . 4
  - 1.3.3 Planning for design, fabrication and experiments . . . 4

2 Theoretical Modelling and Calculations **7**
- 2.1 Fresnel Zonal Plate Design . . . 7
- 2.2 Focusing Parameters and Analogy with Optics . . . 8
- 2.3 Designing FZP on truncated AFM tips . . . 10
- 2.4 Modeling on Cantilever body and tip . . . 13
  - 2.4.1 First echo amplitude at the tip without FZP . . . 14
- 2.5 Simulation Results and Analysis . . . 15
  - 2.5.1 Signal Variation on Cantilever Body . . . 15
  - 2.5.2 Signal variation at the tip . . . 18

3 Fabrication **25**
- 3.1 Fabrication Process . . . 25
- 3.2 Parameter Settings for Focused Ion Beam . . . 26
  - 3.2.1 Dose tests on cantilever tip . . . 26
  - 3.2.2 Fabricating first FZP patterns . . . 28
- 3.3 Designing on AFM Cantilever body and tip . . . 28
  - 3.3.1 Fabricating FZPs on AFM Cantilever Body . . . 30
  - 3.3.2 Fabrication on AFM tips . . . 31

4 Experimental Methods **37**
- 4.1 Setup Description . . . 37
  - 4.1.1 Photo Induced Generation of Bulk Acoustic Waves . . . 37
  - 4.1.2 Detection using Beam Distortion Detection and Conoscopic Interferometry . . . 37
  - 4.1.3 Setup Configuration . . . 38
  - 4.1.4 Electronics . . . 39
- 4.2 Modification of Experimental Setup . . . 39
  - 4.2.1 Changing the setup configuration . . . 39
  - 4.2.2 Unamplified Photodetector . . . 42
  - 4.2.3 Pump-probe Alignment on FZP . . . 44
- 4.3 Data Analysis . . . 45
  - 4.3.1 Fitting of Acoustic Echoes . . . 45
  - 4.3.2 Error Analysis . . . 47

5 Experimental Results **49**
- 5.1 Measurements on Cantilever Body . . . 49
- 5.2 Measuring signals Near the tip . . . 54
- 5.3 Signal Attenuation in AFM Cantilever . . . 55

6 Discussions and Outlook **59**
- 6.1 Discrepancies in measurement and simulation on the cantilever body . . . 59
- 6.2 Expected signal from the tip . . . 60
- 6.3 General differences in Modelling and Experiment . . . 60
- 6.4 Challenges in fabrication . . . 61
- 6.5 Outlook: Scope of Future work . . . 64

7 Conclusion **67**

8 Acknowledgement **71**

A Appendix **79**
A.1 Calculation of Important Focusing Parameters 79
A.2 Comparison of Focusing Behaviour from previous acoustic lens studies 80
A.3 Uncertainty Analysis and error propagation 80
A.4 Time-table for one Fabrication session 82
A.5 Calibrating motion of pump spot with number of steps on the piezo-inertial motor on the dichroic mirror 82
A.6 Ambitious timeline at the beginning of the project 82

1

Introduction

1.1. Subsurface imaging

Over the past few decades, nano-scale imaging has developed rapidly to help study the complex functionalities of materials and systems at small scale, with a wide range of application in the field of semiconductors [1], cellular biology [2] and many other fields. This has also called for the increasing importance of subsurface imaging, whereby the subsurface voids, cracks and other heterogenous features can be detected using disturbances in penetrating waves inside the main material. Most of these applications require single digit nanometre resolution (Fig. 1.1).

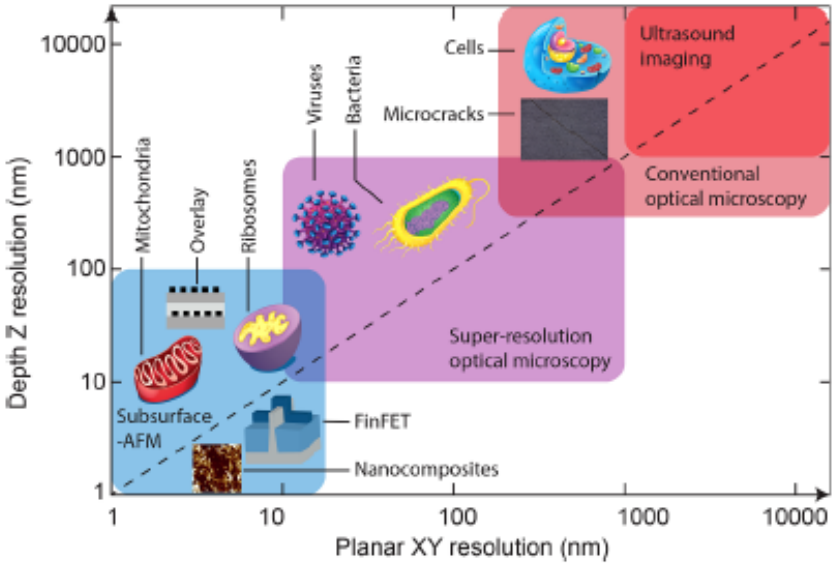

Figure 1.1: 3D resolution as a function of characteristic size of nm scale features [3]

Conventional Optical Non-Destructive Techniques are not suitable to subsuface imaging in opaque materials, and they are also limited to the diffraction limit which lies in the sub-micrometer scale. Other techniques have been implemented such as using ultrasound [4], Scannning Electron Microscope [5], two-photon polymerisation [6], X-ray Imaging [7] Nuclear Magnetic Resonance Spectroscopy [8], Vibration Spectroscopy [9, 10], Opto-nanomechanical Spectroscopy [11]. However none of them were found to achieve the desired nanometre scale resolution. In general, ultrasound is used as a basis for many non-destructive techniques like Scanning Acoustic Microscopy in the semiconductor industry with operating frequencies between 10 to 100 MHz [12], which allows spatial resolution in the order of

wavelengths of only a few μms, which is not sufficient for detecting nanoscale defects.
An approach to improve the depth resolution of subsurface imaging is to use higher frequency waves with ultrashort laser pulse (pump) of less than 1ps duration and detecting the sample response. The acoustic wave generation in the metal takes place from the thermal stress in its free surface due to laser absorption and partly due to thermal and electon-carrier diffusion, the latter being significant for semiconductors [13, 14, 15, 16]. This principle was discussed in detail by Matsuda et.al[17], where the simple thermoelastic and diffusion models were used to explain the generation of longitudinal acoustic pulses in isotropic solids, under strain generation from thermal stress by the incident pump beam [18]. The detection of the acoustic waves by the probe beam can be achieved by the optical reflectance change of the metal surface due to the reflected acoustic wave in the propagating medium, which is caused by photoelastic effect [19]. Hence a different approach is used to increase the sensitivity of detection in the current setup, which will be discussed section 4.1.1.

Focusing of acoustic waves in AFM cantilever

Previous research has shown the possibility of reaching nanometer depth resolution with the pump-probe scheme, [20, 17]. However the spot size of the incident pump pulse is limited by the optical diffraction limit and is in the order of a few μm, which limits the lateral resolution of subsurface imaging. In order to overcome this limitation, a new technique called PhotoAcoustic Subsurface Atomic Force Microscopy (passAFM) is in development at the Dynamics of Micro and Nanosystems (DMN) group in TU Delft. In the present work, the pump excitation pulse is found to generate acoustic pulse of wavelength around 80 nm at 100 GHz in Si AFM Cantilever (Fig 1.2). The AFM cantilever tip is used to guide acoustic waves in much smaller diameter around 100nm, and launch it inside the sample.

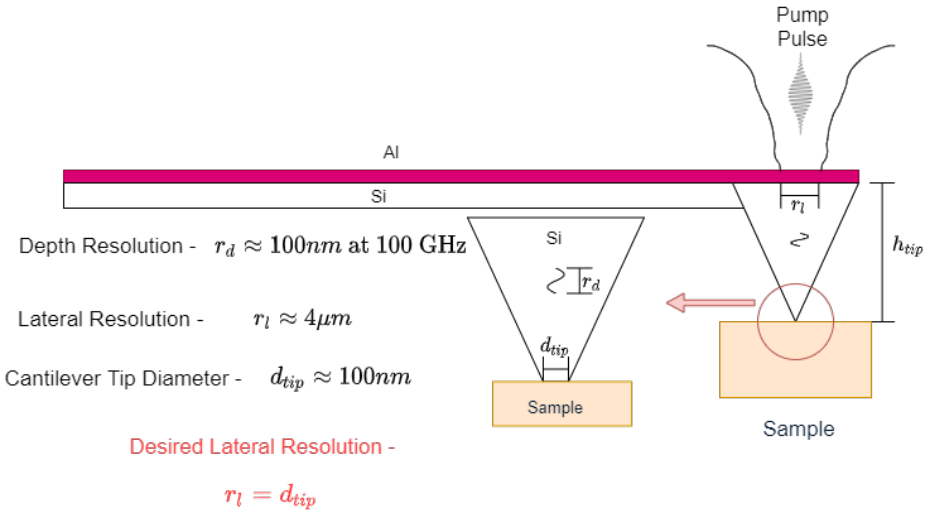

Figure 1.2: Depth Resolution and Lateral Resolution in Silicon cantilever tip

However there is an problem with this technique. The propagation of bulk acoustic waves in the small area of the cantilever tip is characterised by reflection and refraction at the interface between metal and Si cantilever as well as the boundaries of the cantilever tip. These and additional effects like attenuation in Si decrease the acoustic energy at the cantilever tip with increasing depth of propagation, and consequently the energy reflected back and detected by the probe beam is too weak to be detected above the noise level. Bryner et al. [21] investigated the focusing and detection properties of acoustic waves in pyramidal geometries by cutting at different cross-sections in Si AFM tips. From their simulations, it was found that with the increase in propagation depth, the average acoustic power increases due to reduction in tip area. However, their experimental results [22] showed that the acoustic power reflected back to the cantilever base is very weak. The latter results fit with the experiments and numerical simulations conducted internally, where less than 0.2% of the total acoustic energy is reflected back as echoes for a tip height of over 10μm and diameter around 100 nm. Hence it is necessary to focus the acoustic waves to a spot width of the order of ultrasonic wavelength and achieve maximum possible transmission at the tip area. This is expected to ensure minimum loss of energy during

propagation and consequently a large signal after reflection can be detected cantilever base with an improved Signal-to-Noise ratio.

The main objective of this project is to focus the acoustic energy generated inside the cantilever tip of the Picosecond Ultrasonic setup integrated with an AFM cantilever to maximize the intensity of the detected signal, as well as improving the lateral imaging resolution in the sample.

1.2. State of the Art

In order to achieve the desired focusing of acoustic waves at the AFM cantilever at different depths, the concept of imaging at subwavelength concentration fields can be used. In optics, some of the work done in the past decade show that Optical Superlenses can be used for near-field focusing by amplifying the evenescent field component [23]. However, more recent work by Berry et al. [24] and Huang et al. [25] have shown the possibility of easily achieving super-oscillatory lensing by using grating-like structure can create sub-wavelength focusing. In principle, super-oscillation is the ability to focus beyond the diffraction limit [26] due to the fact that band-limited functions can oscillate faster than the highest Fourier Components[24][27].The experimental studies of Rogers et al. [28] demonstrated these imaging capabilities by developing a non-invasive and easy-to-manufacture high throughput binary amplitude masks as Super-Oscillatory Lens (SOL) which can directly focus laser light into a subwavelength spot at an order of tens of wavelength distance from the mask. A design methodology based on Particle Swarm Optimisation (PSO) algorithm was used, which although was easy to implement, had the issue of high computational cost and large processing time. Nevertheless, the aforementioned study showed that the imaging resolution of the optimised design was better than $\lambda/6$, although in principle this technique does not have any physical limits on resolution, and can be improved further by refining the design.

For this current study, a similar approach can be considered for the focusing of acoustic waves in a sub-wavelength region near the cantilever tip. Previously studies have also utilized evanescent waves in Acoustic MetaMaterial (AMM) to achieve improved focus [29]. Different designs of Broadband AMM lenses in Gradient Refractive Index medium using cross shapes [30, 31] have been proposed to achieve high efficiency and smaller lens thickness. However this method requires the object to be placed close to the lens, [32, 28] and is difficult to apply for far-field focusing applications used in the current setup, where the height of the cantilever tip is of the order of ten times the wavelength or more. Furthermore the manufacturing of these lenses even in the megasonic range pose significant challenges in terms of fabrication quality. As a result, in order to achieve a compact acoustic lens, which can overcome the diffraction limit with advantages in fabrication as well as far-field imaging, a planar acoustic lens that can focus acoustic power by modulating the phase delay of the generated acoustic wave can be realised, for example a Fresnel Zonal Plate (FZP) lens [33, 34, 35]. Previous studies show attempts for realizing such Acoustic lenses, but most of them still demonstrated the problem of subwavelength focusing (showed in Appendix Table). The studies conducted by Zhao et al. [36]theoretically demonstrated the achievement of subwavelength focusing, but without substantial experimental validation. More recent works of Hyun et al. [32] used an inverse design process to systematically design and optimise a Super-Oscillatory Acoustic Lens (SOAL), to operate in the megasonic range, based on the Topology Optimisation Algorithm. The design was validated by experiment to test the efficient subwavelength focusing capabilities of incident acoustic pressure, in liquid medium, and was found to have a major advantage in terms of practical applications over the near-field imaging approaches such as AMM-based techniques. A list for the focusing characteristics of planar acoustic lens designs in previous research works is provided in the Appendix A.2.

In this research, a similar acoustic focusing technique will be used to increase the acoustic power and lateral resolution of generated ultrasonic pulse at the AFM cantilever tip in the PicoSecond Ultrasonics setup. We perform first proof-of-concept studies for focusing Ghz acoustic pulses with Fresnel Zonal Plates (FZP) at the cantilever tip, so that an imaging resolution of around hundreds of nm can be achieved. We will also attempt to fabricate the FZP designs at nm resolution to experimentally study its focusing feature and influence on generation and detection of acoustic waves. Additionally, to the best of our knowledge, this may be the first study where Fresnel Zonal Plate design is implemented and experimentally realised to focus GHz acoustic waves in anisotropic solids (AFM cantilever) at nm resolution.

1.3. Research Questions and Planning

This section deals with setting up the goals of the current research. Firstly we discuss the primary knowledge gap and the further scope of study for the present research in section 1.3.1. Based on this background we propose the research questions in section 1.3.2, and briefly describe a short plan for the first design and experiments in section 1.3.3

1.3.1. Knowledge Gap

In this study we attempt to address the various aspects of focusing of acoustic waves in AFM cantilever tip, both experimentally and computationally. To our knowledge, the application of Fresnel zonal plate design, to focus generated acoustic pulses with hundreds of nm resolution in an AFM cantilever and detect them is a new concept, so it can be considered as a research gap. It is demonstrated in the simulation results from section 2.2, that for a short duration of excitation pulse (30-40 ps) the FWHM at the focus is increased by almost 1.5 times and pressure level at the focus is reduced by a factor 1.5-1.8 (Fig. **??** through Fig. **??**). This is because the acoustic waves diffracted from the different Fresnel zones have different times of arrival to the focus. This inference is validated from the work of Sergio Perez Lopez et al. [37], who also found a decrease in axial and lateral resolution at focus when the pulse duration is considerably lesser than the transient duration. For this study, we plan to use conventional Soret-type Fresnel Zonal Plate designs, which are alternate layers of metal and non-metal zones, each of which is half of the total area of the zones. Since metal zones have much higher absorption of the pump laser wavelength than the non-metal zones, we expect that the FZPs can generate almost half of the acoustic energy as compared to a continuous Al film. Furthermore, depending on the reflectivity of the metal zones at probe wavelength the metallic zones may also act as a grating and may diffract the probe beam. Because of these factors we should also test if the SNR is still sufficient to probe the acoustic signal while generating and detecting on the FZP designs.

1.3.2. Research Questions

Based on the research gap discussed before, broad research questions are summarized below:

- **How to focus acoustic waves at the AFM cantilever tip with maximum transmission and smallest spot size, under the limits of fabrication?**
- **How does the design of the Fresnel Zonal Plate affect the generation and detection of the acoustic Pulse ?**

1.3.3. Planning for design, fabrication and experiments

We divide the entire research into 3 stages. The Theoretical modelling and Design stage discussed chapter 2, Fabrication stage discussed in chapter 3 and experiment stage discussed in chapters 4 and 5. In the first stage we numerically study the focusing capabilities of conventional Soret-type FZP designs, along with the detected acoustic signal on the cantilever body and tip with these designs. We also analyse and compare the variation in acoustic signal on different truncated tip geometries with and without the FZP on the back side of the tip. Based on these designs we fabricate the FZPs on AFM cantilever, as well as truncate the tips with and without FZPs to the desired depths and tip size. Then we implement the fabricated AFM cantilevers with Fresnel Zonal Plate design in the setup, and measurements carried out to test the imaging characteristics of the tip in contact with a sample. However, in order to validate the focusing capabilities of the present idea of acoustic lens design, some first hand measurements with conventional FZP profile need to be performed. Generating a single pattern on the cantilever tip requires the setup to be re-aligned for every FZP design. Hence for the first measurements, these patterns will be fabricated on the back surface of the cantilever body which is large enough to accommodate more than 100 FZP patterns, thus making it possible to conduct multiple tests on a single cantilever body. A segment of the cantilever body is shown in Fig. 1.3, where the FZPs are in out-of-focus and in-focus configuration. By comparing the variation in detected signal on the FZPs with the simulation results, we can obtain a first validation of the focusing feature of FZPs. The next step involves truncating the tip at different depths and consequently, different tip sizes. An increase in tip size enables a larger acoustic spot to be reflected from the tip area, thereby increasing the reflected acoustic power at the base of the cantilever. Hence we first plan to measure the SNR at the truncated tips without focusing. The final experimental stage will involve measuring on the truncated

tip with FZP being patterned on the backside of the cantilever (Fig 1.4). In this case the size of the zones are calculated such that the focal depth of the FZP is as close as possible to the truncation depth. The minimum dimension of the zones should also be above the fabrication limits, which is a critical parameter in designing the FZPs. It should be ensured that the alignment of the generation and detection setup at every measurement cycle is retained with an appreciable level of repeatability.

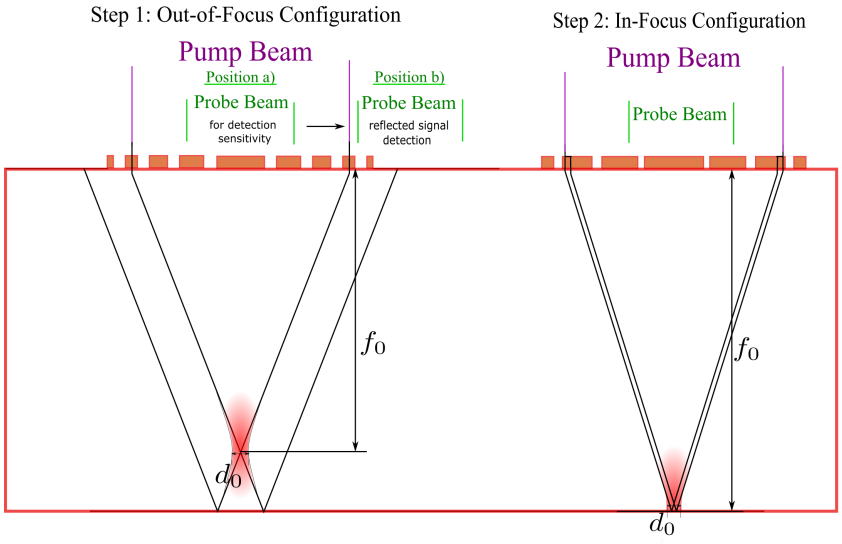

Figure 1.3: Measurement configuration on cantilever body for focusing and detection with FZPs of different focal depths. f_0 is the focal depth of the FZPs and d_0 is the spot size at focus

$$h_{tip} = f_0$$

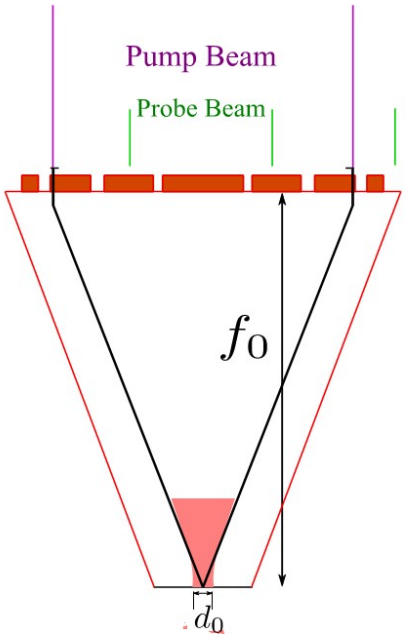

Figure 1.4: Measurement configuration on truncated AFM tips with fabricated FZPs. h_{tip} is the height of the truncated tip and f is the focal depth. We first plan to measure a signal from the truncated tips without the FZP before this step.

2

Theoretical Modelling and Calculations

In this chapter, we discuss the theoretical modelling and design of the Fresnel Zonal Plates (FZP). First we briefly introduce the fundamental principle of FZPs and study their capability to focus GHz ultrasound pulses using numerical and analytical calculations. Thereafter we discuss the design of AFM cantilevers with FZPs for experimental measurements of their focusing properties. Finally we model these designs computationally and analyse the simulation results for the detected acoustic signal and their trend with different design parameters.

2.1. Fresnel Zonal Plate Design

A Fresnel Zonal Plate in acoustics is a set of alternating thin layers of materials which are either acoustically transparent and opaque or both transparent, such that the transparent zones can diffract the acoustic waves at a particular focal depth [35]. Two types of Fresnel Zonal Plates have been used in previous studies, Soret type and Phase Reversal type. Soret type is where the focusing takes place from the alternate transparent and opaque layers due to diffraction. The transparent layers are called positive zones and the opaque layers are called negative zones. Binary Phase Retrieval types are where transparent layers are separated by a thickness to induce phase difference, leading to constructive interference at the focus. The first kind was used by Welter et al. [38] and Moleron et al. [39], with the latter using extraordinary acoustic transmission to obtain a high amplification up to 16dB in the kHz range. Phase Reversal FZPs (PR-FZP) were used by Xia et al. [40] and Su et al.[41], and can be implemented where there is not much contrast between acoustic impedence of the zonal material and the host material is smaller. Although the PR-FZP design was proposed to improve lens efficiency and the focal intensity [42], a variant of Soret-type FZPs will be chosen as the first design for the present work because of their relative ease of fabrication with 100s of nm scale feature sizes. In this configuration, the pump pulse excites the annular metal layers (Fig 2.1a) on the back surface of the cantilever, which generate acoustic waves at GHz range inside the host material. In most of the previous research, the Soret-FZP designs are used to focus kHz and MHz acoustic waves in fluids, with solid materials as acoustically opaque element for the FZP. In the present work the focusing takes place directly in Si by generating acoustic waves only in the metal (Al) zones, since the absorption of the pump laser in Si is negligible compared to Al. Hence it is interesting to verify the feasibility of this design with the metal layer as the acoustically transparent/positive zones, while the Si surface itself does not not take part in generation, but only the Si body propagates the wave. For the propagation inside cantilever, numerical simulations are carried out in a simplified COMSOL model and verified with Analytical Calculations in conjunction with Diffraction Theory in Optics.

For the numerical modelling, the radius r_n of the n^{th} zonal plate can be calculated as [43, 44]

$$r_n = \sqrt{n\lambda f_0 + n^2\lambda^2/4}, n = 0, 1, 2, \dots, m(m = 2N) \tag{2.1}$$

where m is the total number of zones, N is the number positive-negative zone pairs, λ is the acoustic wavelength inside the medium of propagation and f_0 is the height where maximum focusing takes place.

The model geometry for the first FZP design is illustrated in Figures 2.1a and 2.1b. For simplicity, a 2D axisymmetric model is considered. Here we designate acoustically positive zones as the metal(Al) layers where the bulk acoustic waves are generated (marked in Gold in Fig.2.1a and shaded in Fig.2.1b), and the negative zones are the intermediate Si layers where no generation takes place. The Input excitation is a Modulated Gaussian pulse in time and radial direction, which for simplicity is applied to the top boundary layers of the metal plates. We use linear anisotropic material model for crystalline Si with direction of propagation in the 100 axis. This is verified from the material orientation of PPP-CONTR AFM probes, where the 100 axis orientation is along the tip.

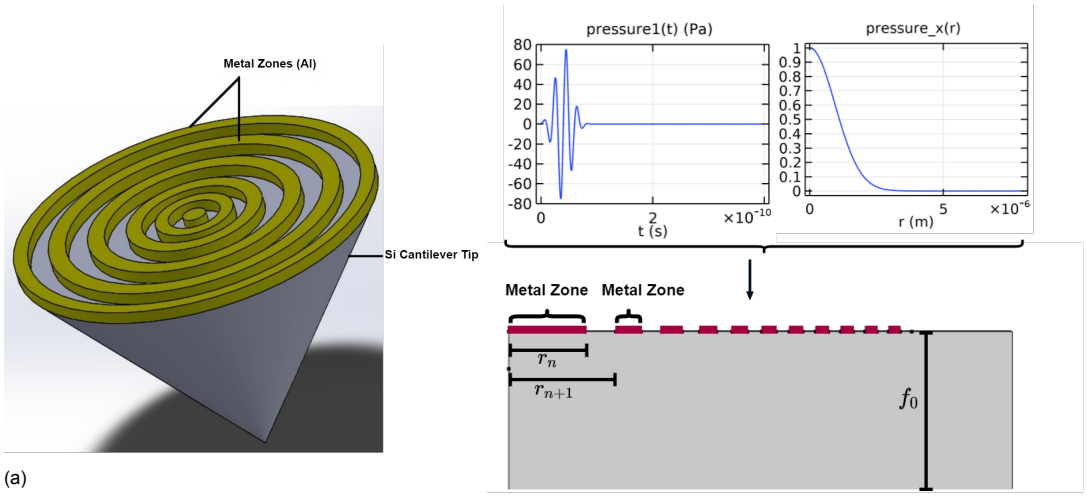

(a) (b)

Figure 2.1: a)3D Illustration of Fresnel Zonal Plates on Backside of Cantilever; b)2D axisymmetric geometry and boundary excitation of FZPs (maximum radius 4-5μm). The geometry is not to scale with the radial pressure profile on top.

2.2. Focusing Parameters and Analogy with Optics

The focusing capabilities of Fresnel Zonal Plates are controlled by a number of design parameters, primarily the wavelength range of the acoustic signal, Numerical Aperture [45] of the FZP, the number of zones m and the height of the zonal plates h_z. The first parameter is dependent on the pump pulse duration, speed of sound, the optical absorption depth of the material on the back side of the cantilever and the cantilever tip material. The Numerical Aperture is also dependent on the diameter of the pump spot and the thickness of the thermally excited region of cantilever, where the generation and focusing takes place. Hence these parameters are assumed to be fixed and set by the passAFM setup for the First Design. The primary focusing parameters in analogy with optics are:

- Pressure at the Focus
- Axial Location of Zeroth order Maximum focus (Focal Depth)
- Full Width Half Maximum of Pressure at Focus (FWHM)
- Full Length Half Maximum of Axial Pressure Distribution (Tail Width)
- Half Pressure Length of Right lobe of the Tail Width

The numerical calculation of the parameters are described in the Appendix Section A.1. The time-explicit Discontinuous Galerkin Algorithm in COMSOL 5.6 [46] is used to simulate the focusing effect of the FZP. This method solves equations of linear elasticity in the velocity-strain formulation, and is highly memory efficient since it solves millions of Degrees of Freedom with higher order discretization, enabling it to use a larger minimum mesh grid size of $\lambda/5$, compared to conventional structural algorithms. In order to validate the numerical results and check the feasibility of the design, this variation of the focusing parameters with the design parameters mentioned before are studied. The analytical model was developed by using the Rayleigh-Sommerfeld Diffraction Integral (RS) [47] over the acoustically transparent zones, to calculate the axial location of maximum focal depth, Pressure field and

the FWHM at focus. However it was found that the Analytical Results obtained from this method do not match the computational results. The cause for this issue was that a continuous wavefront with a single frequency was considered as input excitation, whereas the actual Gaussian pulse had a duration of the order of a few tens of picoseconds. Hence the analytical model was modified to include finite Pulse Duration of the acoustic signal, and the Rayleigh-Somerfield Integral was calculated over the frequency range of the Pressure Spectrum. This model was based on the work of Sergio Pérez-López et al. [37], where a transient Pressure field was obtained by maximum of the inverse Fourier transform of the Rayleigh-Sommerfeld spectrum.
Fig. 2.2 shows the Radial Pressure distribution at the focus for 6 different FZP geometries, keeping the radial size of the aperture at $4\mu m$. Compared to the conventional Diffraction Model, the Transient Model is found to capture significantly better the focusing features in the DG-FEM model.

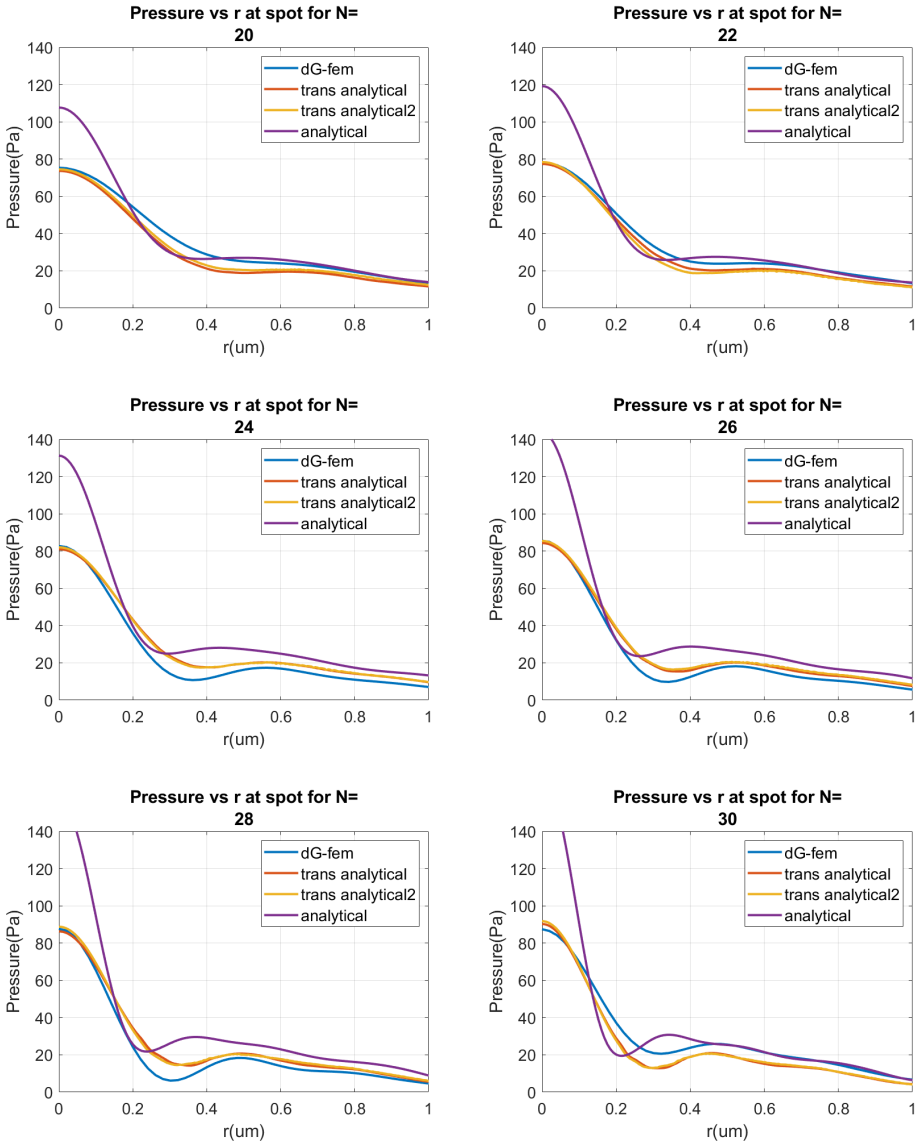

Figure 2.2: Pressure Profile at focus at various number of zone pairs. The blue line is the numerical results with DG-FEM algorithm in COMSOL. The purple line is the analytical results with conventional Rayleigh Somerfeld Algorithm. The red and the yellow lines are the results obtained from the Transient Rayleigh Somerfeld Algorithm, with the focal depths calculated from eqn 2.1 and analytical models respectively

Fig. 2.3 shows the variation of the first three focusing parameters with the number of zonal plates. It is found that with the conventional FZP configuration, a factor of around 2 is obtained in pressure of

focusing. With the increase in number of zones, the maximum pressure at focus increases, although it is found to be much weaker for the excitation with finite pulse duration (Fig. 2.3a). The focal depth reduces almost linearly with increase in m as expected from the linear dependence of focal depth in eqn 2.1 for larger number of zones. (Fig. 2.3b).For smaller number of zones, the non-linear dependence of $1/m$ plays a more dominant role, as can be seen later in Fig. 2.5a. The Half Pressure Half Width (HPHW) at the focus also has a general reduction trend between the numerical and analytical results (Fig. 2.3c), which means that the lateral resolution also improves with increasing number of zones. However the HPHW decreases from approximately 1.56λ to 0.83λ between 18 to 30 zones, so the lateral resolution is quite weak for the conventional FZP design for this application. Hence alternative optimised versions of the FZP design will be studied to improve the focusing and resolution.

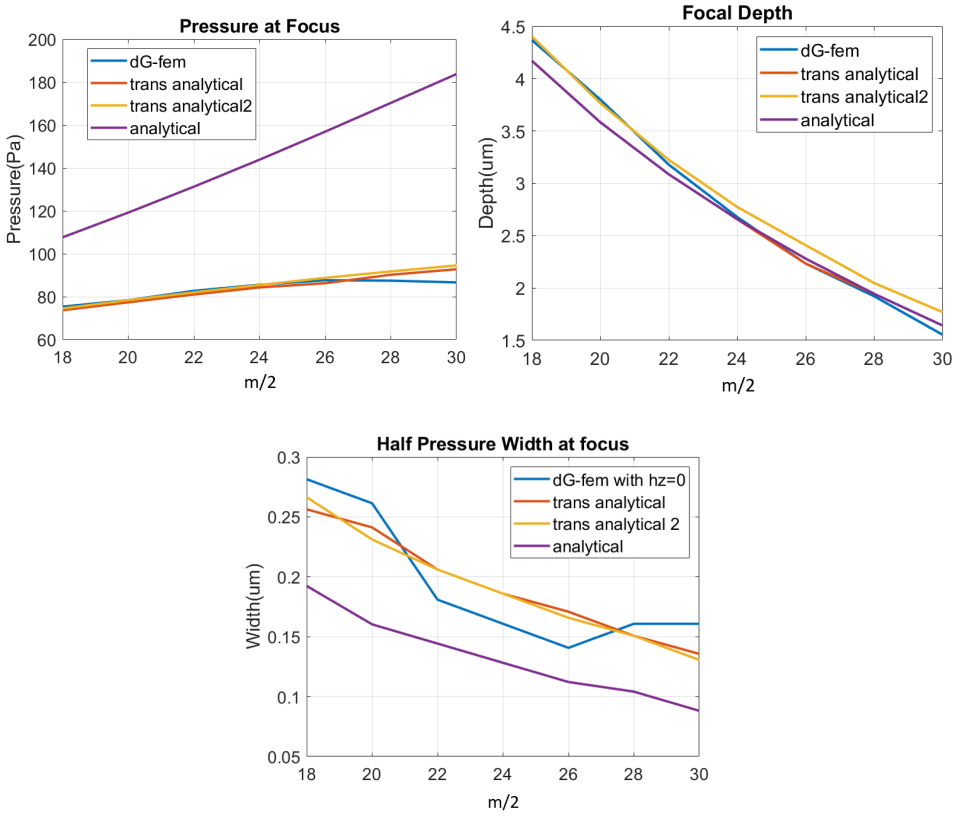

Figure 2.3: Variation of focusing parameters with number of zone pairs(N=m/2): a)Pressure at Focus, b)Focal Depth, c)Half Pressure Half Width at focus. The blue line is the numerical results with DG-FEM algorithm in COMSOL. The purple line is the analytical results with conventional Rayleigh Somerfeld Algorithm. The red and the yellow lines are the results obtained from the Transient Rayleigh Somerfeld Algorithm, with the focal depths calculated from the analytical and numerical models respectively

The analytical and numerical results in Fig. 2.3 and Fig.2.2 are found to be in line with the predictions of Sergio-Perez-Lopez et al. [37], who also predicted that there is a degradation in focusing resolution of acoustic FZP when the Modulated excitation duration is shorter than the transient duration. For the current analysis, only the first three parameters(pressure at focus, focal depth and half width half maximum) are computed numerically, due to high computational time. So far, although it has been found that these parameters are not very sensitive to the height of zonal plates, its dependency on rest of the parameters are yet to be studied.

2.3. Designing FZP on truncated AFM tips

This section describes the preliminary steps of designing Fresnel Zonal Plates to focus Ghz acoustic waves in AFM Cantilever tips. The most important parameters required for the design of conventional Soret-type FZP are the number of zones, the focal depth and the radial size of the FZP, also called the

aperture size (r_{max}). These parameters can be roughly calculated from each other using equation 2.1. Since the estimated focal depth matches well with the simulation and transient analytical calculation (Fig. 2.3), equation 2.1 can be used for estimation of the main design parameters for fabrication of the FZPs. Because of the limitations in fabrication as will be discussed in chapter 3.1, the minimum feature size of these zonal plates should also be taken into account. For conventional FZPs, this is given by the size of the furthest zone from the central axis.

In order to have the focusing at the tip, the the AFM tip needs to be truncated till the focal depth. Assuming circular symmetry of the AFM tips, the tip dimensions at the truncated height can be roughly estimated, as shown in Figure 2.4. The PPP-CONTR 50 AFM probes used in this study have approximately 16 degrees half-tip angle and 15 μm tip height.

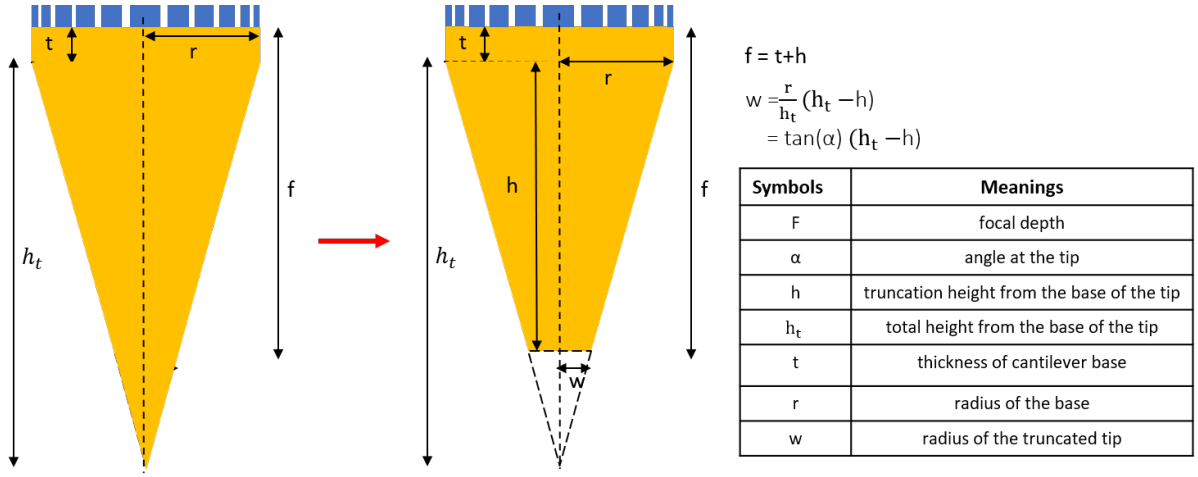

Symbols	Meanings
F	focal depth
α	angle at the tip
h	truncation height from the base of the tip
h_t	total height from the base of the tip
t	thickness of cantilever base
r	radius of the base
w	radius of the truncated tip

Figure 2.4: Truncating the tip with respect to focal depth of the FZP

Truncation($h_t + t(\mu m)$)	Tip width (nm)
12.92	1.5433
14.43	1.0400
15.25	0.7667
16.2859	0.4214
16.75	0.2667
17.2495	0.1002

Table 2.1: Truncation height vs tip width

Table 2.1 shows the variation in truncation height with respect to the tip radius. For modelling and fabrication of conventional zonal plates, the variation in focal depth and minimum feature size is shown in Fig. 2.5a and 2.5a with respect to the number of zones. The FZP designs can be selected by choosing the number of zones and size of each zone for the desired focal depth and minimum feature size, for a fabrication limit of approximately 70 nm. The AFM tips can be designed in two ways: by keeping the aperture radius fixed and varying the number of zones or vice-versa. However for the first scheme, it can be seen from Fig. 2.5a that the focal depth decrease has a steeper slope with the increase in number of zones. Hence there is a reduction of around $4\mu m$ with increase in number of zones by 2 between 12-14, and a consequent drop in the tip radius by a factor 10 (Table 2.1). Therefore in order to study the possible variation of signal within this, the designs are selected based on varying the aperture radius, for a constant number of zones. For truncating the tip to smaller depths, the first design scheme can be followed, keeping a fixed aperture size and changing the number of zones in one of the 4 plots in Fig. 2.5a and 2.5b.

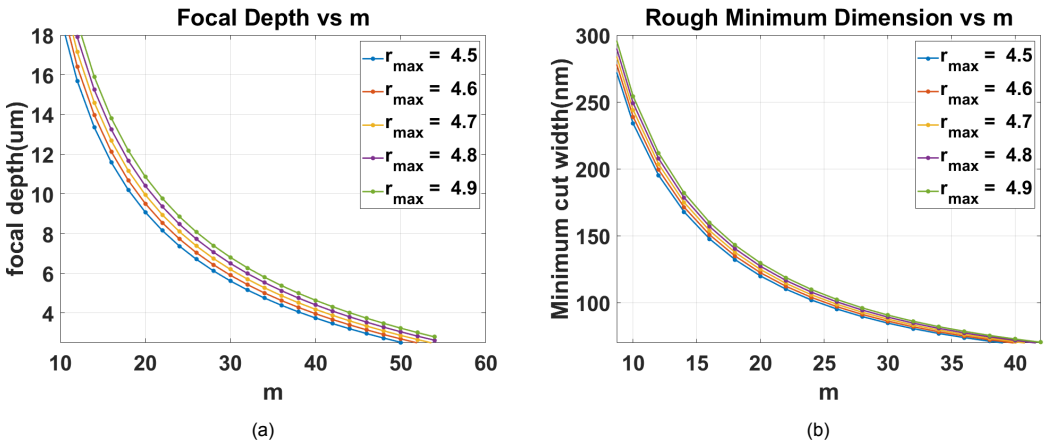

Figure 2.5: a)Focal Depth and b) Minimum Feature size vs number of FZP zones for different radius of curvature

The design of the FZPs should follow the main design constraints:

1. The aperture size of the zones should be approximately the same order as the spot size of the pump laser, to generate the maximum acoustic energy in the zonal space of the FZP rings for best focusing.

2. The minimum feature size, or the size of the last zone should be larger than the fabrication limit. The minimum lateral dimension is of the order of 100 nm, and is set by the smallest achievable spot size of the focused ion beam, and will be discussed in the chapter on Fabrication

Taking into account these limits, a design space for the FZP parameters are prepared and shown in Fig. 2.6. All the primary dimensions of the fabricated designs are selected from this design space.

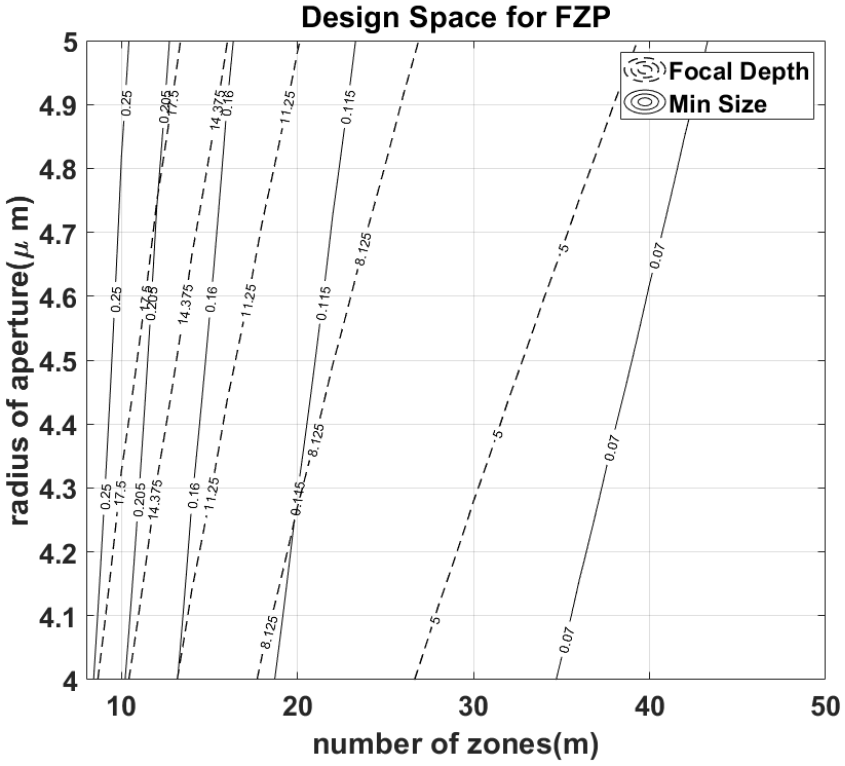

Figure 2.6: Design space for Conventional FZPs for a fabrication limits of aperture size and number of zones. The dotted lines represent the contours of the focal depth levels and the solid lines represent those of minimum feature size.

2.4. Modeling on Cantilever body and tip

Based on the experiment planning in section 1.3.3, the first step to prove the focusing by FZPs is to study the signal trend with varying focal depth at the cantilever body. In the present setup, the probe laser detects the acoustic pulse which is reflected back on the cantilever base. In presence of the FZP, the reflected acoustic pulse is detected at the surface of the Aluminium and Silicon zones. Hence in order to compare the experimental results with simulation, the acoustic pulse amplitude is calculated at the zonal plane.

The detection of acoustic echoes for the present study is done by the sensing the variation in probe laser power density, caused by changes in reflectivity of the surface . Studies conducted by Matsuda et al. [17] show that the change in reflectence δr over the unperturbed reflectence r_0 is dependent on the longitudinal component acoustic strain $\eta\,(z', t)$ induced at a depth z' from the surface:

$$\frac{\delta r(t)}{r_0} = \frac{4ik\tilde{n}}{1-\tilde{n}^2}\left(\frac{dn}{d\eta} + i\frac{d\kappa}{d\eta}\right)\int_0^\infty \eta\,(z', t)\, e^{2ik\tilde{n}z} dz' \tag{2.2}$$

and the corresponding relative reflectivity change $\delta R/R_0$ can be approximated as

$$\frac{\delta R}{R_0} = 2\,\mathrm{Re}\left(\frac{r_0^*\delta r}{r_0 r_0^*}\right) = 2\,\mathrm{Re}\left(\frac{\delta r}{r_0}\right) \tag{2.3}$$

where n and κ are the real and imaginary parts of the refractive index, and $\frac{dn}{d\eta}$ and $\frac{d\kappa}{d\eta}$ are the photoelastic constants. For a probe wavelength 780 nm, these optical constants are known for measurements on a continuous aluminium film. However the FZP, which consists of alternate rings of Al and Si is subjected to acoustic strain in both these surfaces. Because of it's low reflectivity and weaker photo-elastic constant at this wavelength, the contribution of the probe power density from the change in reflectivity of the Si zones is negligible.For a finite acoustic pulse of a few picoseconds, the contribution of the integrand to the total reflectivity in equation 2.2 can be neglected beyond the thickness of Al film, which is around 3-4 times the absorption depth of the probe laser (7.3 nm in Al) [17, 48]. The reflected probe power density scales linearly with the change in reflectivity, which is calculated from the the average acoustic strain over of the FZP or continuous film.

For simplicity, we first perform the preliminary strain calculations over the surface of the zones, as shown in Figure 2.7. The blue lines indicate the boundary probe over which the surface strain integral is computed, under the Al and Si zones. In order to avoid zero strain at the stress-free boundary conditions of the FZP surfaces, these probes are taken small depth (around 100nm) below the surface. Hence for a radially symmetric model, the longitudinal strain after dropping the pre-factors is integrated as surface integral over all the zones:

$$\eta_{\mathrm{surf}}\,(z', t) = \frac{\sum_{j=1}^{(N-1)/2}\int_{r_{2j-1}}^{r_{2j}} \eta_{zz}\,(z', r, t)\, r dr}{\sum_{j=1}^{(N-1)/2}\left(\pi\left(r_{2j}^2 - r_{2j-1}^2\right)\right)} \tag{2.4}$$

where N = number of zones $+1$, r_{2j-1} = Inner radius of the j^{th} zone , r_{2j} = Outer radius of the j^{th} zone.The denominator is the total area of the Al zones. This is approximately half of the total area of the FZP, and this factor remains fairly constant for all FZPs. Hence the average strain is just a constant factor difference with the integral in equation 2.4. In order to incorporate the effect of the detection, the longitudinal strain distribution $\eta_{zz}\,(z', r, t)$ is weighted by the reflectivity of in Al, which is 87% for probe wavelength of 780 nm.

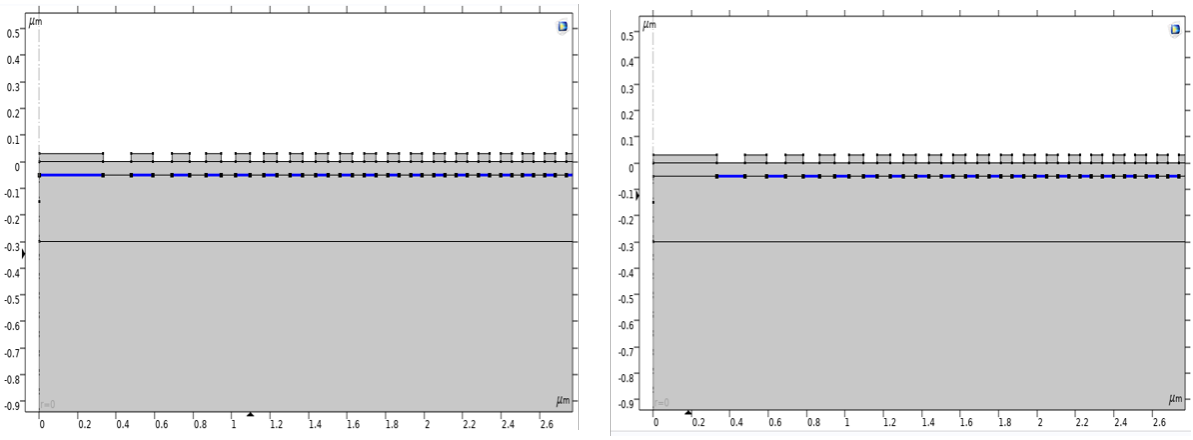

Figure 2.7: Boundary probe for first calculations of Acoustic strain under Al and Si zones

To incorporate the effect of the absorption depth ε over the zones, we use the surface average at the Al zones $\eta_{\mathrm{Al}}(z',t)$ from eq. 2.4 and substitute it eq. 2.2. Assuming the upper limit of this integral as the thickness of the Al zones h_z, and dropping the prefactors, the real part of the reflectivity change is given by

$$\begin{aligned} &\mathrm{Re}\left(\delta r/r_0\right) \approx \int_0^{h_z} \eta_{\mathrm{Al}}(z',t)\left(\frac{d\kappa}{d\eta}\cos(2k\tilde{n}z-\psi)+\frac{dn}{d\eta}\sin(2k\tilde{n}z-\psi)\right)e^{\frac{z'}{\varepsilon}}dz' \\ &\text{where } \tan\psi = \frac{\kappa\left(n^2+\kappa^2+1\right)}{n\left(n^2+\kappa^2-1\right)} \end{aligned} \tag{2.5}$$

The photoelastic constants $\frac{d\kappa}{d\eta}$ and $\frac{dn}{d\eta}$ are of the order of ≈ 5 and the average strain is of the order of $\approx 10^{-4}$. Hence we take these as constants for this analysis. In the simulation the equation 2.5 boils down to the volume integral of the product of spatial longitudinal strain with the weighted sine and cosine components and Gaussian factor for the probe beam.

2.4.1. First echo amplitude at the tip without FZP

In this section we present an approximate method of estimating the amplitude of the acoustic echo when propagating through the AFM tip. If the spot size of the acoustic pulse is larger than the tip area, part of it is subjected to reflections from the edges of the tip. The phase changes caused by the reflected components disrupts the coherence of the acoustic pulse at the edges, thereby loosing this part of the signal in the medium. The part of the acoustic pulse inside the tip area retains it's coherance and contributes to the detection signal reflected back from the tip. If we neglect the dispersion of the plane acoustic wave, the reflected acoustic pulse can thus be approximately scaled from the excitation pulse by the ratio of the area under the truncated Gaussian spot to that under the spot at the base. As illustrated in Fig. 2.8.

Assuming axisymmetric profile of the tip, the following equation holds at truncation levels 1 and 2:

$$\begin{aligned} &\text{Signal ratio between base 0 and level 1 : } \frac{\mathrm{A}_1}{\mathrm{A}_0} = \frac{\int_0^{\mathrm{R}_1} e^{-\frac{r^2}{r_0^2}} * rdr}{\int_0^{\mathrm{R}_0} e^{-\frac{r^2}{r_0^2}} * rdr} \\ &\text{Signal ratio between level 2 and level 1 : } \frac{\mathrm{A}_2}{\mathrm{A}_1} = \frac{\int_0^{\mathrm{R}_2} e^{-\frac{r^2}{r_0^2}} * rdr}{\int_0^{\mathrm{R}_1} e^{-\frac{r^2}{r_0^2}} * rdr} \end{aligned} \tag{2.6}$$

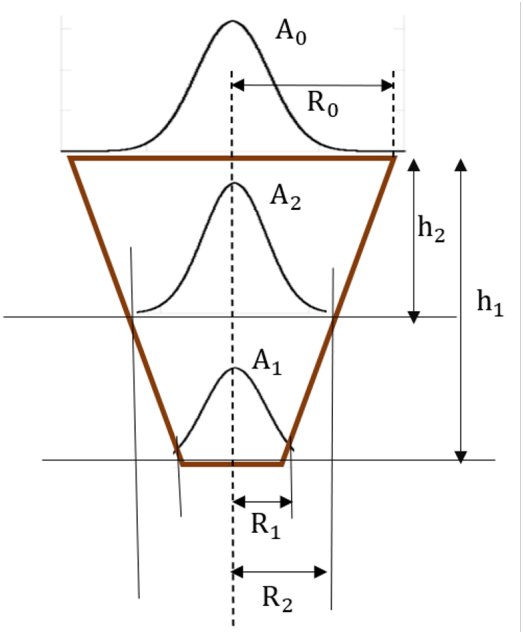

A_0 : Signal Amplitude at base
A_1 : Signal Amplitude at height h_1
A_2 : Signal Amplitude at height h_2
R_1 : Tip radius at height h_1
R_2 : Tip radius at height h_2
R_0 : Spot size (radius) of Acoustic Echo

Figure 2.8: Scaling of the acoustic plane wave at truncation depths h_1 and h_2

Apart from the edge reflections, the signal amplitude is reduced due to attenuation while propagating through the depth of the tip. The attenuation is mainly due to viscous damping of the phonons and is dependent on the frequency content and distance of propagation of the acoustic pulse in the medium. Since this is not present in the calculation of the scaling factor, eqn 2.6 yields more realistic results when there is a small difference in truncation levels 0, 1 and 2 to neglect the attenuation($\leq 2\mu m$). This verified by the experimental results of Bryner et al. in section 2.5.2

2.5. Simulation Results and Analysis

In this section we discuss results of modelling various FZP designs and compare the detected reflectometry signal with and without focusing. First we model FZPs of different focal depths on the cantilever body, followed by modelling it's focusing feature on different truncated tip geometries. These theoretical studies will be compared with the experimental measurements in chapter 5 on the AFM cantilever body and truncated tips with and without FZPs.

2.5.1. Signal Variation on Cantilever Body

The variation in the first echo signal on the cantilever body for different FZP configurations are studied in this section. Fig. 2.9 shows the average reflectometry signal for the excitation and the reflected first echo in the cantilever body of thickness 2.5 μm. The excitation pulse amplitude for the FZP is smaller than that of the excitation at the aluminium film. This is because the generation of the acoustic waves only takes place in the aluminium zones of the FZP. The total area of the Al zones is half of the area of the continuous film with the same radial size, hence the surface integral of excitation pulse caused by generation of acoustic waves in this area is reduced by an order of 1.7-2. Within the FZPs the excitation pulse increases with increasing focal depth, which can be explained by the radial Gaussian profile of the pulse, which is the maximum at the central zone. With the increase in focal depth, the FZPs also have a smaller number of zones and consequently larger central zone. This increases the effective area of maximum strain near the centre, thereby increasing the surface energy density of the excitation. In order to remove the effect of the increasing generation of excitation, the simulation results are normalised with the excitation amplitude, as shown in bottom Fig. 2.9 . We use the normalised pulse amplitudes to explain the focusing effect of the acoustic wave by FZPs of different focal depths.

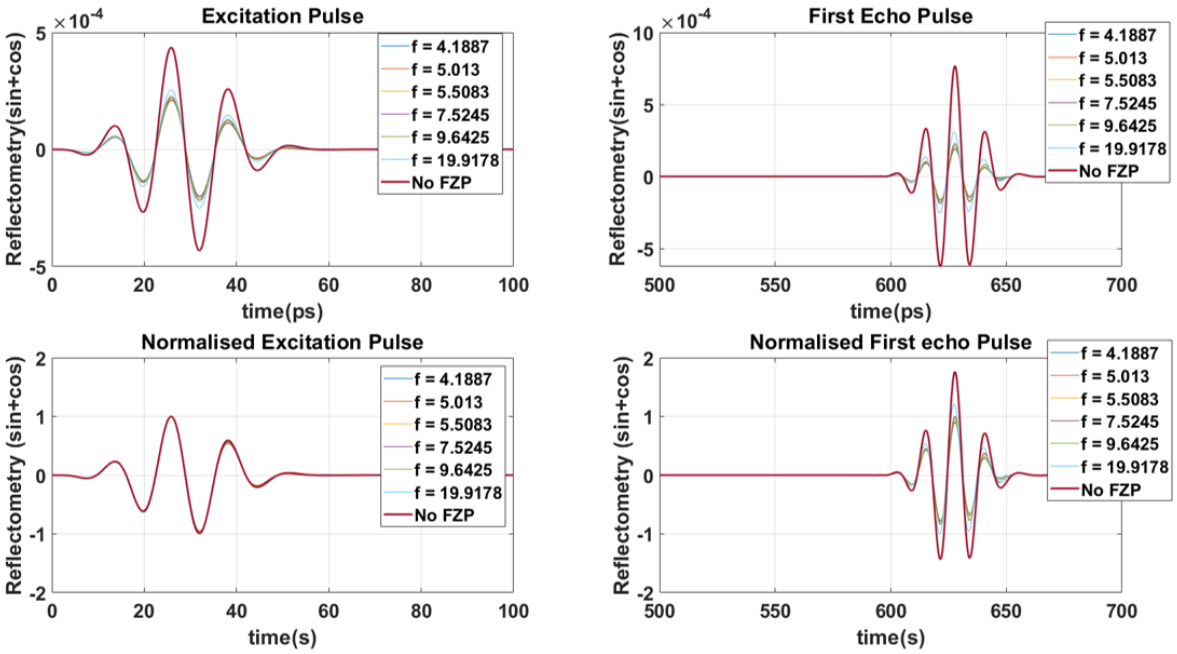

Figure 2.9: Simulated excitation and first echo reflectometry pulses (actual and normalised) on cantilever body of thickness t=2.5μm for different FZP focal depths (2t-8t).The reflectometry signals are calculated as the sum of sine and cosine components on the Al zones of the FZP without the pre-factors of the optical constants of the probe laser (eqn. 2.5) .

The higher amplitude of the echo as compared to the excitation can be explained by the reflection boundary condition at the probe region. To demonstrate this, we investigate the time response of signal probed at different heights below the FZP plane in Fig 2.10. At 0.2 μm below the surface, the incoming and reflected echoes are separated in time. As the probe volume gets closer to the surface, the incident and reflected echo interfere to increase the amplitude. Since the pulse width of the echo is 40 ps or 33 nm, around the thickness of the volume probe. So the amplitude of the echoes is expected to increase almost by a factor of 1.2- 1.5 due to interference with the reflected component. This factor is generally slightly smaller with the FZP because part of the reflected wavefront is truncated by the Si zones which are not probed in the simulations.

The variation of normalised reflectometry amplitude with focal depth shown in Fig. 2.11 follows an increasing nature with focal depth of the FZPs. This may be explained by the spread of the Gaussian profile of the in the in the probe region, and the relative size of the central zones, which receive the maximum part of longitudinal strain from the echoes (Fig. 2.12). For focal depths less than the cantilever thickness, the reflected acoustic echo diverges at the probe region. If the spot size is larger than the probe diameter, part of echo is not detected by the probe beam. Beyond $f = t$, the entire acoustic echo is probed because it is localised in the FZP region of around 8.5-9.4 μm diameter, which is similar size or less than the probe diameter. For focal depths beyond 3t, the acoustic echo is converged back to the surface, but spread of the strain profile spreads more in the FZP region, and is also probed in the central Al zones of larger size. Hence the signal amplitude increases with the increase in focal depth and decreasing number of zones. In the limiting case when the focal depth is infinitely large, there is 1 zone where the signal becomes maximum. This is the case of the continuous film without FZP, shown as the horizontal limit line in Fig. 2.11.

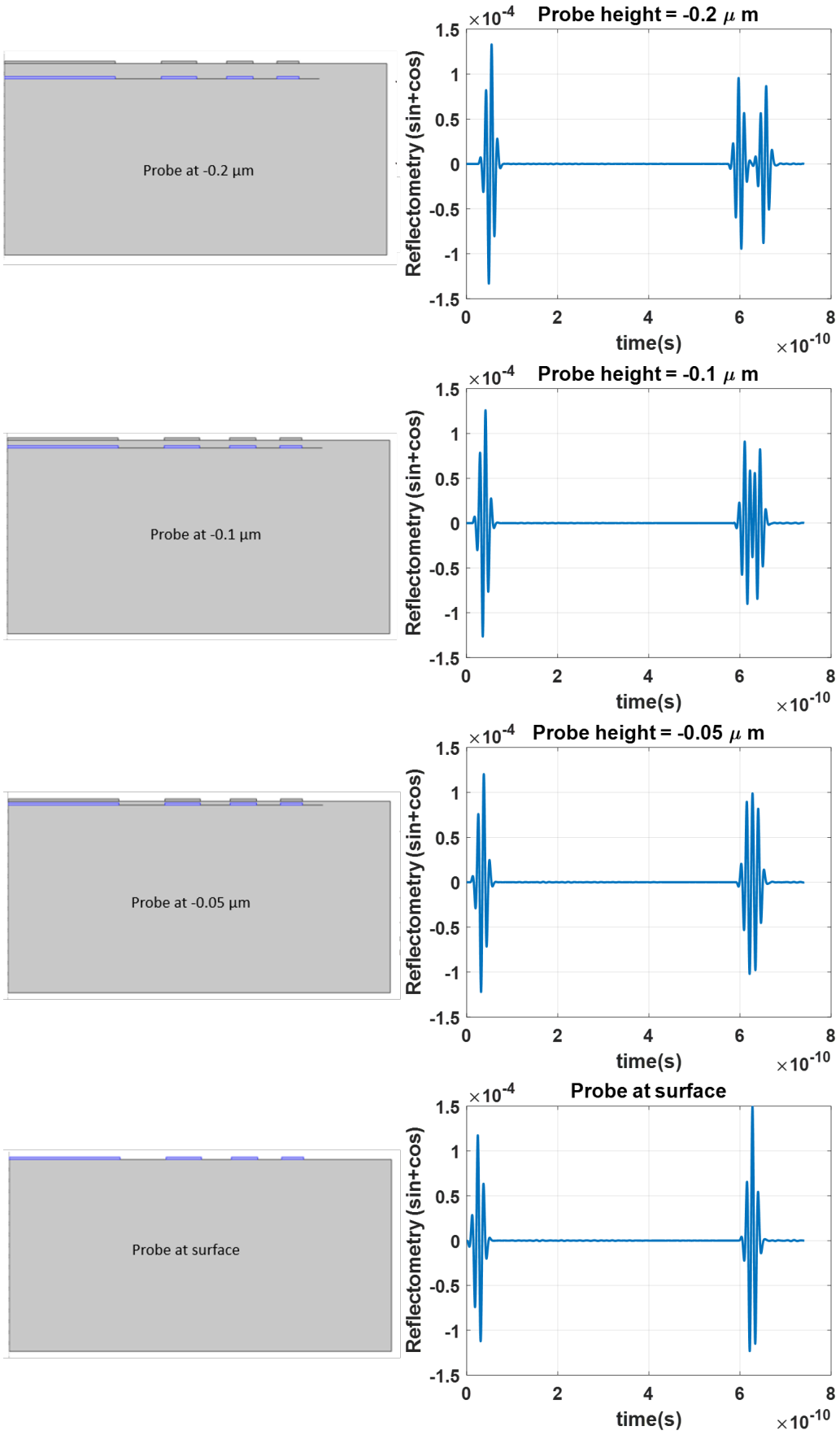

Figure 2.10: First echo probed at different heights under Al zones,(probe regions marked in blue).As the probe region approaches the top surface of the Al zones, the incident and the reflected components of the acoustic echo interfere with each other, until maximum constructive interference when probed at the Al zones themselves. This effect causes the reflectometry signal near the surface to be higher than the excitation signal in Fig. 2.9

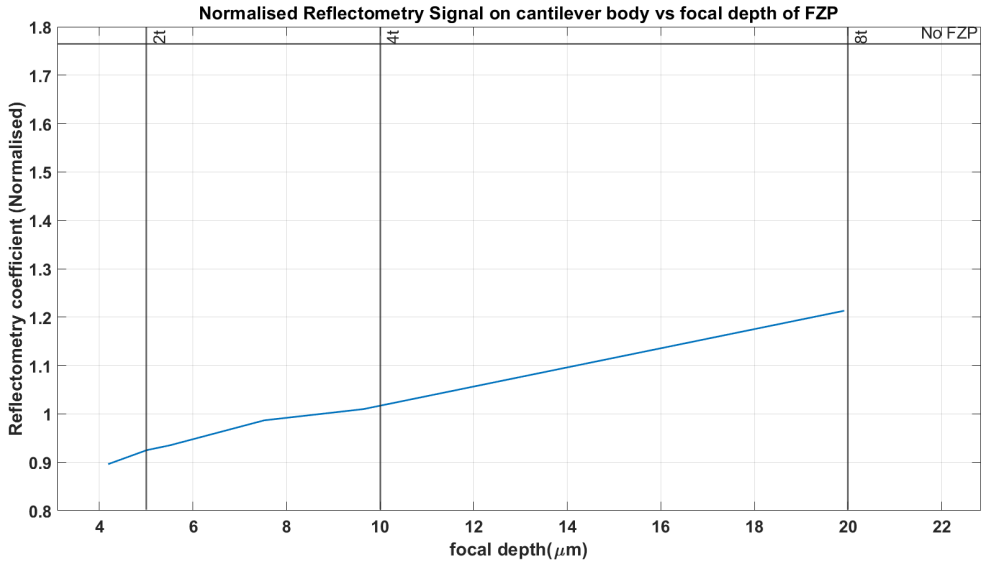

Figure 2.11: Normalised reflectometry signal on the cantilever body vs focal depth of FZPs (blue curve), ranging from 2t-8t, t being the thickness of the cantilever body. The black horizontal line shows the reflectometry signal for a continuous film.

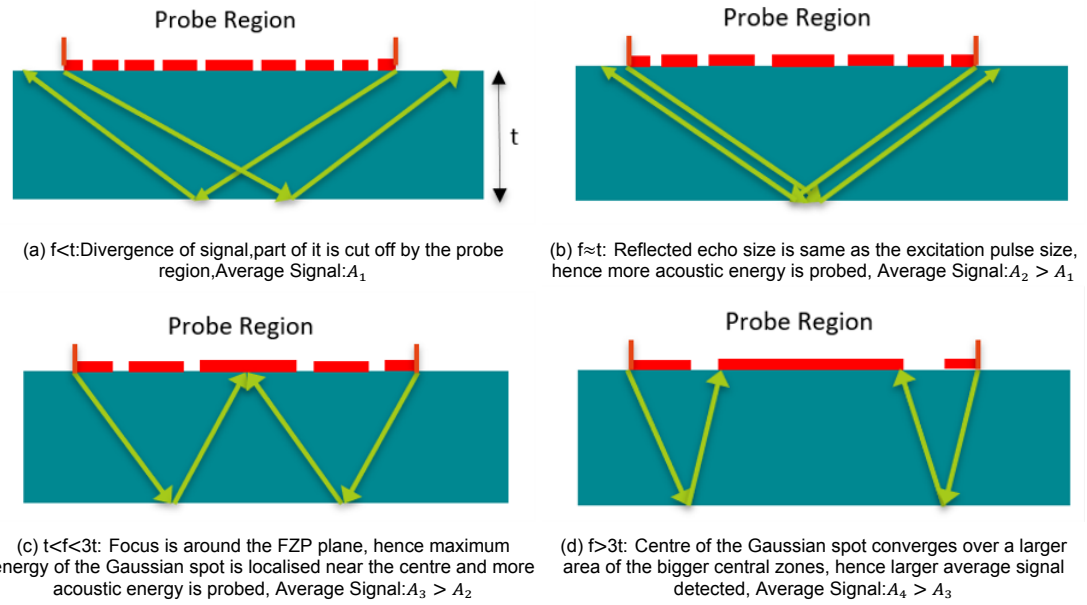

(a) f<t:Divergence of signal,part of it is cut off by the probe region,Average Signal:A_1

(b) f≈t: Reflected echo size is same as the excitation pulse size, hence more acoustic energy is probed, Average Signal:$A_2 > A_1$

(c) t<f<3t: Focus is around the FZP plane, hence maximum energy of the Gaussian spot is localised near the centre and more acoustic energy is probed, Average Signal:$A_3 > A_2$

(d) f>3t: Centre of the Gaussian spot converges over a larger area of the bigger central zones, hence larger average signal detected, Average Signal:$A_4 > A_3$

Figure 2.12: Schematic of variation in acoustic echo spot size on the FZP plane. for different focal depths (f). The signal variation in Fig. 2.11 depends on this variation in spot size.

2.5.2. Signal variation at the tip

In this section, we discuss the results for focusing of acoustic pulses in the truncated tip with FZP and compare them with the results without the FZP.

Verifying analytical results at the tip

We first verify the tip scaling factor described in section 2.4.1 with the simulation results. In this regard we calculate both the strain integral and the reflectometry component on a cantilever base with a thin Al film, and on a truncated tip with base diameter 5 μm and height 11.45 μm (Fig. 2.13a and 2.13b respectively). Fig. 2.13c shows the peak-peak amplitude of the strain and the reflectometry signals of the first echo, and the ratio of these amplitudes at the tip with that of the base matches well with the first equation of eqn. 2.6

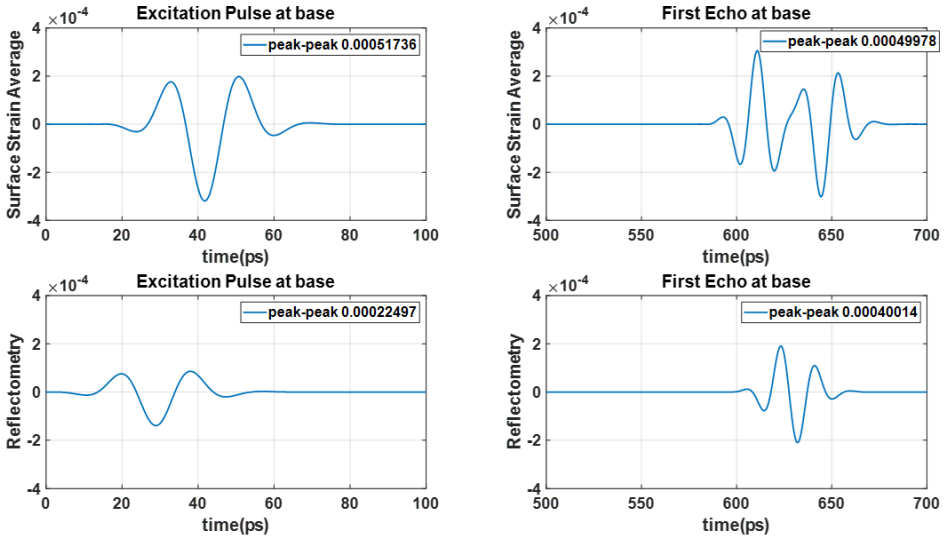

(a) Strain and reflectometry components at the base

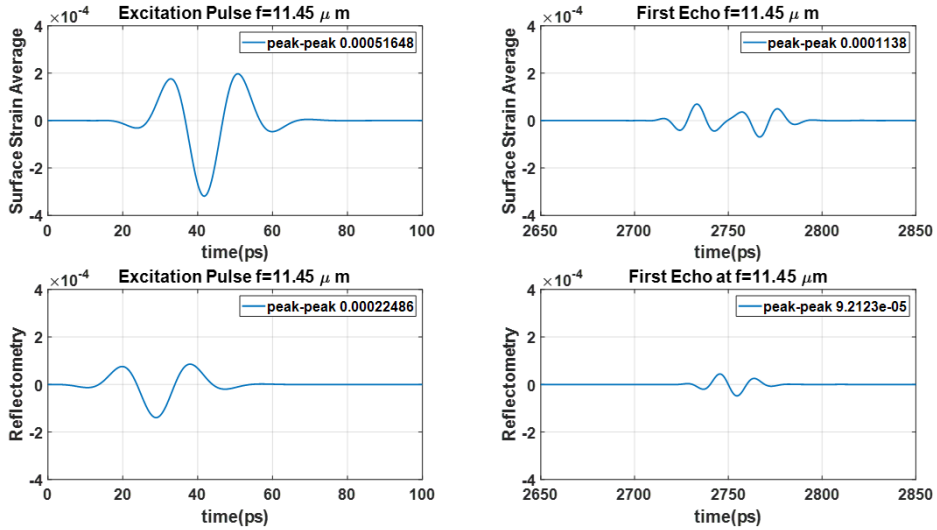

(b) Strain and reflectometry components at the tip

Parameter	Excitation Pulse (h=11.45)	Reflection Pulse (h=11.45)	Excitation Pulse (base)	Reflection Pulse (base)	Reflection Pulse (h=11.45)/ Reflection Pulse (base)	
					From plots	Analytical
Strain Integral	5.17e-4	1.138e-4	5.1736e-4	4.9978e-4	0.23	0.23
Reflectometry components	2.25e-4	9.2123e-5	2.249e-4	4.0014e-4	0.23	

(c) Table for comparing scaling factor with simulation results. The last column is the analytical scaling factor between the 5 μm radius base and the tip radius 3.3 μm at 11.45 μm truncation height. This factor is calculated from the first expression of eqn 2.6

Figure 2.13: Comparing reflectometry amplitude of acoustic echoes with analytical calculations

We also verify the scaling factor between two truncation levels with the experimental results in the thesis of Bryner et al [22](Fig. 2.14). The ratio between the reflectometry signals at truncation heights 10.41 μm (3.5 μm tip diameter) and 12.46 μm (1.9 μm tip diameter) is found to be 0.367, and the scaling factor between at these levels is calculated as 0.377 (second expression in eqn 2.6) with a acoustic spot size of 4.5 μm diameter at the base. This also shows that for small difference in tip truncation, the signal amplitude is primarily governed by the scaling factor and less by the attenuation in Si.

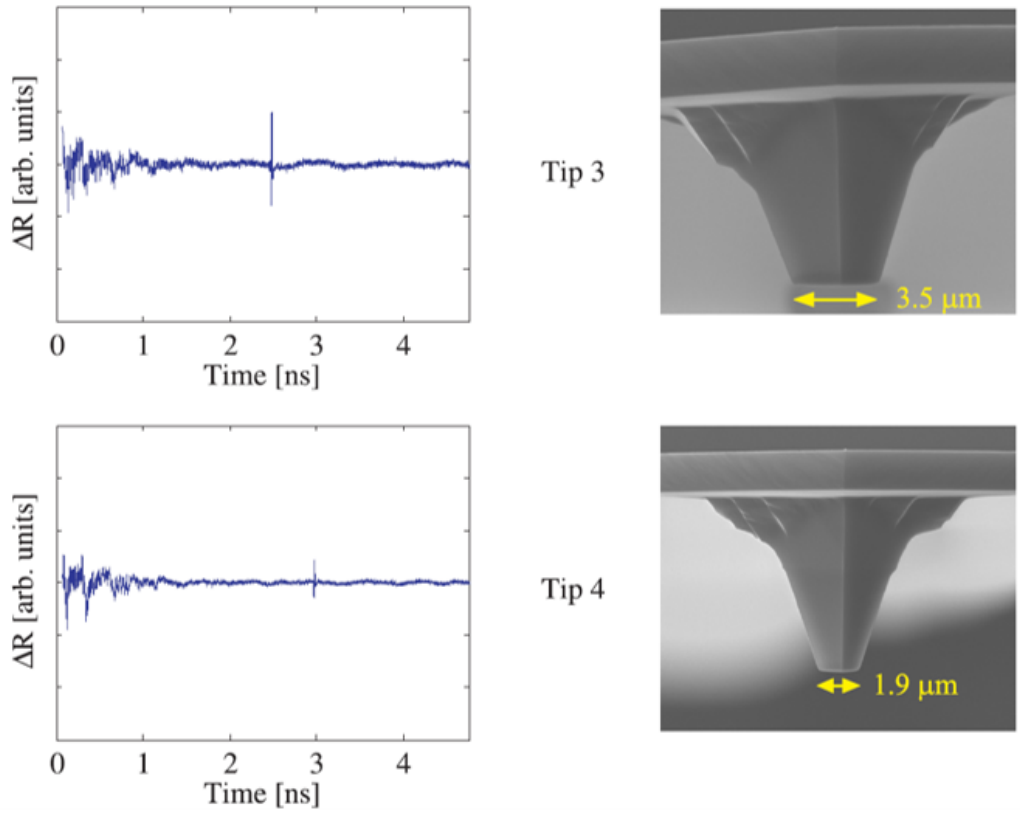

Figure 2.14: Measured Reflectometry Signals by Bryner et al.[[22]]. Top figure represents signal at truncation depths 10.41 μm (3.5 μm tip diameter) and bottom figure signal at truncation depths 12.46 μm (1.9 μm tip diameter)

Reflectometry signal on the the truncated tip with FZP

Here we study the reflectometry signal of the first echo at different truncation geometries of the tip. Two aperture sizes of the FZPs are are used: 4.7 μm and 4.5 μm with the number of zones from 12-24 and 14-26 and focal depths 15.6-7.37 μm and 14.6-6.24 μm respectively. Fig. 2.15 shows the normalised reflectometry signal of first echo at different tip truncation depths. The reflected pulse from the truncated tip has a trailing component which increases with the increase in focal depth. This can be explained by the fact that the part of the acoustic wavefront diffracted from the outer zones of the FZP has a larger pathlength compared to the wavefront from the inner zones, and therefore time delay in interfering with the latter. For shorter focal depths, there is a larger spread in pathlengths from the zones to the tip,leading to growth of the trailing wave behind the main wave. A second explanation is that the focused acoustic pulse reflected from the tip gradually transforms into spherical wave from a planar wave with larger travel distance from the tip. The reflected spherical wave also has more acoustic dispersion, causing the lower frequency components to trail the higher frequency ones, thereby increasing the tail-width for larger travel distances.

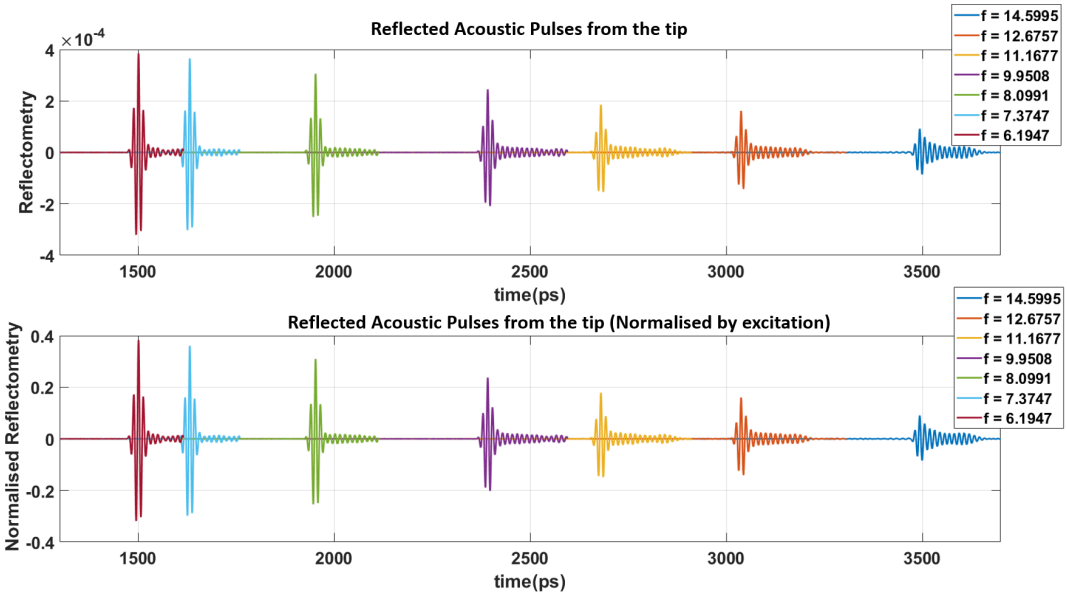

Figure 2.15: Reflectometry and Normalised reflectometry signal from the tip at different focal depths of FZPs (aperture size 4.7 μm). The truncation height of the tip is same as the focal depths. All points are normalised with the maximum peak-peak value of the excitation.The reflectometry signals are calculated as the sum of sine and cosine components on the Al zones of the FZP without the pre-factors of the optical constants of the probe laser .

Figures 2.16a and 2.16b show the variation in normalised reflectometry signal with and without the FZP. The relative amplitude of the detected signal on the FZP is a trade-off between two opposite effects:

1. Focusing of the acoustic wave on the tip, which maintains the coherence of the reflected wave, thereby increasing the signal. The size difference between the tip and the focal spot is important in determining the amount of coherent acoustic energy that reflects back.

2. the amount of acoustic energy received by the Al zones vs the part cut-off by the Si zones. This is dependent on the size of the central Al zones which receives the maximum energy of the Gaussian spot.

This effect is demonstrated in the schematic Fig. 2.17a and Fig. 2.17b. For smaller focal depths and wider truncated tips, the latter effect is more significant, and hence the reflectometry signal is smaller than that without FZP. For larger focal depths and smaller tip sizes , the effect of focusing with FZP becomes more important, as more of the acoustic wave gets truncated and looses it's coherence without the FZP .Hence the signal on the FZP surpasses that of without FZP, with the latter dropping sharply with the tip-scaling factor (blue curves in Fig. 2.17a and Fig. 2.17b). Secondly for the FZP, reflected wave from the longer focal depths becomes more spherical and the maximum part of it's energy is detected at the larger central zones. For the present simulations, the normalised reflectometry signal on the FZP starts overcoming the signal without the FZP for truncation depths beyond 12 μm and tip radius less than 1.5 μm, and grows upto 6 times higher at depth 15 μm or tip radius 460 nm.

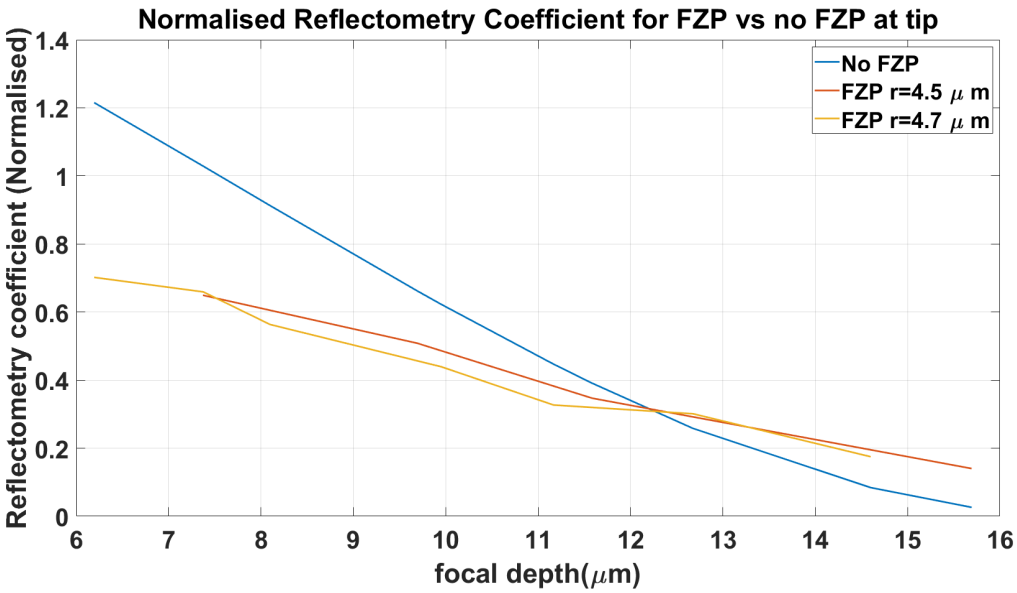

(a) Normalised Reflectometry vs focal depth with and without FZP on tip

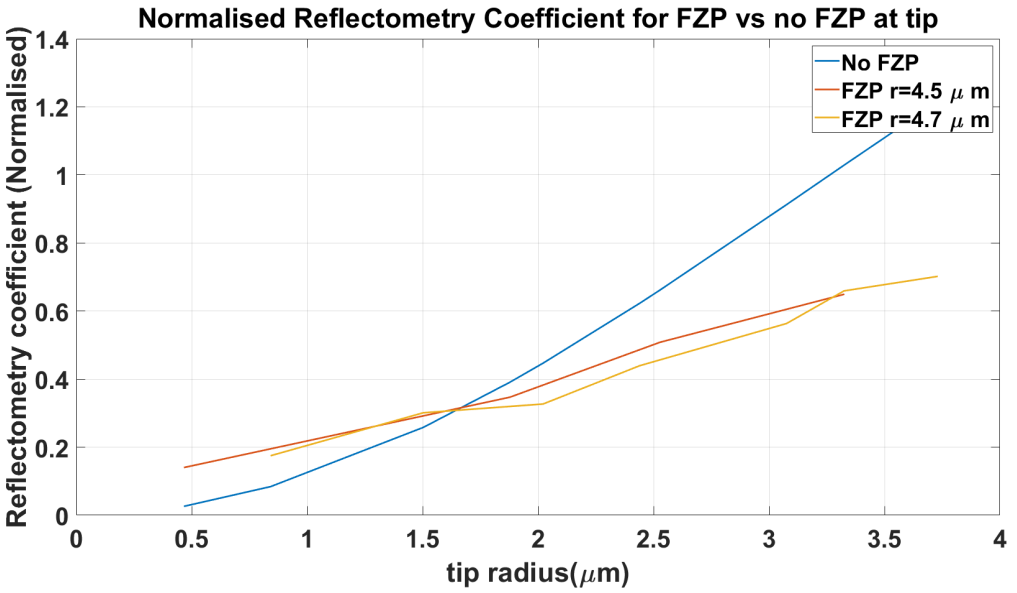

(b) Normalised Reflectometry vs tip radius with and without FZP on tip

Figure 2.16: Normalised Reflectometry vs a) focal depth and b)tip radius with and without FZP. The simulations are performed with aperture size 4.5 μm (red line) and 4.7 μm (yellow line)

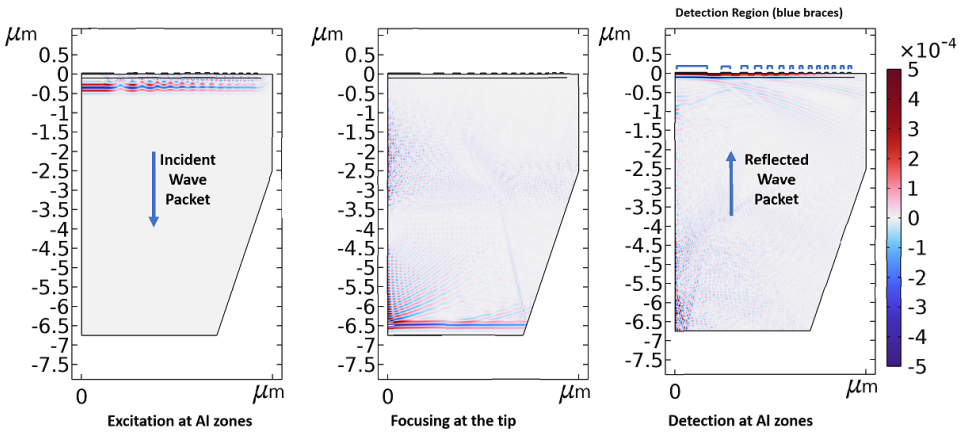

(a) Focusing and detection of acoustic strain pulses on FZP with focal depth 7.5 μm(aperture size: 4.7 μm)

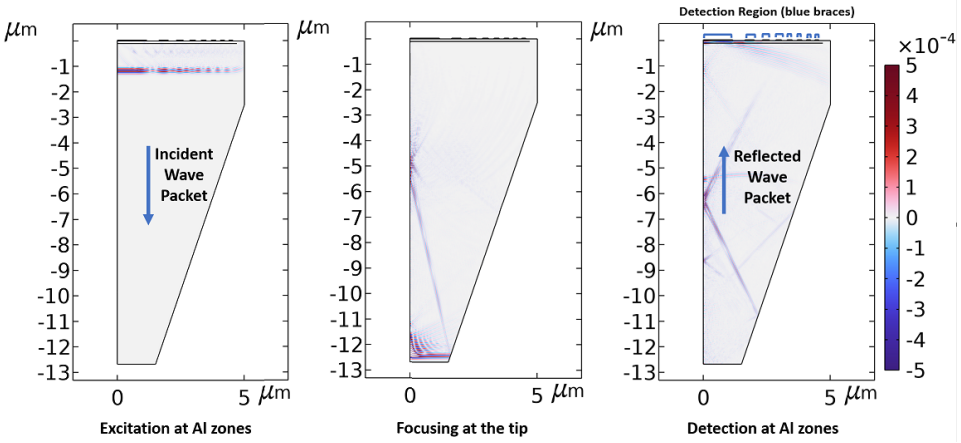

(b) Focusing and detection of acoustic strain pulses on FZP with focal depth 12.7 μm (aperture size: 4.7 μm)

Figure 2.17: Focusing and detection with FZP on the tip at different focal depths. The acoustic pulse is detected on in the Al zones of the FZP, cutting off part of the signal on the Si zones. The acoustic pulse is the longitudinal strain parameter. All legends have the same scale, ranging from $(-5 * 10^{-4} - 5 * 10^{-4})$

3

Fabrication

In this chapter, we discuss the first designs of acoustic lensing devices for focusing GHz ultrasound in AFM cantilever. First we provide a brief introduction on the fabrication process employed in the present work and associated parameter settings used. Thereafter we discuss the various steps for patterning FZP lenses on the cantilever body and tip, and also truncating the tip upto the desired height and tip surface area, for detecting the first echo signal.

3.1. Fabrication Process

The design of the cantilevers with Fresnel Zonal Plates are carried out with Focused Ion Beam Milling. The Helios G4 Plasma FIB UXe Dual Beam with SEM [49] is used for both the fabrication of the FZPs and truncation of the tips. In this process the collimated beam of plasma ions is extracted from an RF-coupled Xe chamber, forming a significantly long tail beam [50] with a high intensity. The alignment of the center of the Fresnel lenses with respect to the tip should be ensured, and the scanning strategy of circular patterning will be determined at the beginning. The main milling process consists of two primary steps as shown in 3.1, firstly the acoustic lens profile will be generated on the metal layer, followed by cutting the tip to a desired focal depth. The FZP pattern is created by making annular cuts of the metal layer at the locations of the negative non-metal (Si) zones. This process is associated with material removal at the sharp ends forming bevels, hence a safety margin should be considered above the base dimensions to accommodate for the extra material removal. The tip truncation is then done by aiming ion beam from the side to progressively remove layers of materials along the longitudinal direction of the tip until the desired axial depth is achieved. The truncated tip surface will be further polished with a plasma beam of lower power.
The conventional acoustic lens design is estimated to have features with minimum dimensions of the order of 100-150 nm for 18 Zones. Increasing the number of zonal plates or optimizing the present design for better focusing may lead to even smaller dimensions. Although having a narrower ion beam width is suitable for patterning smaller features, the minimum lateral dimension is desired to be more than 50nm. Furthermore, the depth resolution of the ion beam might also be a constraint for minimum feature size in the axial direction. This depends on two main parameters, the power and the material to be removed. Although the former is specified by the ion current of 1.5pA-2.5μA, we perform further investigations (section 3.2) to estimate the relationship between the current and minimum depth cut on Al metal layers on Si. Additionally the stability of the ion beam at lower power should be taken into account while fabricating such patterns.

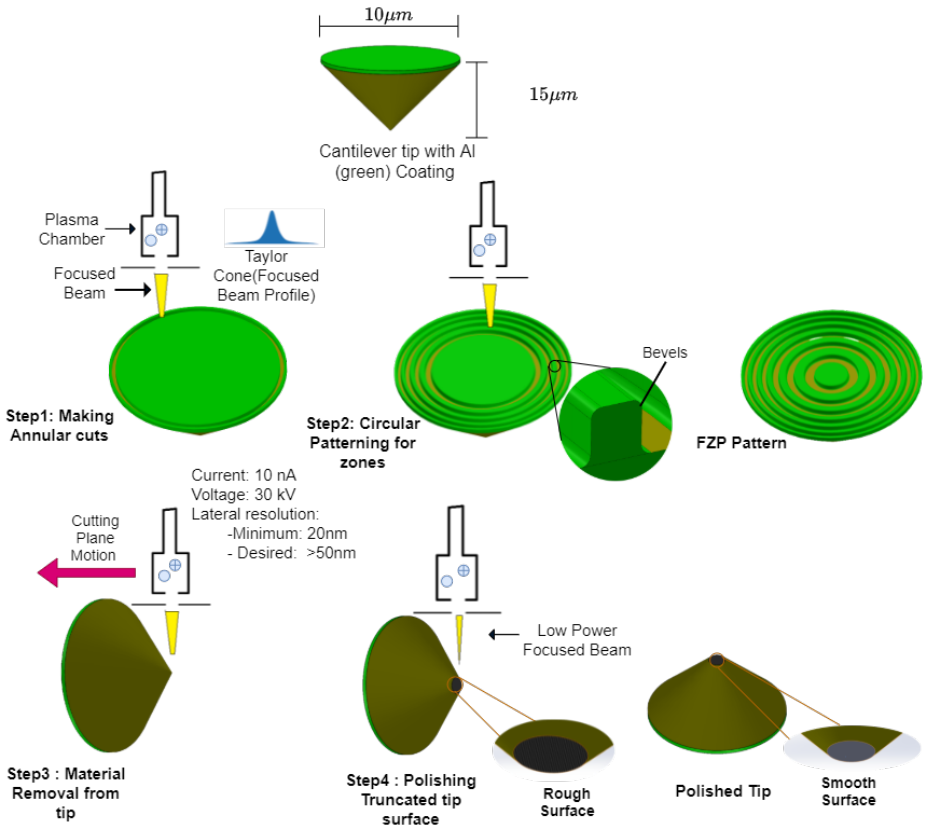

Figure 3.1: Fabrication flow diagram for FIB milling of Truncated AFM tip with FZP

3.2. Parameter Settings for Focused Ion Beam

The Focused Ion Beam is used to cut the FZP rings on the AFM cantilever tips and also truncate the tips to the desired focal depth, as discussed in section 2.3. However it is first important to understand the basic parameters required for generating features using the FIB. Hence we first conduct some dose tests to understand the effect of these parameters on the dimensions of the patterns milled with the FIB. After that we fabricate a first FZP pattern to realise the feature dimensions and depth of cut that can be generated using the preliminary parameter settings.

3.2.1. Dose tests on cantilever tip

In order to study achievable feature depths in aluminium and silicon layers,the dose tests are performed on the chips of broken cantilevers which are coated with aluminium. The basic user-controlled input parameters are:

- Ion current: Most important parameter that sets the etch rate and the total milling time. It is generally set between 3-10 pA for the present feature dimensions.
- Material profile: The FIB software sets it's internal parameters based on the set material. By default it is Si.
- Penetration Depth: Determines the depth of cut for one set material profile. Sets the total milling time, and the lateral dimensions of the patterned features.
- Overlap: The percentage overlap between two adjacent points of the ion beam. Sets the minimum pitch distance between two points in the feature geometry. For best possible accuracy, 90% overlap is recommended for smaller features. Increasing overlap also increases the total milling time.

Fig. 3.2 shows the dose tests for determining the settings for achieving different depths of cut in the chip. We cut square holes of $0.5\mu m$ with penetration depths ranging from 10-200nm and ion currents

from 1-10pA. Currents from 3-10pA start etching away the aluminium layer from depth settings of 50nm and removes part of the silicon for higher depths. Due to lower ion bombardment, smaller currents like 1-3pA cannot remove the full Al layers for smaller penetration depths (10-50nm), but is much better for larger penetration depths (200 nm). This effect is more visible from the irregular Al layers on Si for penetration depths between 50-150nm, and also at 200nm for 1pA current.

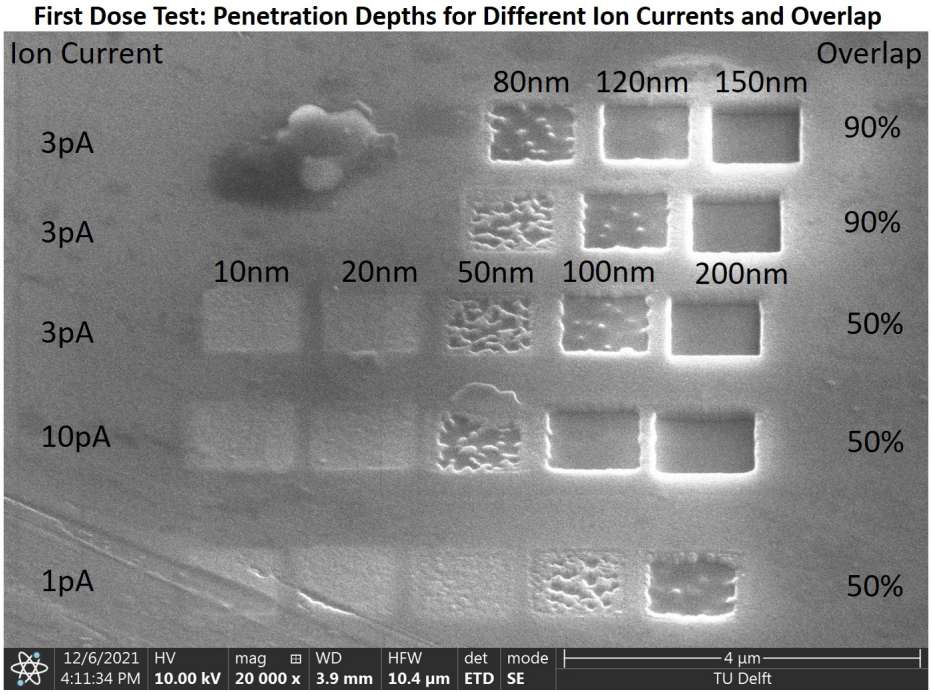

Figure 3.2: Dose tests for depth, overlap and Ion Current

For samples with larger penetration depth the margin between the Al and Si layers (Fig. 3.3) is used to estimate the height of the aluminium coating. The total depth of cut over the Al-Si layers is more than the set penetration depth for Si due to faster material removal rate on aluminium than on the silicon. However, the ion current also cuts through an oxide layer on the Al film, therefore the factor between actual and set penetration depth is hard to estimate.

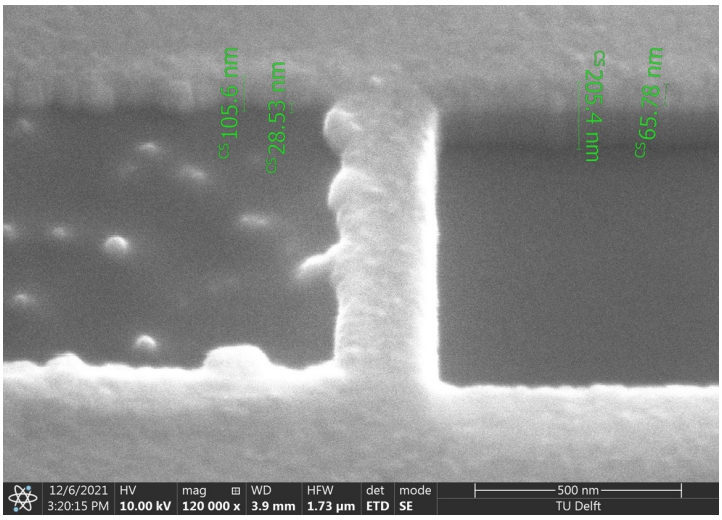

Figure 3.3: SEM images for Milling in Al and Si layers for settings.Right hole: Depth=100nm, Ion Current=3pA,Overlap=50%,Left Hole: Depth=200nm,Ion Current=3pA,Overlap=50%

3.2.2. Fabricating first FZP patterns

We fabricate the first FZP design (Fig. 3.4) on the broken AFM cantilever chips with the parameter settings from the dose test. As introduced in section 3.1, the ion beam scans through the specified region of the FZP and repeatedly cuts annular patterns on the aluminium surface, thereby generating alternate layers of silicon rings and intermediate aluminium rings. The inner and outer diameters of the rings are set by the radial dimensions of the FZP.

The The FZP has 8 Al zones and 8 Si zones. The outermost Si zone of $4.5\mu m$ radius is also the smallest zone and has a thickness of 150nm, which is more than the theoretical fabrication limit of 50 nm. Hence a higher ion current of 10pA can be used to generate these features. However, it should be noted that for smaller features, a smaller current is recommended for the same penetration depth, to avoid undesired material removal from the Al zones. Additionally, an optimum focusing of the ion beam is required to produce smooth-edged features with smaller currents. The zoomed in pictures at 250,000 magnification show an overall depth of approximately 150 nm (with a set penetration depth of 120 nm) across the Al and Si layers, with the depth of the Al coating of approximately 30nm. The Al zones have circular edges or bevels on each side and the bevel size is dependent on the ion current and the penetration depth. For the present settings it is approximately 20nm, and hence we set this as a tolerance on the inner and outer diameter of the annular zones. In the present study, we add this tolerance on the positive or Al zones and remove them from the negative or Si zones.

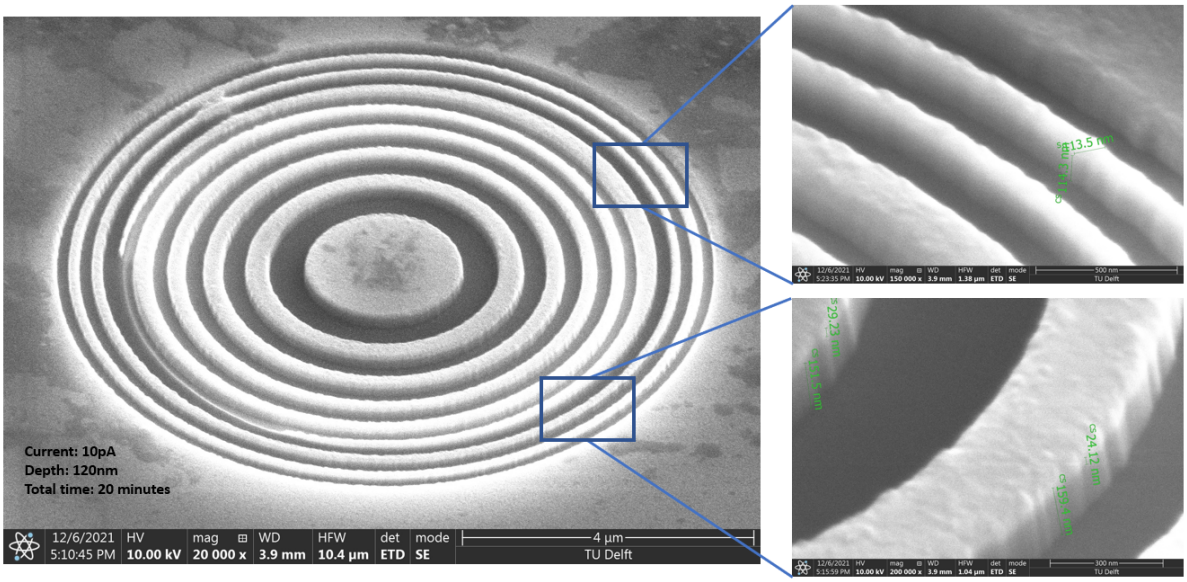

Figure 3.4: SEM images and feature sizes of first FZP on cantilever chip: N=16, Radius: 4.5 μm

3.3. Designing on AFM Cantilever body and tip

In this section we demonstrate the actual design process on on the AFM cantilever and truncation of the tip for the proof of concept experiments of acoustic wave focusing. As introduced in the planning stage in introduction chapter, Fig. 3.5 shows that the FZPs of different focal depths are patterned on the cantilever body. We plan to compare the variation of the acoustic signal detected on these FZPs with the simulation results of section 2.5.1. Thereafter, we fabricate the FZPs on the AFM tip and truncate the tip to the desired focal depth. We also truncate the tips of some samples without the FZP in order to compare the acoustic signals with and without the FZP in the tips. .

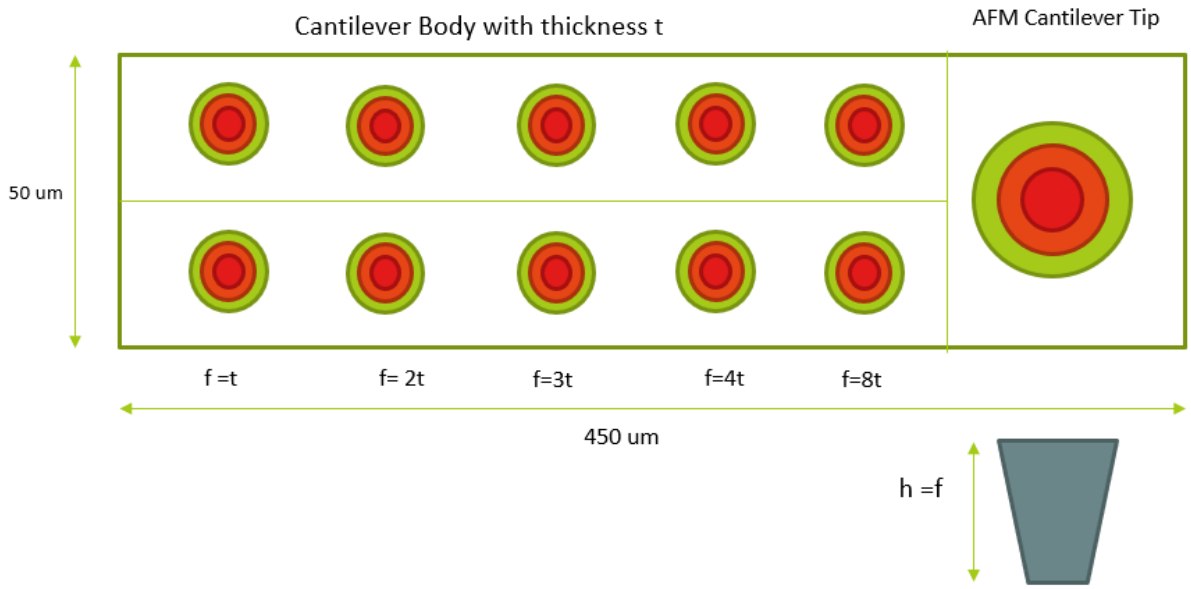

Figure 3.5: Planning fabrication on AFM cantilever for proof of concept of focusing. We fabricate FZPs on the cantilever with different focal depths to test the focusing

The fabrication plan described in Fig.3.5 requires milling features on the AFM tips in multiple planes, and also cutting from both sides of the AFM cantilever. However the FIB-SEM setup consists of a holder and a mount suitable for making features only in xy plane. To resolve this, we prepare a custom-made holder (Fig.3.6). This enables the ion beams to mill the AFM cantilever from both sides of the xy plane. Furthermore, the holder is equipped with 3 stubs in x,y and z directions, so that the AFM cantilevers are oriented in all 3 planes in the 3D space. This is particularly essential while truncating, where it is important to visualise and cut the tip in both the front (xz) plane and side plane (yz) to ensure a flat surface

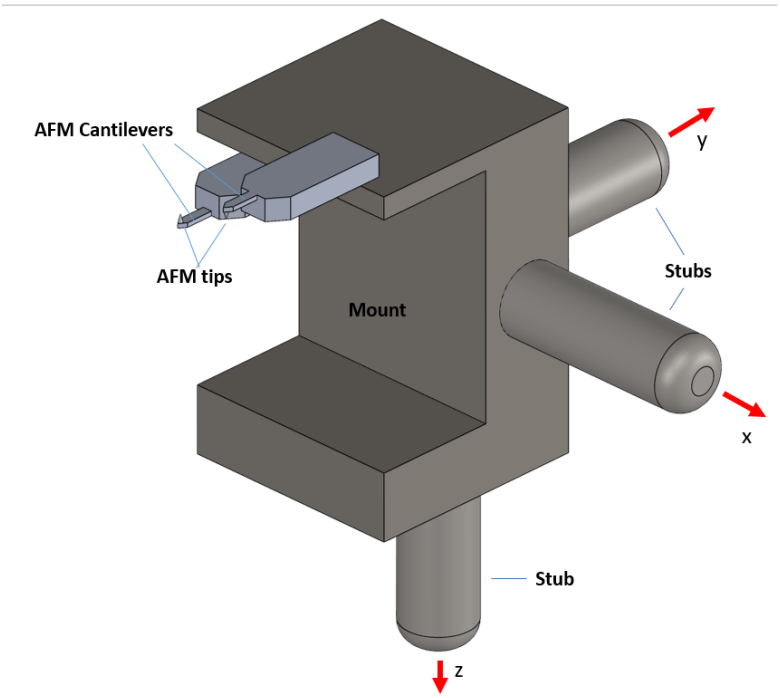

Figure 3.6: AFM Holder for imaging and milling in two directions(top and bottom) and 3 planes (xyz)

3.3.1. Fabricating FZPs on AFM Cantilever Body

Here we present the first part of the fabrication process, which involves FIB milling of FZPs on the cantilever body. For the first proof-of-cencept studies, we design conventional Soret-type FZPs that are designed to focus 80 Ghz acoustic waves (wavelength of 105 nm in Si). The FZPs are of the same radial size and have 5 different focal depths ranging from the thickness of the cantilver body (t) to 8 times the thickness of the cantilever body. As shown in Fig(2.5a) and Fig(2.5b), the smallest focal depth also has the largest number of zones and smallest feature size. For the present designs this is 70±20nm for focal depth of t and 90±20nm for focal depth 2t. These dimensions are close the theoretical limit of the minimum lateral dimension, and therefore requires optimum focusing with the ion beam. With the focusing, a small current of 3pA and a penetration depth of 100nm is used, but still produced some irregularities on the edges of the zones for the focal depth of 2t (5 μ m), as shown in Fig. 3.7a. On the other hand, a larger focal depth of 8t with a minimum feature size of 270±20nm could be fabricated by a larger current of 10pA with better dimensional accuracy and lesser feature size, as shown in Fig.3.7b. The maximum feature size, or the diameter of the central zones ranges from 0.8μm±20nm for t to 2.9μm±20n for 8t, which is similar to the order of the wavelength of the probe beam, implying a possible diffraction of the probe laser on reflection of the probe beam.

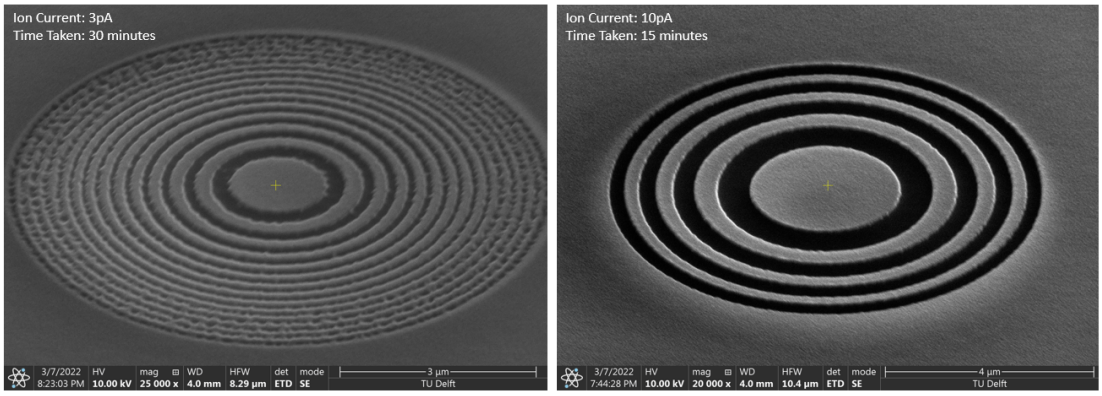

(a) Focal Depth=5.01 μm (2*thickness of Cantilever)
Number of zones: 28
radius: 4.1 μm

(b) Focal Depth=19.91 μm (8*thickness of Cantilever)
Number of zones: 8
radius: 4.1 μm

Figure 3.7: SEM images of FZPs with largest and smallest focal depth achieved with present settings

Fig.3.15 shows a SEM image of AFM cantilever with all the fabricated FZPs at 10,000x magnification, and the 250,000x zoomed in view of each of them. The FZPs marked in blue are the ones which achieve smoothest feature edges with the present focusing and parameter settings of the ion beam. The ones marked in red are distorted FZPs, mostly charecterised by insufficient or excessive material, irregularities and focusing defects. A larger current of 10pA with 90% overlap is sufficient to produce the FZPs with focal depths 4t and 8t. For 3t and 2t, a smaller current of 3pA are used, which however generates some irregularities, especially in the smaller outermost zones. For the focal depth 1t, the feature size are too small to reach even with 3pA and the current focusing, thereby causing unwanted material removal from the positive zones. A current of 1pA is too small to remove all the aluminium from the negative zones, thereby leaving out an irregular layer of Al in the middle and outermost zones. However there is still room for improvement in the future sessions, where with more dose tests (particularly for lateral dimensions) the best possible focusing and parameter settings can be achieved.

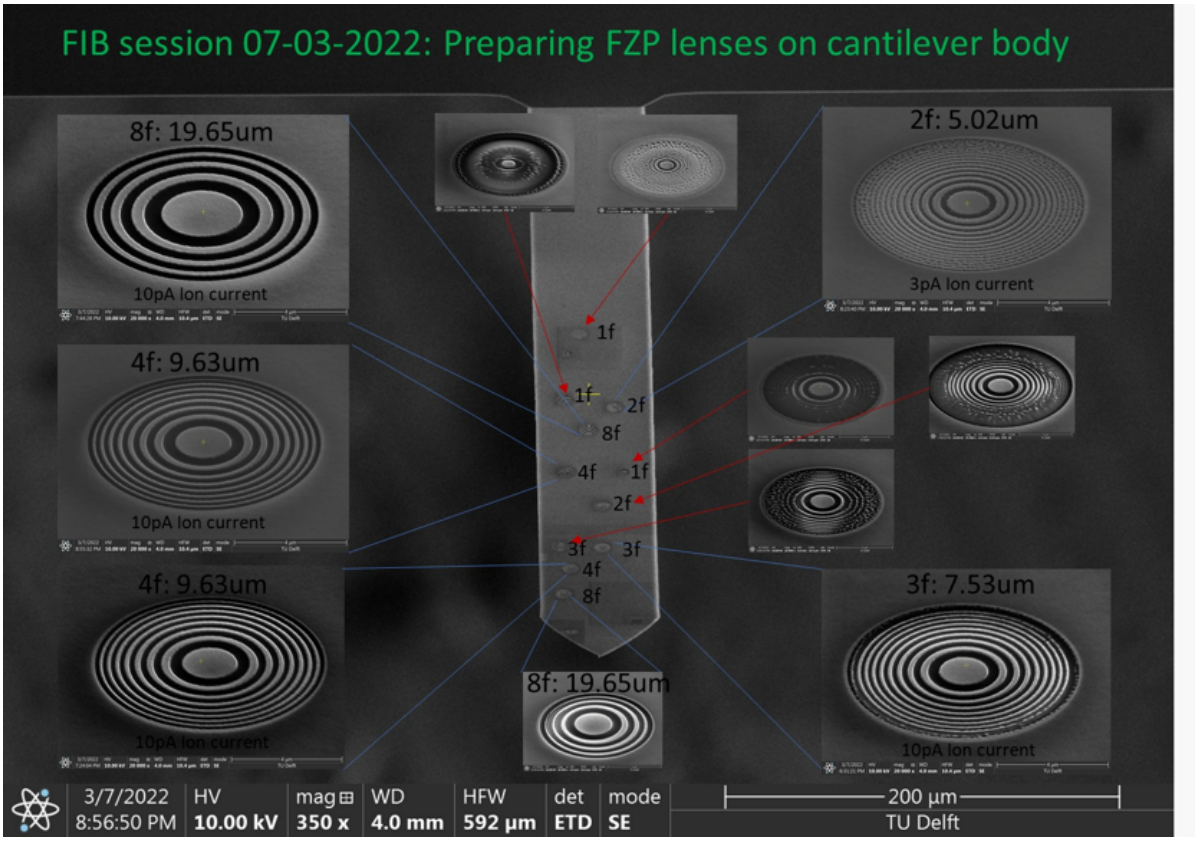

Figure 3.8: AFM Cantilever Body with FZPs (focal depths f-8f (where f=t,thickness AFM Cantilever)) (**Picture by Ruben Guis**). The blue lines indicate the FZPs where all the zones are propperly fabricated, and the red lines indicate the ones that are distorted due to sub-optimal parameter settings and focusing defects of ion beam

3.3.2. Fabrication on AFM tips

After fabricating the first FZPs on the cantilever body, we move on to designing these structures on the tip and truncating the tip upto the desired focal depth. In order to measure and compare the detected acoustic echoes with and without focusing, we also prepare truncated AFM tips without FZP of the same depth.The truncation depth should be as large as possible to ensure minimum tip area in contact with the sample, for better resolution. So we first find the maximum possible truncation depths, where we can just see the signal over the noise level. In this regard, we measure the echo amplitudes in the cantilever body at every reflection, and plot them with the total depth traversed by the echo as shown in the upper plot in Fig. 3.10. Thereafter we scale the echos to the estimated amplitude for the same depth traversed in the tip, using the scaling factor discussed in section 2.4.1. The bottom plot in Fig. 3.10 compares the estimated echoes at the tip to the noise level. The noise level is set as twice the standard error of the measurement noise in the boxcar for 60 averages. We estimate that the signal amplitude is same as the noise level for depths around 10 μm. With more averaging, the noise level can be reduced to measure the signal at this level. We also select a second and larger truncation depth of 12.7 μm, where the signal might be under the noise level without the FZP, but might be measurable with the focusing effect of the FZP.

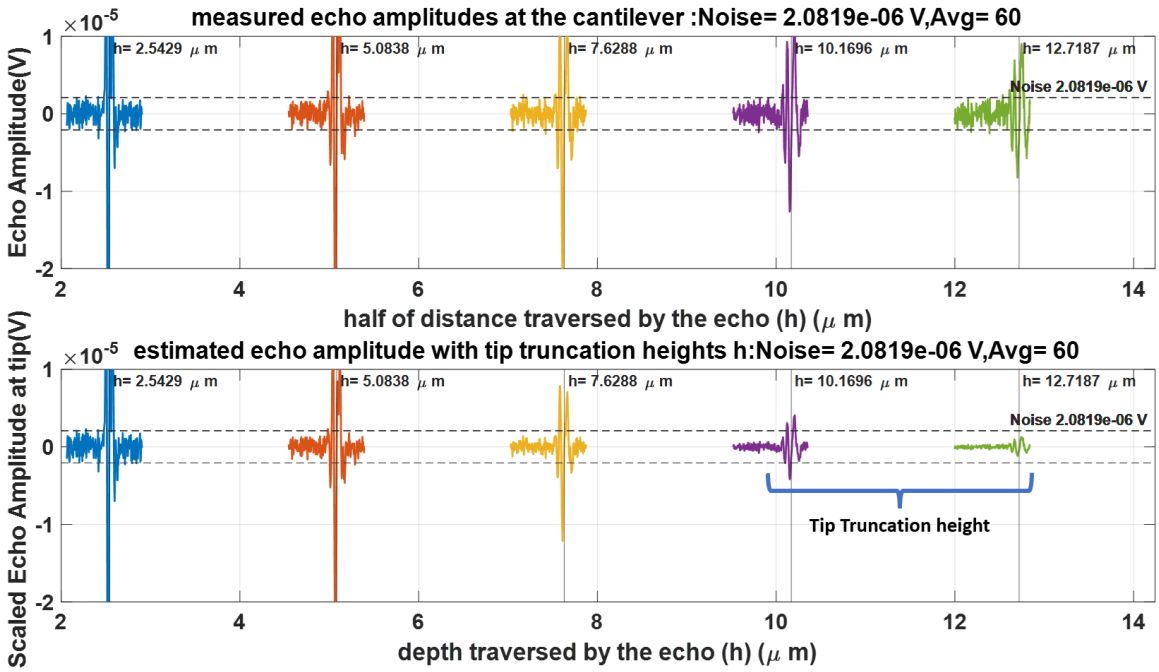

Figure 3.9: Comparing echo amplitudes with the measurement noise level. The upper plot shows the measured echos reflecting from in the cantilever body. The bottom figure shows the corresponding echo amplitudes estimated at the tip same truncation depth. The blue box shows the selected truncation depths at the tip. Note that these measurements are taken with the old photodetector

For the first proof-of-concept studies, we truncate 4 AFM tips, 2 with depths around 10-11μm and the other 2 near 12-13μm. Thereafter, we design FZPs with the corresponding focal depth one of each pair of truncated tips. The steps for the fabrication process on the tip are discussed below:

- **Step 1: Height Measurement** As a first step we measure the total height of the each of the AFM tips, as shown in Fig. 3.10.The total tip height is used to calculate the radius of the truncated tip using the axi-symmetric assumption in (Fig. 2.4), and verify it with the actual dimensions of the pyramidal AFM tip. All 4 of the samples have tip heights ranging from 14.5-14.9 μm, and with the the thickness of the AFM cantilver (2.5 μm), it gives a total tip height 17-17.4 μm

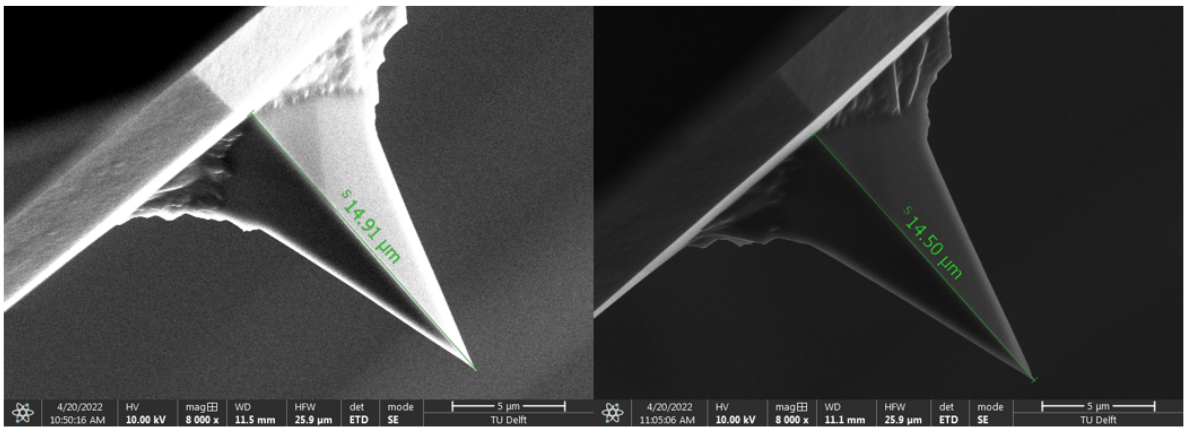

Figure 3.10: SEM Images for Measured tip heights

- **Step 2: Making Alignment Markers on the tip** In order to focus the generated acoustic pulses at the center of the tip, it is important that the centre of the FZP is aligned with the tip. Therefore small holes are cut at the the edges of the AFM tip from the underside in order to mark the axial position of the tip along the length of the cantilever, as shown in Fig. 3.11. Because of axial

symmetry of the cantilever, lateral position of the tip is in line with the tapered end point of the cantilever. Hence the position of the two holes and the tip end point can be used to mark the centre of the FZP with respect to the tip, while fabricating from the top side.We use a high current of 1nA for making markers of size 2x2 μm. For cutting through holes on the body itself we use a depth of 3 μm with these settings.

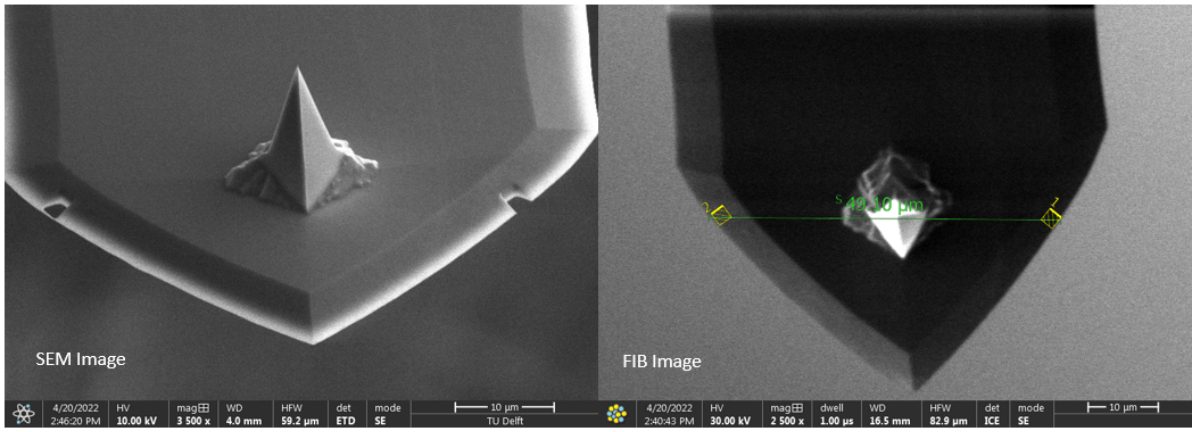

Figure 3.11: Making features on edges from the tip side to align FZPs with the tip

- **Step 3: Truncating the tip**

In the third step, we truncate the AFM tip from the front side. This process consists of two steps, the rough cutting stage and the fine cutting or polishing stage. In the first stage the triangular tip is removed with upto a height slightly larger than the target truncation depth, as shown in Fig. 3.12a. A larger current of 1nA is used to cut most of the material of the tip in a shorter time. In the second step the truncated surface is polished with the smaller current, as shown in Fig. 3.12b. Because of the finite size of the scanning area, this process also involves removing some extra material after the first stage, thereby truncating the tip to the target height. For larger truncations of around 8 μm, the tip width is much higher (order of 3-4 μm).Hence the current can be set a bit higher to 4nA for the first stage and 0.3nA for the second stage, so that the total time can be maintained at 3-4 minutes. In that case we should keep the margin truncation height a bit larger for the first stage to avoid truncating more height with larger current. We also find that the truncated surface of the tip has more material at back surface of the tip than the front. The cause of this is that, while shooting the ion beam from the front, the ionised surface of the already truncated part of the tip repels the ion beam away from the surface, giving rise to the extra material at the back shown in the right picture of Fig. 3.12a. Although this slope seems to be slightly removed with the polishing, the cross-section images in Fig. 3.12c show the presence of extra material on the backside. This can be removed by milling from the side of the tip, and will be taken into account in the future processes.

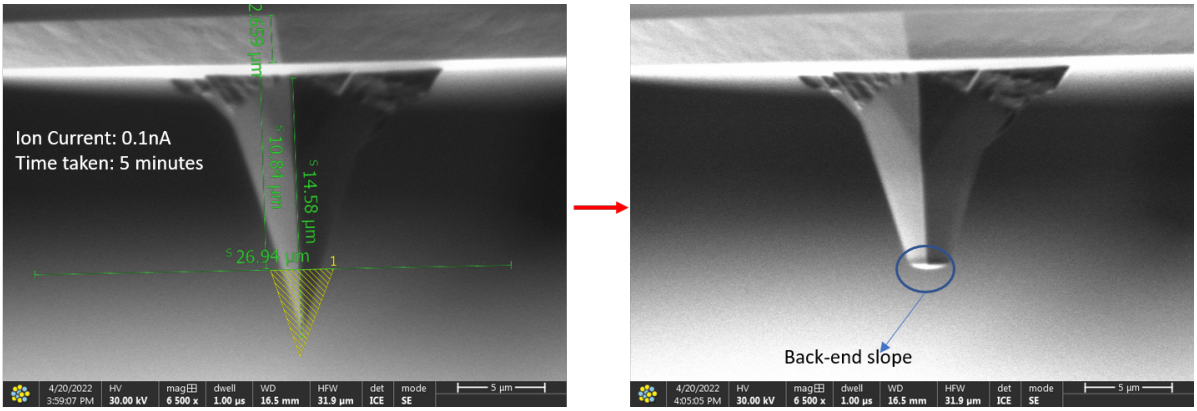

(a) Step 1: First cut removing most material at the tip (FIB Image)

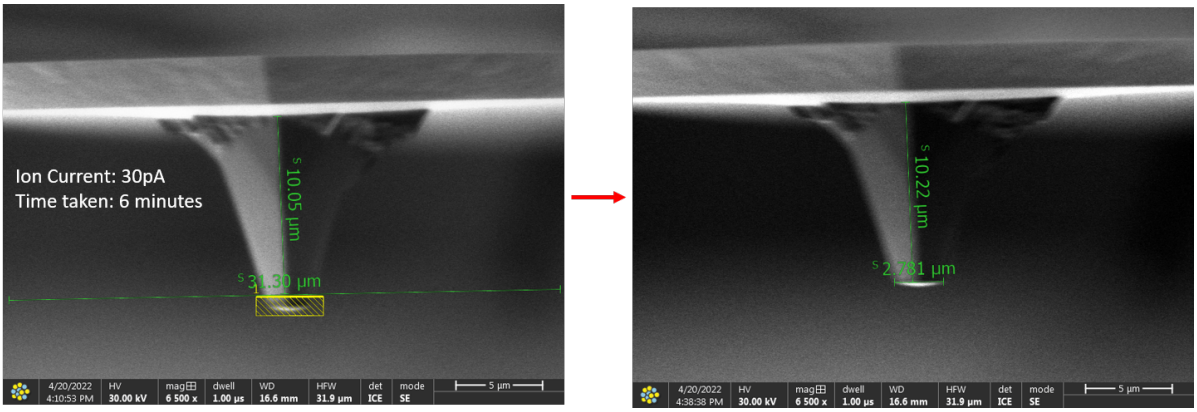

(b) Step 2: Second cut for smoothing the truncated tip surface (FIB Image)

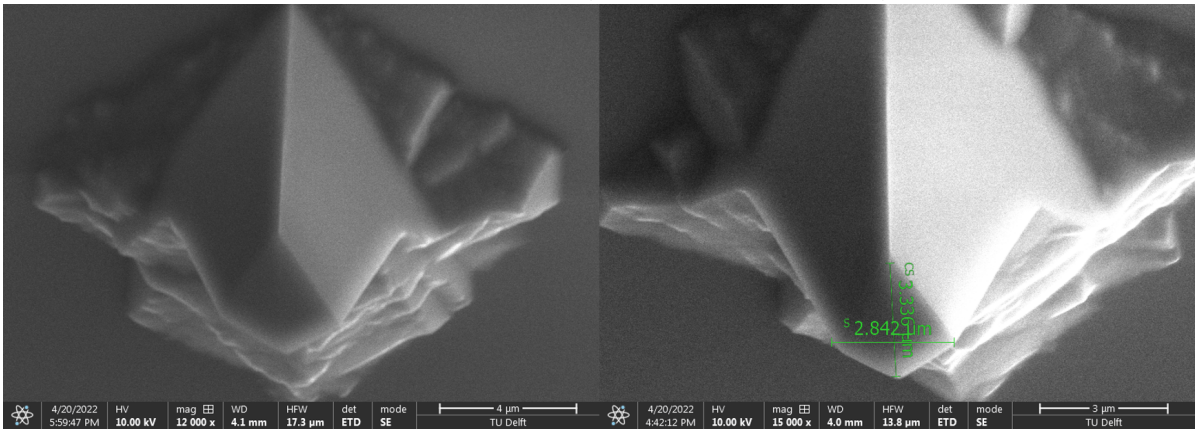

(c) SEM Images of Truncated tip surface

Figure 3.12: Steps for truncation of AFM tips

- **Step 4: Fabricating FZPs on tip**

  The final step is to design the FZPs on two of the AFM tips with different truncation levels as focal depths. The design parameters of the FZP are selected for each truncation depth from the design space in Fig.2.6. The minimum feature size for focal depths above 11 μm range from 270-300 nm, hence these FZPs are easily fabricated with 10pA current and a penetration depth of 100 nm. Before fabrication, the top surface of the AFM tip is brought into focus of the ion beam, which is approximately at a working depth of 4mm from the electron gun and 16.5 mm from the ion gun. Then the scanning area of the concentric zones is specified by aligning the centre of the zones with the tip using the edge markers and the end of the tip (Fig. 3.13a), followed by generating the FZP patterns (Fig. 3.13b). The milling time for each FZP is around 20 minutes. Sometimes we find that even with 10pA and 110nm depth, the FZP might still turn out to be a bit irregular on

the edges (Fig. 3.15), in case of which it is advisable to try higher current of 30 pA or 120nm penetration depth.

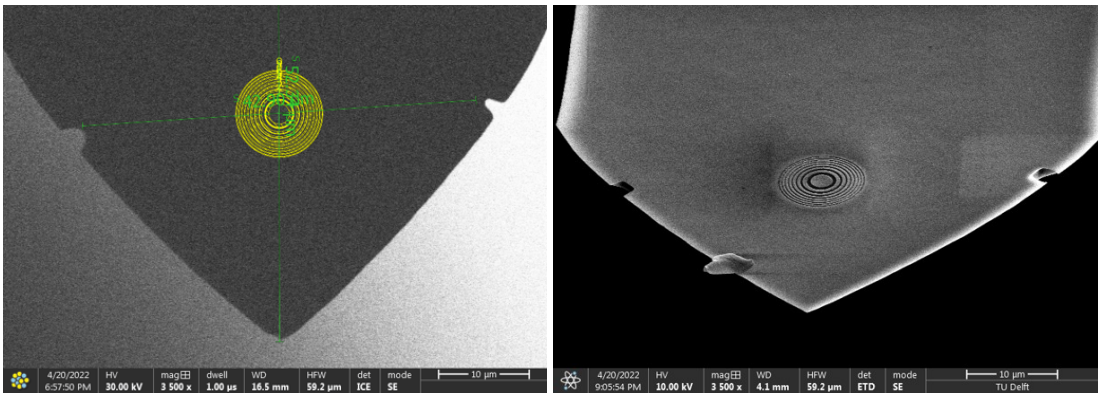

(a) Aligning the centre of FZP rings using edge-markers (b) SEM Images of FZP on tip

Figure 3.13: Adding FZP on tip

Fig. 3.14 compares the measured dimensions of the truncated tip with the estimated dimensions from the axi-symmetric tip calculations. The base size of the tip is measured between 4.73-4.75 μm, which is similar to the estimated pump spot at focus. The measured dimension of the tip surface is given by the length of the smaller axis of the cross-section of the pyramidal tip (Fig.3.12c and Fig. 3.15)). We find that the measured tip-width agrees well with the axis-symmetric calculations of the tip. Fig. 3.15 shows a schematic of the truncated samples on the holder. These samples will be used for the first experiments to detect an the acoustic signal from the tip and compare the amplitudes with and without the FZP.

Cantilever	Total height(μm)	Truncation Depth (Calculated) (μm)		Desired Tip Width (μm) (Diameter)	
		Calculated (focal depth of FZPs)	Measured (Smallest Dimension)	Calculated	Measured (Smallest Dimension)
1	14.73	8.95	8.822	3.71	3.528
2	14.91	8.95	8.970	3.78	3.528
3	14.81	10.33	10.31	2.86	2.823
4	14.50	10.33	10.22	2.72	2.781

Figure 3.14: Table for fabricated and calculated dimensions for the truncated tip. All heights are without the thickness of the cantilever (2.5 μm)

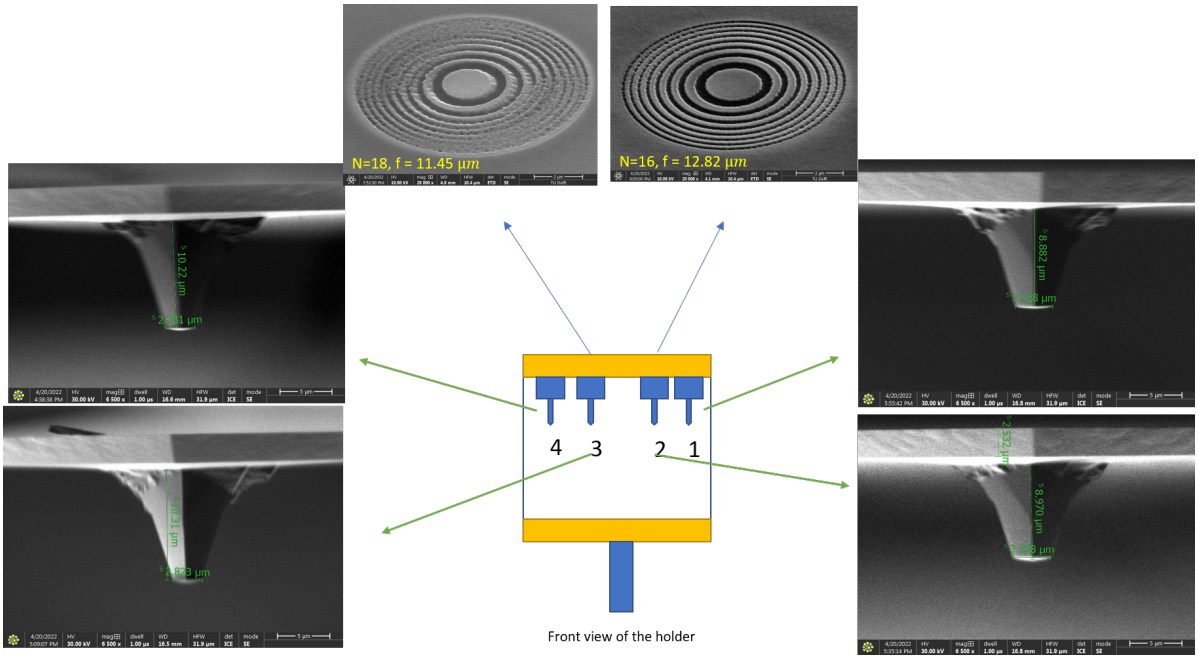

Figure 3.15: Summary of truncated tips and FZPs on them

4

Experimental Methods

In this chapter we discuss the Experimental methods that are followed in this work. We first describe briefly the fundamental principles of the Picosecond Ultrasonic Setup, followed by the modifications that were performed in order to improve the amplitude and sensitivity of the reflectometry signal. Thereafter we discuss the data analysis method performed on the measured signal.

4.1. Setup Description

The setup for measurement of the acoustic echos with picosecond time resolution consists of two main physical phenomena. First the bulk acoustic waves are generated inside the AFM Cantilever using the principle described in subsection 4.1.1. Then the reflected acoustic waves are detected using a probe pulsed laser as described in subsection 4.1.2 and the signal is digitized using the sampling method described in section 4.1.4. Finally the measurement setup and its working condition is briefly discussed in subsection 4.1.3.

4.1.1. Photo Induced Generation of Bulk Acoustic Waves

The generation takes place when the metal film on the AFM cantilever locally heats up by absorbing energy from a femtosecond pulsed laser (100mW at laser output). This is described in the form of thermal strain pulse for a stress free boundary condition by Profunser et al. [51] and Thomsen et al. [19]. The frequency of the generated acoustic pulse is primarily dependent on the pump duration, Lamé constants and density of the metal film. The absorption depth of the metal film plays an important role in determining the temporal width of the thermal strain pulse.

In the present experiments, we use Si AFM cantilevers with 30 nm Al metal film on its backside. Al and Si is a common combination of materials in commercially available cantilevers. Furthermore the Al-Si interface has good enough matching of acoustic impedance and hence good transmittance. Profunser et al. [51] studied the propagation, reflection and transmission of the acoustic pulse at the metal substrate interface, for 4 different metal films (Al,Pt,Cu,Au) and showed that Al can efficiently generate acoustic waves from laser pulse absorption. Si is also good as a material for the cantilever tip in this case because of its low absorption of optical signal for the pump wavelength, low attenuation for acoustic waves and compatibility with other Silicon samples widely used in the semiconductor Industry.

4.1.2. Detection using Beam Distortion Detection and Conoscopic Interferometry

The detection of the acoustic signal is sensitive to the change in surface profile of the metal film caused by the reflected acoustic pulse, and is done using a probe laser which is perpendicularly incident on the metal film of the cantilever. It is based on the principle of divergence of the reflected beam wavefront due to photo induced curvature of the metal surface as a function of acoustic displacement. A diaphragm is used to truncate the probe beam wavefront reflected from the sample, and causes a variation in power with different divergence angles of the reflected beam. This technique is called Beam Distortion Detection (BDD). It is demonstrated by Chigarev et al.[48] that with this method, the SNR is significantly stronger if acoustic wavelength is much larger than the probe signal penetration depth. Also the BDD

signal is less sensitive to acoustic and thermal instabilities.
The SNR of the acoustic signal is further amplified by using the principle of Common-Path Conoscopic Interference. Liu et al. [52] used this novel technique by focusing the probe beam on the sample and passing it through a thin birefringent crystal, which creates a conically varying retardation in the probe beam, with an SNR improvement of 15 dB compared to the standard reflectometry setup. For our setup, we use a sapphire plate to create this profile and a Polarizing Beam Splitter is to allows S polarised light to pass, forming a Conoscopic Interference Pattern.A qwarter wave plate (QWP) is used before the PBS to select the pattern which gives the maximum sensitivity using the principle of BDD.

4.1.3. Setup Configuration

The full setup configuration is shown in Fig. 4.1. The pump and probe are two femtosecond Erbium lasers from Menlo Systems, with wavelengths of 1560 nm and 780 nm respectively, and 100 mW average power. The pump laser has repition rate 100 MHz and and the probe is set 10kHz slower. The sapphire plate receives the probe beam at different incident angles and by blocking the p-polarised component using the Polarising Beam Splitter (PBS)), generates the Conoscopic Interference Pattern (CIP). The Quarter Wave Plate is used to vary the polarization of probe beam to change the CIP, by controlling its fast axis orientation. The s-polarized component from the PBS is detected in the Visible (VIS) camera and the photodetector. The 8/92 Beam Splitter slightly reduces the intensity of the probe Beam by sending most of its intensity to objective towards the sample, and reflects only 8% towards the IR camera. The Dichroic Mirror allows transmission of the probe wavelength but reflects the pump wavelength, enabling them to be incident on the cantilever (sample). The IR camera is used to set the correct alignment of the pump and probe beam spots, whereas the VIS camera is used to set the alignment between the probe beam on the cantilever and CIP. The diaphragm is used to generate the BDD signal as discussed in section 4.1.2 and maximise the SNR by controlling it's percentage opening. The Dichroic Mirror shown in Fig. 4.1 are actuated by a Inertial Piezo-driver which is based on stick-slip motion. Because of varying friction between the drive shaft and the piezo, the motor has some backlash, which is a potential issue in maintaining the repeatability of the probe spot position around the 2D plane of the cantilever surface. Hence it is necessary to make an automatic calibration/feedback between the number of steps on the motor and the corresponding position of the pump and probe spots detected on the camera. In this regard, image recognition techniques can be implemented using the pump beam position as reference and measuring position of the probe beam for gradual steps of drive motion.

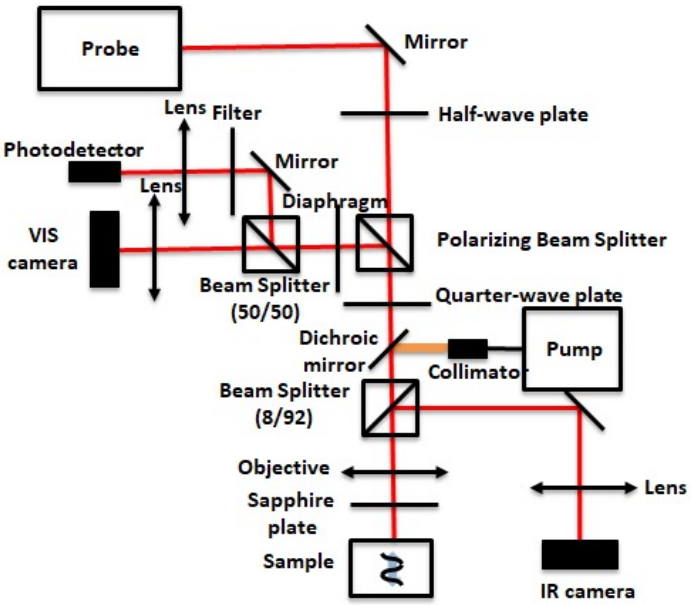

Figure 4.1: Present setup for Measurement (**M. Robin et al. Manuscript In Preparation**)

Further details and further updates regarding the setup and its alignment techniques can be found in

the manual of Martin (**M. Robin et al. Manuscript In Preparation**).

4.1.4. Electronics

The measurement of the Thermal and acoustic pulse and reconstruction are performed using a high speed Asynchronous Optical Sampling Technique(ASOPs). Here the two mode-locked pulsed lasers have a fixed repetition rate slightly offset to each other, and the resulting time-delay scheme is used to reconstruct the response signal from the sample [53], as shown in Fig. 4.2. Bartels et al. [54] developed a high speed ASOPS system with stable repetition frequency close to 1 GHz, enabling the scanning between two pulse trains over a time window of 1 ns. For the setup, the time window of 10ns between two successive pump pulses is reconstructed using an offset frequency of 10 kHz between the pump and probe laser. This allows for measurement of this 10ns window in 100 μs. In order to extract the thermal and acoustic signal from the probe pulses, a Lock-In Amplifier with ultra-high Bandwidth of 600 MHz from Zurich Instruments is used with the Boxcar and Periodic Waveform Analyzer option [55].

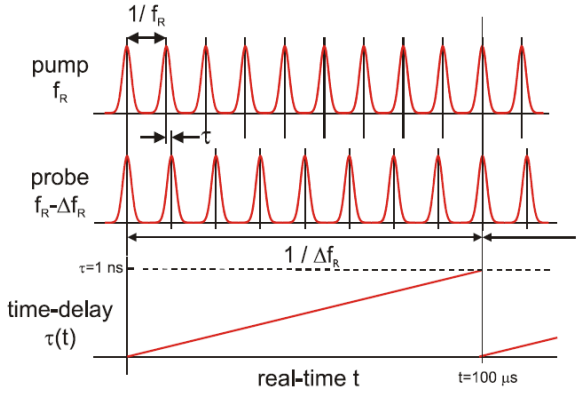

Figure 4.2: Schematic Sketch of ASOPS time-delaying principle with two fs pulse lasers [53]

4.2. Modification of Experimental Setup

In this section, we discuss certain modifications that are made in the setup to increase the signal-to-noise ratio of the acoustic signal and to be sesnsitive enough to detect acoustic echoes at the tip. The amplitude of the generated acoustic signal depends on the pump laser power density on the surface of the sample. The intensity of the detection signal, or the change in reflectometry at the surface depends on both pump and the probe laser power densities. With the initial setup configuration, we were unable to detect the lower intensity acoustic echoes from the truncated AFM tips (shown in Chapter 3). Therefore we attempt to set the pump and probe power densities (W/m^2) as comparable with the measurements of Bryner et al.[21], who could measure the acoustic echoes at similar tip truncation heights. The pump and the probe beam are focused on the sample using an 20x magnification objective lens upto a spot size of 9-10 μm, as opposed to 3-5 μm reported by Bryner et al. The powers are measured using S120C sensor integrated with a PM1000D console. The pump power on the objective is 31mW as compared to that of 10mW for Bryner et al. which is a factor of 2 smaller in power density. The power on the photodetector cannot be increased beyond 50μW due it's optical saturation limit, thereby limiting the power density to the order of 100 times smaller than Bryner et al. In the following sections we introduce a few techniques to increase the pump and probe power densities and increasing the SNR of the reflectometry signal.

4.2.1. Changing the setup configuration

Here we demonstrate a possible way to increase the pump power. In the previous configuration, as shown in Fig. 4.3a, the pump beam was allowed to pass through the Polarising Beam Splitter (PBS) and the Qwarter Wave Plate (QWP). This caused the pump beam to loose a significant amount of power before it reaches the objective lens. Measurements show that around 35-40 % of the total pump power at the fibre collimator enters the objective. Hence we move the pump collimator and the SP 950nm dichroic mirror after the qwarter wave plate, as shown in Fig.4.3b. By doing so, we find an increase in pump power from 35mW to 69.6mW, which brings it's power density at the same order as Bryner

et al. However the surface power density of the acoustic signal also depends on the absorption of the pump power in the sample. For the present setup the absorption coefficient for 1560nm pump laser in aluminium is 2.5%, which is 5 times less than that of the 800nm pump laser used by Bryner et al (13% absorption coefficient).

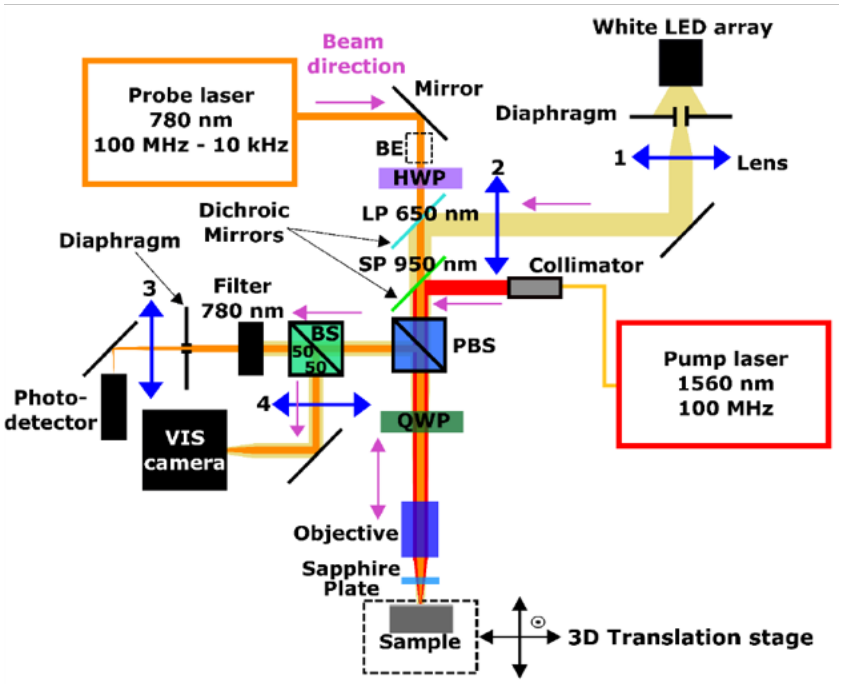

(a) Old configuration

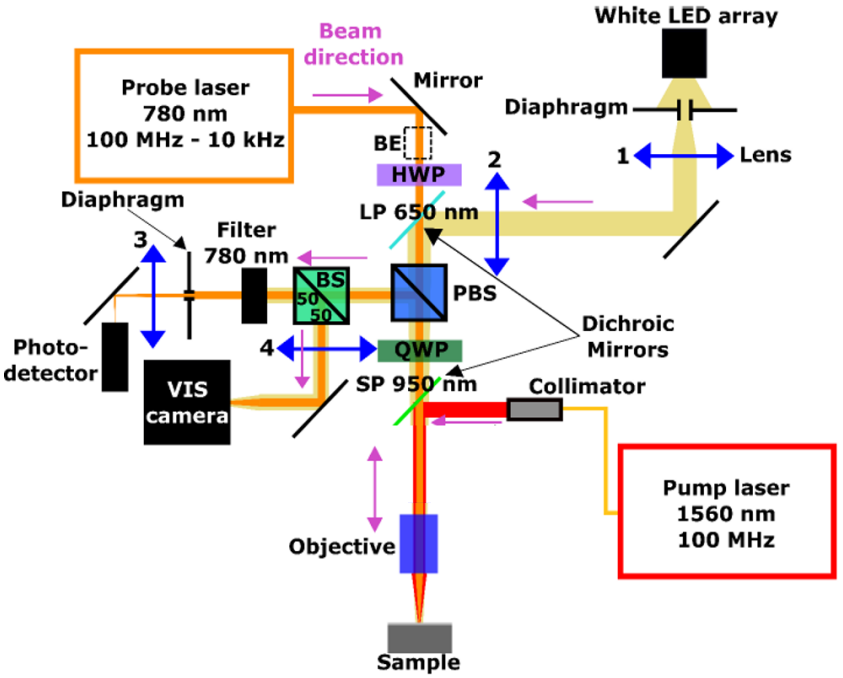

(b) New Configuration

Figure 4.3: Old and changed configurations of the setup (see Martin's Manual(**M. Robin et al. Manuscript In Preparation**)). The blue arrows indicate the direction of polarisation, except for the one where all polarisations are present, and it doesn't as long as we can use it to see a picture of the sample on the camera

Fig. 4.4 shows the modulated probe pulses in the old and new configuration. With the same probe power, we find that the increase in pump power leads to a factor 2.3 rise in thermal peak. For both

the cases, the noise level remains the same and all 6 echoes are clearly visible on the 2.5 μm thick cantilever body in a time window of 4ns as expected. Fig. 4.5 compares the first 6 echoes on the cantilever body for the old and new configuration. The echoes for the for the new configuration vary approximately 1.3-1.5 times higher than that of the old configuration. Although the fluence of the pump beam on the sample is the same order as that of Bryner et al., the acoustic wave generation is still smaller due to 5 times smaller absorption for a pump wavelength of 1560 nm in our setup (compared to 800 nm in Bryner et al).

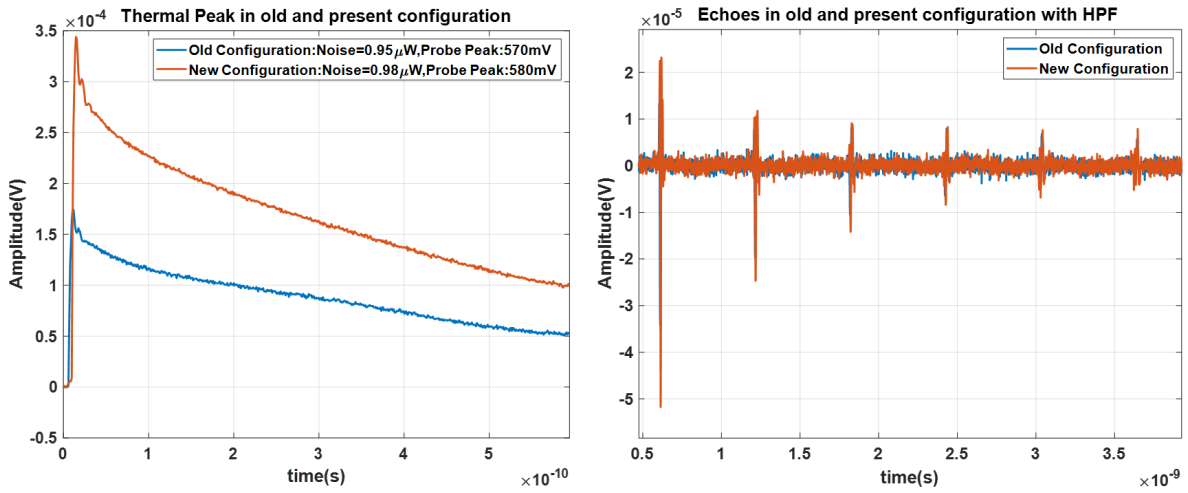

Figure 4.4: Comparing thermal peak and echoes of the old and new configuration. The signal on the left figure is high-pass filtered to remove the disturbance signal due to the detection algorithm. Note that the time axis is continuing from the left to the right figure. To compare the echoes in the old and new configuration, a zoomed in figure of each echoes is presented below

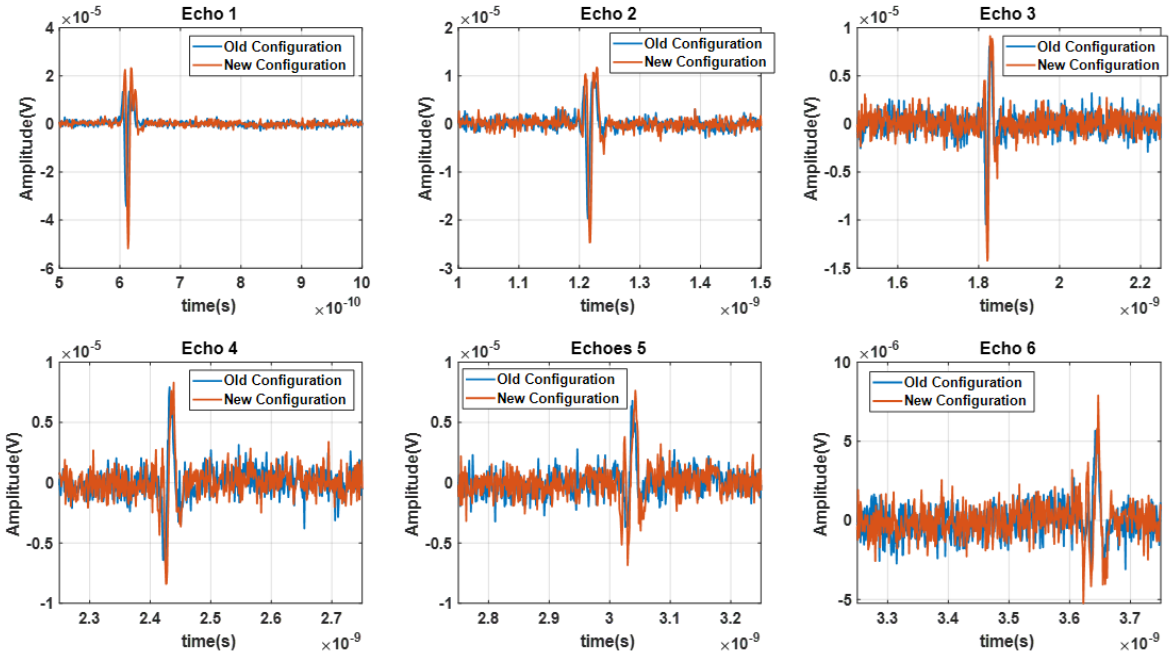

Figure 4.5: Comparing first 6 echoes of the old and new configuration.The signal is high-pass filtered to remove the disturbance signal due to the detection algorithm.

A downside of this configuration compared with the old configuration is that, a very weak pump power reaches the visible camera, due to most of the pump polarisation being cut off by the PBS and QWP. Therefore it requires the illumination system to be turned off, and a higher exposure time (around

350ms) and gain level (16-20) on the camera to see the pump power. This makes it a bit harder to align the pump and probe spots on the cantilever body without the illumination system, so we do most of the alignment by optimising the thermal peak.

4.2.2. Unamplified Photodetector

In the measurements of Bryner et al., a probe power of 2mW was used on the sample within a spot size of 3-5 μm. In order to have the same probe power density in a spot size of 9-10 μm, we should therefore have a probe power ranging from 8-12 mW. We measure a probe power drop by a factor of 4-4.5 from the objective to the photodetector, implying that we require a power of approximately 1-2 mW on the photodetector. However with the current photodetector, Fig 4.6 shows that the the thermal peak already decreases when the probe power is increased to 80 μ W or more, impliying that the photodetector is already saturated around 100 times below the power requirements. Secondly the amplifier of the old photodetector is a noise source(6pW/$\sqrt{Hz}$), shows that the noise level almost increases by a factor 2 as near the maximum pulse amplitude of 1V.

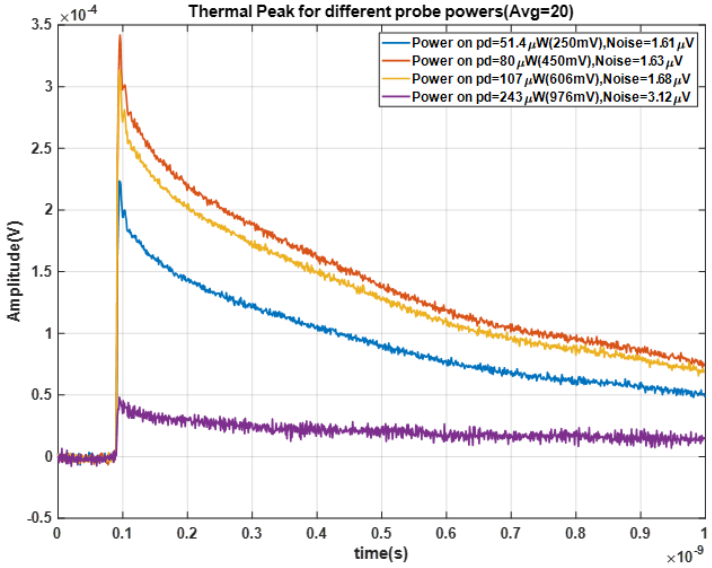

Figure 4.6: Comparing thermal peak and noise with increasing probe powers for the old photodetector

In order to resolve this issue, we replace the FPD510 photodetector with an un-amplified photodetector DET10A2 from Thorlabs with a high optical saturation threshold of 25mW and an NEP of 5fW/$\sqrt{Hz}$ without the amplifier. Also the new photodetector has a 1mm diameter active area, which is 2.5 times higher than the old one, thereby facilitating easier alignment lesser chances of truncation of the probe beam. In absence of the amplifier, the probe pulse amplitude is the voltage across the 50 Ohm impedence of the lock-in amplifier, which is much lower than the old photodetector. Fig. 4.7 shows the thermal peak and the probe pulse with the DET10A2 is 9-10 times smaller than the FPD510 for a 5.6 times larger optical power. Apart from the ability to reach higher optical powers, we also gain a higher SNR in the acoustic echoes, with around 1.7-1.8 times larger signal and approximately 4.5 times smaller noise level with same number of averages.

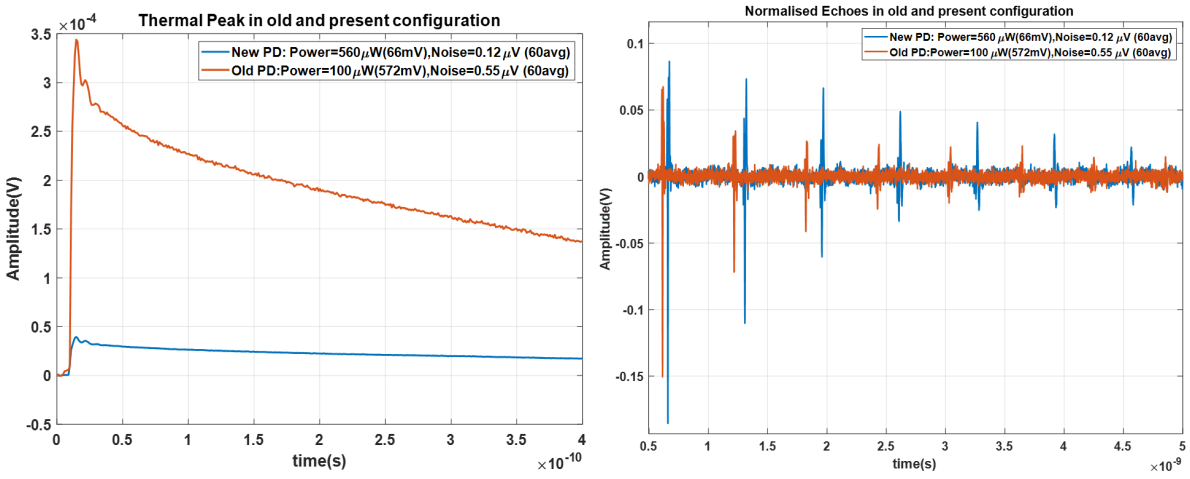

Figure 4.7: Comparing first 6 echoes of the old and new photodetector. The right figure is the thermal peak and left figure are the echoes filtered with HPF and normalised with the thermal peak

From the measured signal of the first 6 echoes on the cantilever body, we estimate the echo amplitudes at the truncated tip (Fig. 4.8). This is done by scaling the echos on the cantilever body with the tip-scaling factor (section 2.4.1) for the surface area at the corresponding truncation depth. Because the scaling factor is applied directly on the measured echoes, the attenuation in Si in the truncated tip is already taken into account in this hypothesis. We find that with the same number of measurement averages as that on the cantilever body, the signal at the tip is 3-4 times above the noise level at 11-12 μm (3.2 μm tip diameter) truncation depths. Hence the AFM tips can be truncated upto these depths in order to find a signal without the FZP. For the signals beyond 13.5 μm, we can reduce the noise level by increasing the number of Boxcar averages (noise level $\propto 1/\sqrt{\text{Number of averages}}$), which also increases the measurement times upto 4-5 hours. Furthermore, for larger truncation heights beyond 13.5 μm , we expect to have 3-4 times higher signal with the FZP from the simulations. (section 2.5.2).

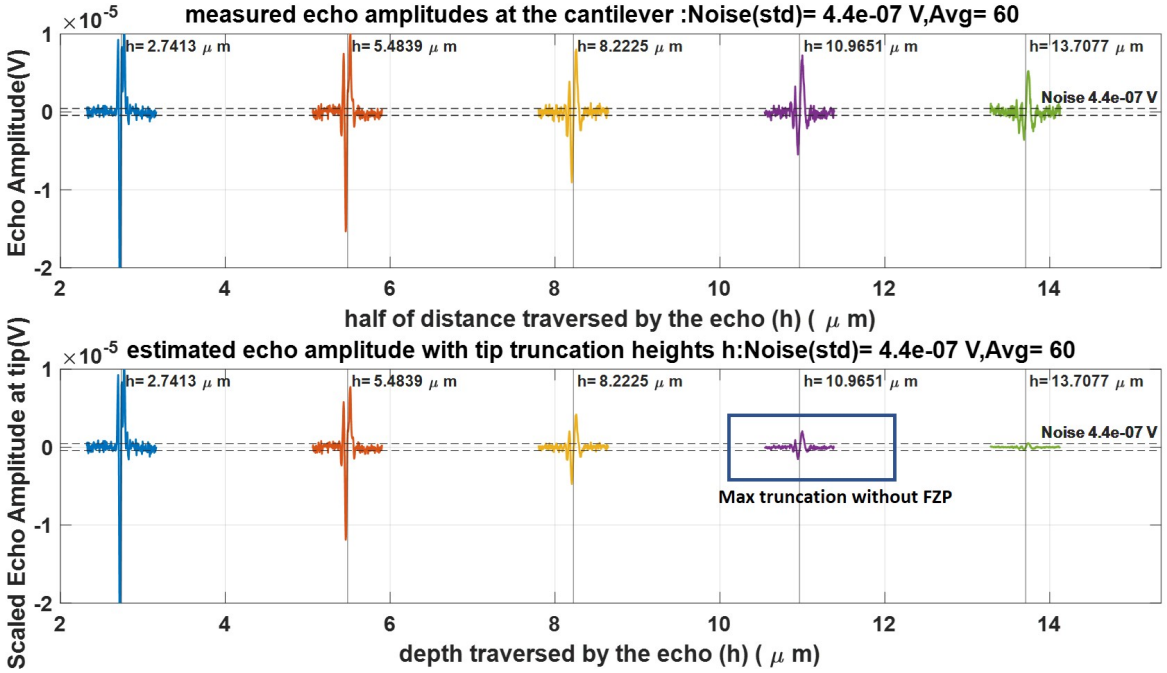

Figure 4.8: Estimating echo amplitude at the tip without the FZP using measurements on the cantilever body with the new photodetector. The top figure shows the first 5 echoes measured on the cantilever body. The bottom figure shows the scaled echoes for the same distance traversed in the truncated tip. The total height of the tip including the cantilever body is assumed to be 17.05 μm in this case

It should be noted that the new photodetector and the new setup configuration is installed much later in the project period, and the first two parts of the results (sections 5.1 and 5.2) will show the measurements with the old configuration.

4.2.3. Pump-probe Alignment on FZP

The pump and the probe beam are aligned with respect to each other to reach the maximum thermal peak, the details of the alignment procedure is discussed in **Martin's manual(M. Robin et al. Manuscript In Preparation)**. Here we discuss a possible strategy to align the pump and the probe spot on the FZP, so that the centre of the pump spot is roughly at the centre of the rings. In this regard, we first align the pump and probe spot outside the FZP to reach an optimum thermal peak. Thereafter we sweep the sample at different locations on the FZP as shown in Fig. 4.9a and 4.9b, until we reach a maximum thermal peak. Fig. 4.10a and Fig. 4.10b shows the pixel locations in x and y axis where the thermal peak is optimum. The principle behind this strategy comes from the fact that the FZPs have a higher temperature due to smaller heat conduction in alternate rings of Al and Si, as compared to a continuous Al film (demonstrated in the results section 5.1). We expect that the effective heat conduction in the FZP is worst when the maximum energy of the pump laser spot is absorbed by the central zone of the FZP, thereby leading to the maximum temperature rise. By comparing the optimum pixel locations in Fig. 4.10a and Fig. 4.10b, it may seem on the camera that pump and probe spots are slightly offset from the centre of the FZP. However this might only be due to the fact that the pump and the probe beams are incident and reflected slightly at an angle on the sample, and thereby are laterally offset on the camera compared to reality.

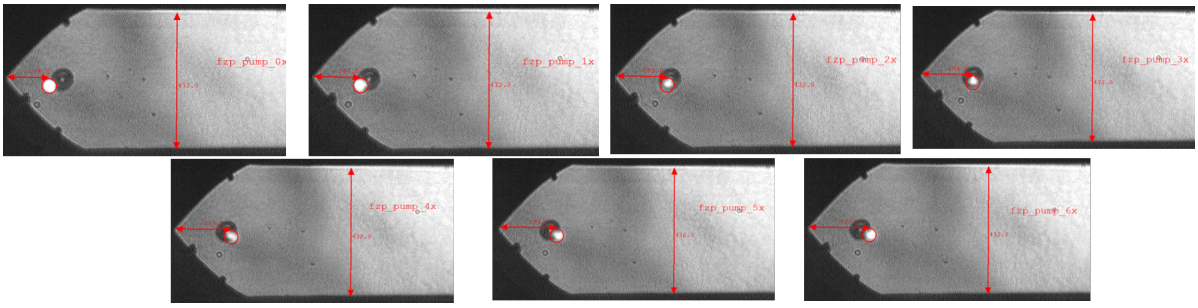

(a) x sweep of the pump

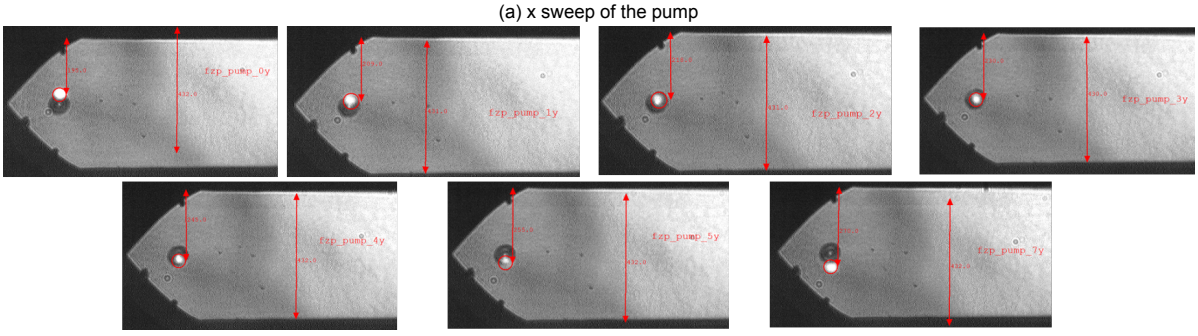

(b) y sweep of the pump

Figure 4.9: Sweeping the sample to move pump and probe spots on the FZP for optimal alignment. The position of the pump is measured by the number of camera pixels

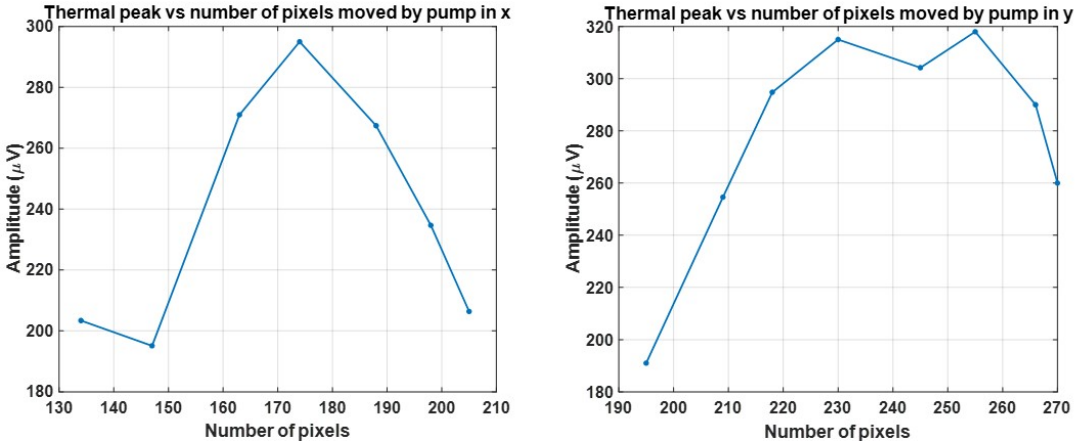

(a) x sweep of the pump

(b) y sweep of the pump

Figure 4.10: Thermal Peak and variation with pixel position of pump on FZP

In case the pump laser is not visible in the new configuration (section 4.2.1) with the camera settings with the illumination system off, it can be first aligned and marked with respect to the probe beam outside the FZP. Then the pump-probe spot can be aligned on the FZP using the method described above.

4.3. Data Analysis

In this section, we discuss the data analysis method used to predict the amplitude and profile of the acoustic pulse from the noisy measurement signal. The estimated amplitude from the fitted model is used to study the variation in reflectometry signal on the cantilever body and the tip with and without the FZP. The signal on the lock-in amplifier has a sinusoidal disturbance due to beating effect in sampling of the pulses during averaging. Hence the signal is always high-pass-filtered with a cut-off frequency of 12-15 Ghz, before performing any functional approximation on the data.

4.3.1. Fitting of Acoustic Echoes

The acoustic echoes measured from the modulated probe signal consists of noise coming from the lock-in amplifier and the photodetector. In order to analyse this data to compare the echo amplitude and shape, we reconstruct them with a non-linear model. In this regard we use the Radial Basis Function Neural Network [56]. These are the simplest forms of feedforward neural networks and are known for their efficient and accurate function approximations. The hidden layers comprise of Gaussian and linear activation functions, also called kernels (Fig. 4.11). The former one fits the shape of the positive and negative peaks and and the latter one fits a linear or constant offset on the data points.

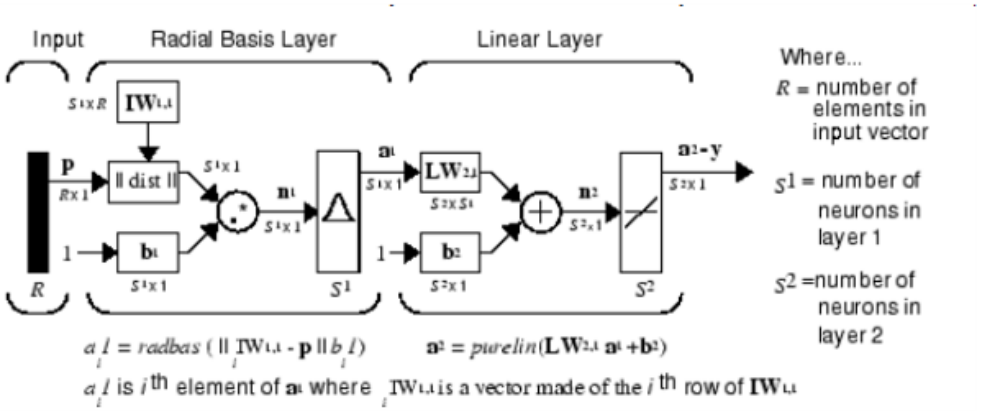

Figure 4.11: Typical RBF Network architecture from MATLAB documentation ([57]). The Radial basis layer comprises of the Gaussian of the euclidean distance between the input layer and weight function,and the linear layer control offsets the location of the RB neurons.

The primary input parameters of the RBF model are the number of neurons or the number of Gaussian kernels, and the spread parameter or the width of each kernel. In order optimise the RBF model, we first fit the data points of the measured echo with different number of neurons, as shown in Fig. 4.12a to Fig. 4.12b. We find that the RBF with 4-5 neurons can optimally fit all the peaks of the acoustic echo over the noise level. Furthermore, we optimise the spread or standard deviation of the RBF neurons by performing a regression analysis between the measured and fitted data points. Fig. 4.13 shows the RMSE and R-squared fits [58] for the regression models with respect to the spread parameters. The optimum spread parameter is used as a constant input parameter in the RBF model

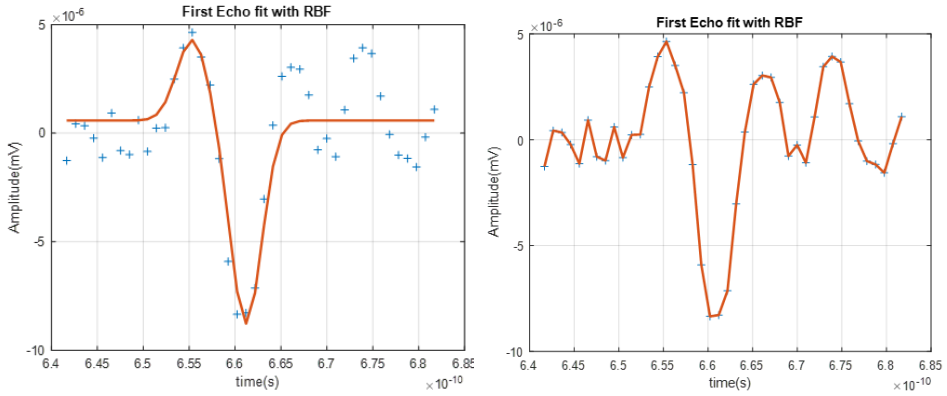

(a) RB with 2 neurons

(b) RB with 42 neurons

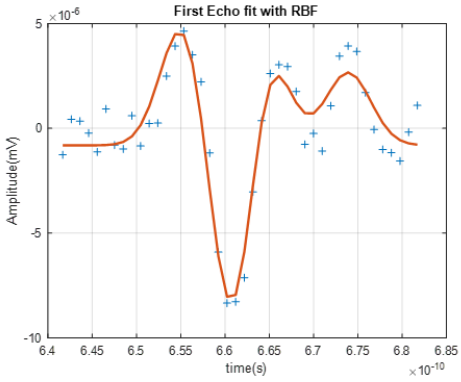

(c) RB with 4 neurons

Figure 4.12: Radial Basis function Approximations with different number of neurons.a)For too less neurons the RBF cannot fit all the peaks in the echoes ,b) For too many neurons, the RBF overfits the noisy data as well, c) Optimum number of neurons for best fit

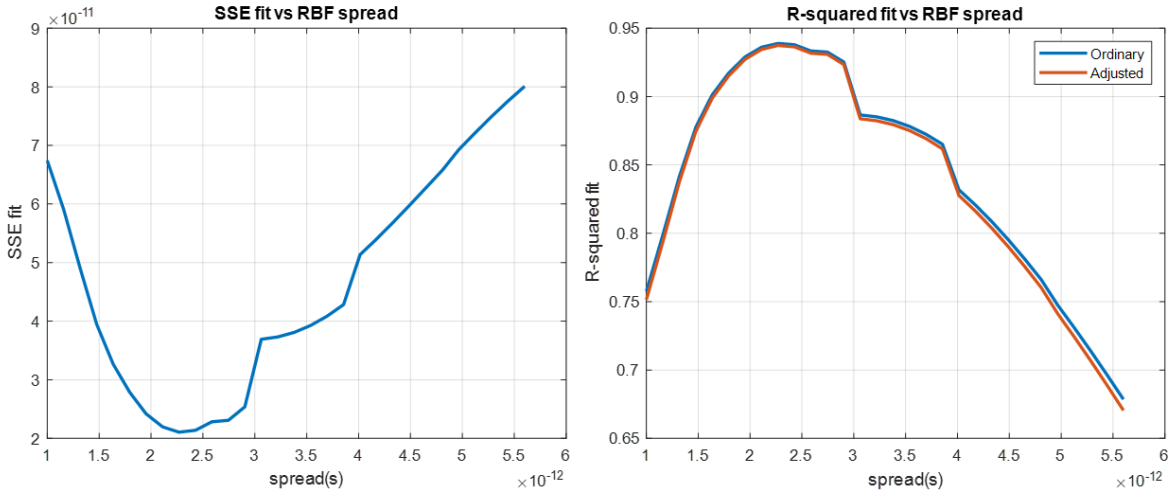

Figure 4.13: Regression analysis between actual and RBF fit to optimize the spread parameter. The optimal spread which gives the minimum standard error and maximum R-squared fit is generally between 20-30 ps

4.3.2. Error Analysis

The functional form of the RBF approximation, representing the fitted acoustic amplitude at each time point is given by:

$$\mathrm{f}\left(t_j, b_i, c_i, w_i\right) = b_0 + \sum_{i=1}^{5} b_i * e^{-\left(\left(t_j - c_i\right)^2 * w_i^2\right)} \left(t_j = t_1 : t_N \text{ are the time points }\right) \tag{4.1}$$

where b_i, c_i, w_i are represent the amplitude, input weights (location of the Gaussian kernels) and spread parameters of the i^{th} neuron. The uncertainty analysis of the fitted model is performed using the Non-linear least squares method, and the correlation between each model parameter is approximated using Gauss-Newton Search Method([59]). The details of this calculation is shown in Appendix A.3. We calculate the standard error of each parameter from the covariance matrix. We find that the parameter b_i corresponds to the peak-peak amplitude of the echoes and hence corresponds to the largest standard error. is also in the same order as the measurement noise in Fig. 4.14

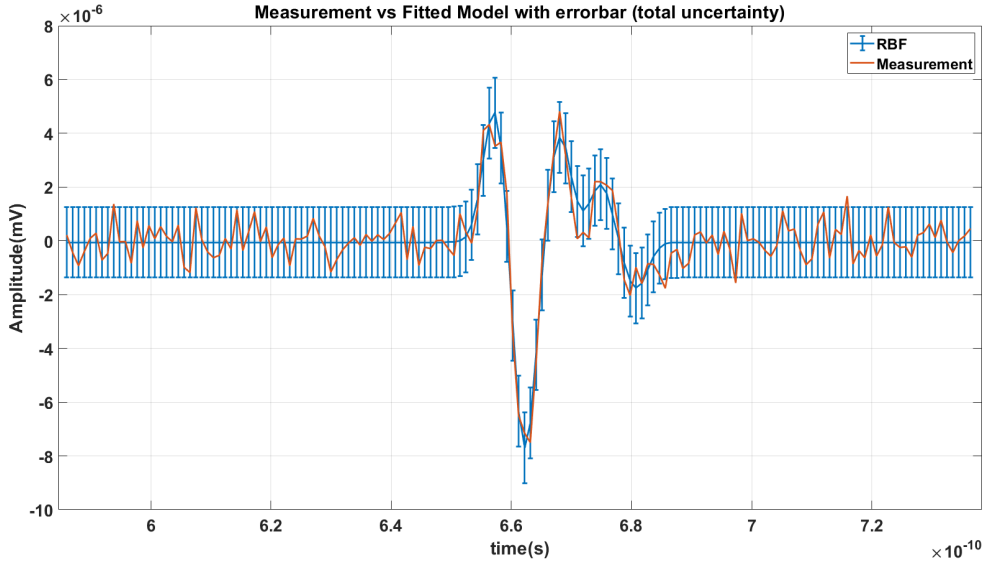

Figure 4.14: Uncertainty analysis of RBF model with respect to amplitude parameters: Standard error = 1.2-1.3e-7, Measurement Noise=1.4e-6

In order to compare the echo amplitudes with and without the FZP, we take the ratio of the peak to peak amplitudes of the signal. Each of these measurements consists of two sets of measurement points on and off the FZP. Therefore we perform error propagation on the ratio parameter with respect to the standard errors of the model parameters (Appendix A.3). These are shown in Fig.4.15. For normalized signals, the parameter uncertainties and the propagated errors are calculated over the normalized datasets and will be discussed further in the results section (section 5.1).

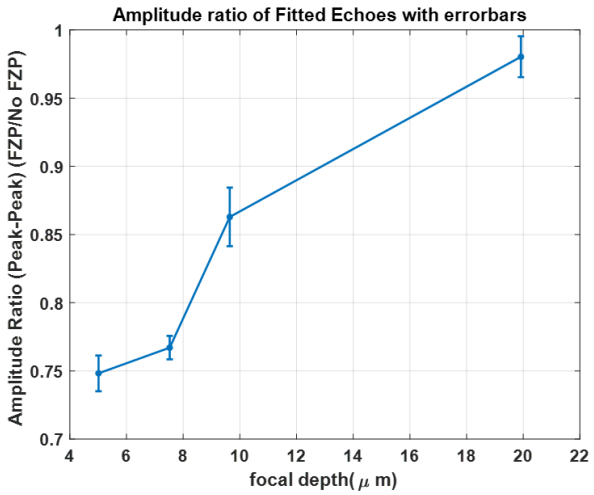

Figure 4.15: Uncertainty propagation for amplitude ratio of fitted echoes for each pair of measurement points (FZP and No FZP). For each focal depth, there are two sets of measurement points, with and without FZP. So we propagate the uncertainty over the model parameters.

5

Experimental Results

In this section we show the results of the measurements on the cantilever body and tip. In order to reduce the effect of the inclination of the cantilever on the detected probe pulse, we measure signals on the cantilever body adjacent to the FZP. We also compare the results of the detected signal with the simulations.

5.1. Measurements on Cantilever Body

We first measure the probe signals from the FZPs fabricated on the cantilever body(sec 3.3.1), ranging from a focal depth of 2t-8t, t being the thickness of the cantilever body. The amplitude of the input signal on the Boxcar is around 285mV with the old photodetector and each measurement is averaged over 120 cycles. Fig 5.1 shows the reflectometry signal detected on and near the FZP, measured over a time window of 2 ns. The thermal peak on the FZP is higher and has a slower decay than that without the FZP, implying that the effective thermal conductivity of the FZP is worse than that of the cantinuous Al film. We find that the thermal peak is the maximum for the FZP with focal depth 2t, and gradually becomes smaller and closer to the continuous Al film with increasing focal depth upto 8t. This is because smaller focal depths also have more zones of lesser thickness, including a smaller central zones.

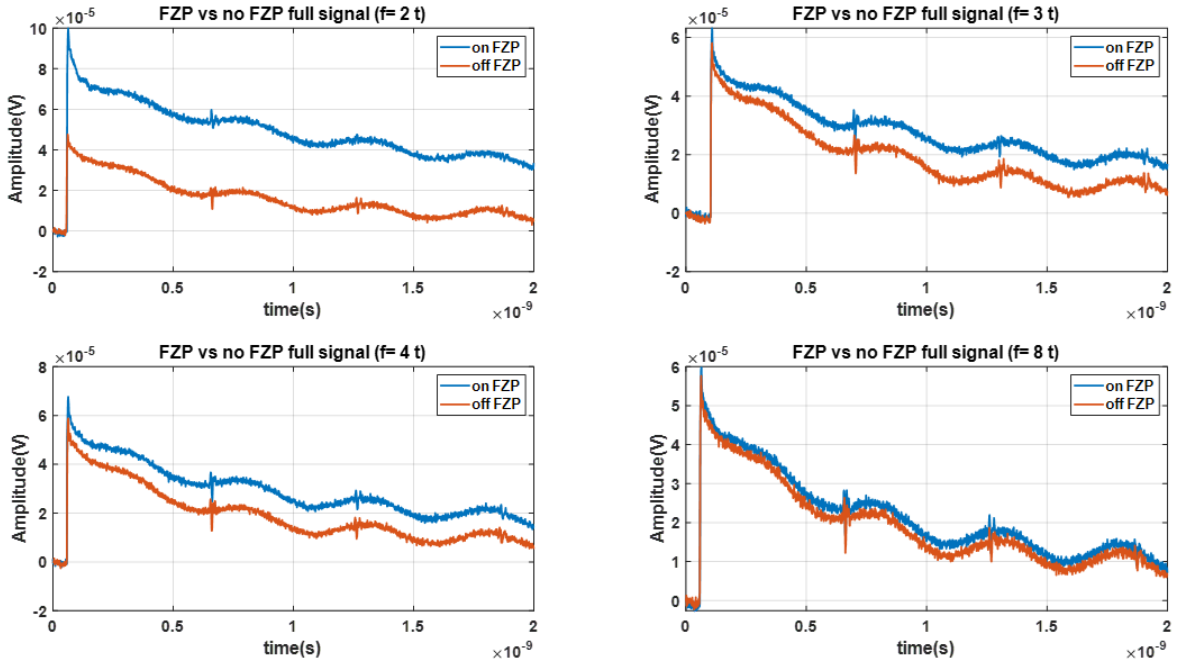

Figure 5.1: Thermal peak and echoes on cantilever body. The FZPs range from focal depths 2t-8t, t being the thickness of the cantilever body

We study the reflectometry signal of the first acoustic echoes on and near the FZPs, as shown in Figures 5.2a through 5.2d. In order to remove the effects of diffraction and truncation of the probe laser on the FZP, we normalise the the echoes with respect to the thermal peak. This is also expected to remove the effect of the additional heat generation due to bad thermal conductivity on the FZPs. We find that in all cases the main amplitude of the signal above the noise level consists of 5 distinct peaks. For the FZPs the first positive peak has a higher relative amplitude than the other positive peaks, as compared to the signals without the FZPs. The larger negative peak (off the FZP) also has a smaller relative magnitude on the FZPs. This effect is more prominent for the focal depths 2t and 3t, and for higher focal depths, the pulse shape gradually becomes more similar to the echoes without the FZP.

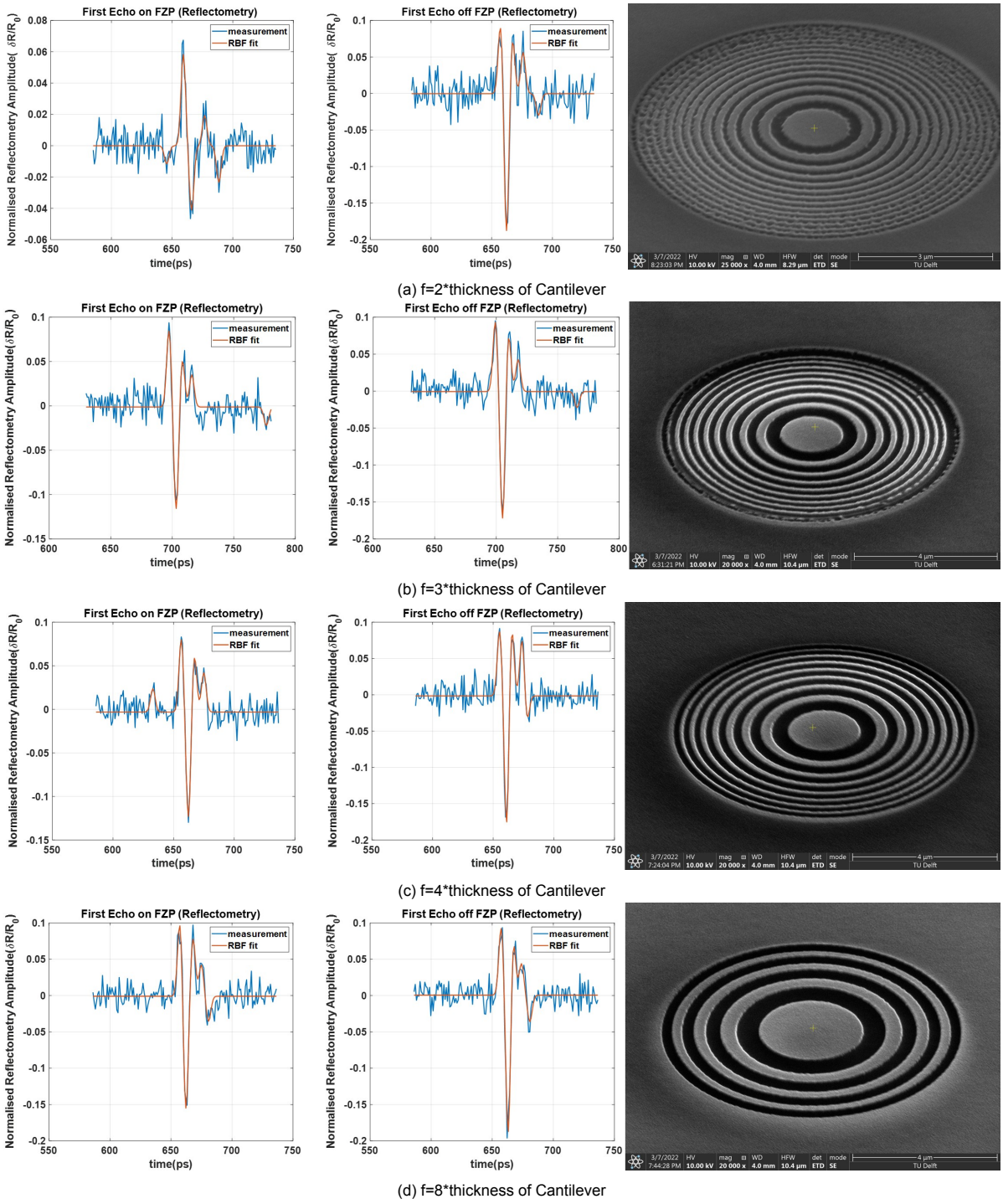

Figure 5.2: First echoes on good FZPs with focal depths ranging from 2t-8t, t being the thickness of the cantilever body.All amplitudes are normalised by the thermal peak

We can infer that the FZPs may cause a change in shape and frequency content of the acoustic pulse, as the waves diffracted from the outer zones interfere with the central part of the acoustic wave with a phase delay. This is because near 2t, the acoustic pulse is expected to focused back to the surface of the FZPs, and with increasing focal depth, the signal deviates from the focused wave profile and is closer to the plane wave at excitation. The pulse shape can be therefore used to further study the acoustic profile at focus.

We also study the signals from the FZPs that are distorted during the fabrication. These are particularly the ones with smaller focal depths from t-3t, for which the current and the depths settings of the focused

ion beam were not optimised. These are shown in Figures 5.3a through 5.3b.

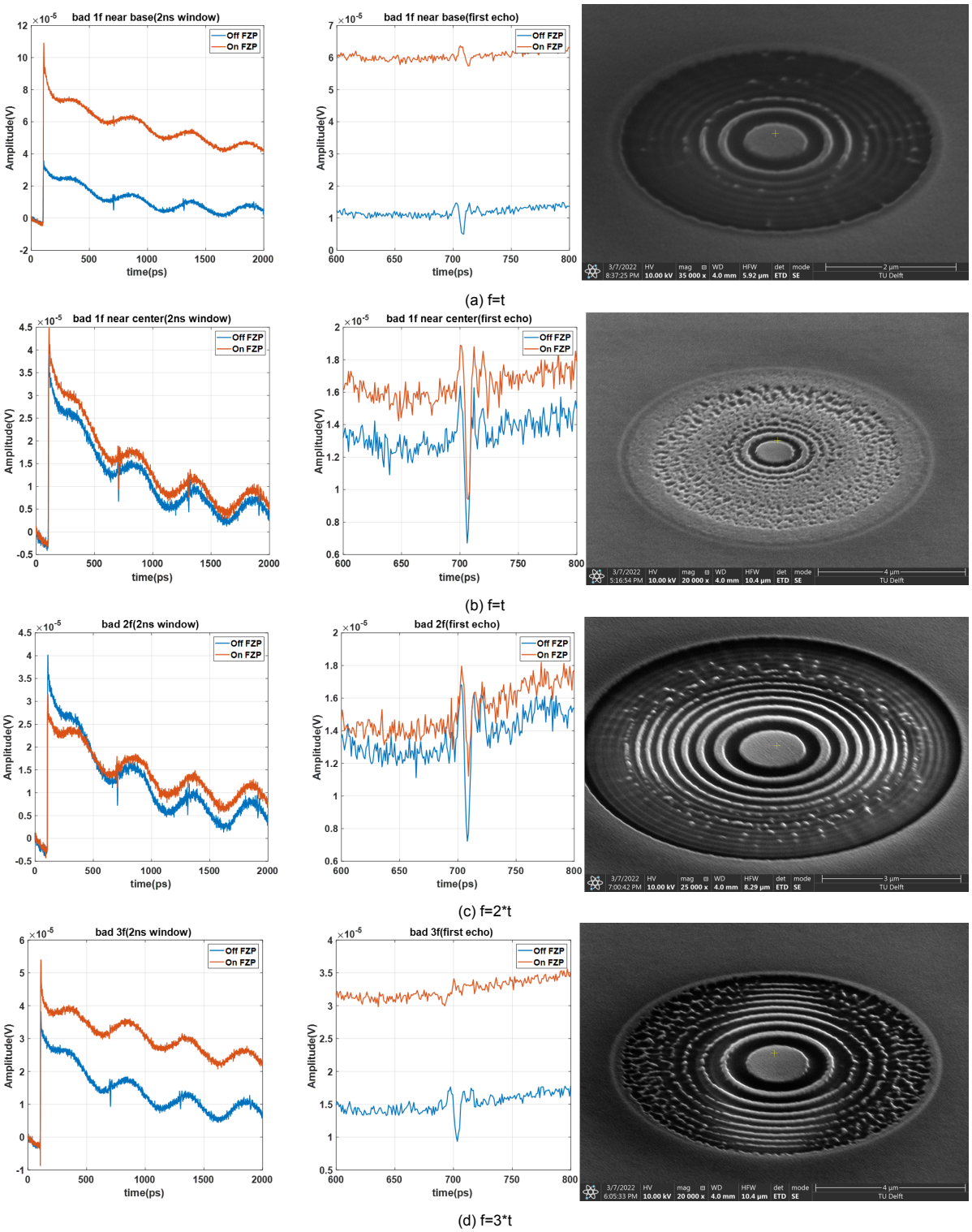

Figure 5.3: Measurements on the bad FZPs, for focal depths ranging from t-3t, t being the thickness of the cantilever body

The reflectometry signal from the same FZPs depend highly on their fabrication. As shown in Fig. 5.3a the first design for f=t has most of the aluminium removed by higher current, so the generated signal is almost a factor 3 smaller than that outside the FZP. For the second FZP in Fig. 5.3b a smaller current removed most of the aluminium on the outside the central zones, and therefore the signal has a similar

shape as that outside the FZP. This is also the case for f=2t in Fig. 5.3c, where the pulse shape has a smaller positive peak and a larger negative peak. This is different from the FZP in Fig. 5.2a where all the middle and outer zones are properly patterned but all the zonal edges are more irregular, and the signal has a relatively higher first peak. However the signal amplitude for the latter case is much smaller, implying that the design of the central zones are more important in retaining the amplitude of the signal, and the outer zones are responsible for the focusing of the acoustic pulses and having an overall influence on it's shape. This is because the central zones absorb most of the pump power and generate more acoustic energy. Presently the size of the FZPs are almost twice the pump beam diameter (3-5 μm according to Bryner et al.[21]) to absorb 90% of the pump power. But they could also be designed smaller (within the fabrication limits) so that the the outer zones can focus higher energy acoustic waves, thereby contributing more to the signal amplitude.
Finally, we compare the measured normalized reflectometry signals on the FZPs with simulations. We normalize the reflectometry signal with the thermal peak in order to remove the effect of generation and probe beam diffraction from the detected signal on the FZP. In order to get rid of the material constant pre-factors and the variation in pump and probe power in different locations of the cantilever, we take the ratio of the measured signals on and outside the FZP. Subsequently, for the simulations, we divide the normalized reflectometry on the FZP by that from a continuous thin film. Fig 5.4a and 5.4b show the variation of normalised reflectometry signal ratio with the Focal depth of the FZPs. Since the diameter of the pump beam is difficult to estimate accurately from the setup, we calculate the reflectometry signals for two different pump diameters, 8 μm and 4.5 μm, the latter one being closer to the measurements of Bryner et al. [21].We find that the simulation results follow the same increasing nature as the experimental measurements, and the reflectometry signal ratio with smaller pump diameter is higher and closer to the measurements. This can be explained by the fact that for smaller pump diameter, the inner half of the FZPs containing more Al receive higher acoustic energy and the outer half receives smaller acoustic energy, compared to the case of smaller pump diameter. As described in section 2.5.1, the signal amplitude on the FZP should approach the signal on the Al film or the amplitude ratio should converge to 1 when the focal depth approaches infinity, or there is 1 zone of continuous Al film.

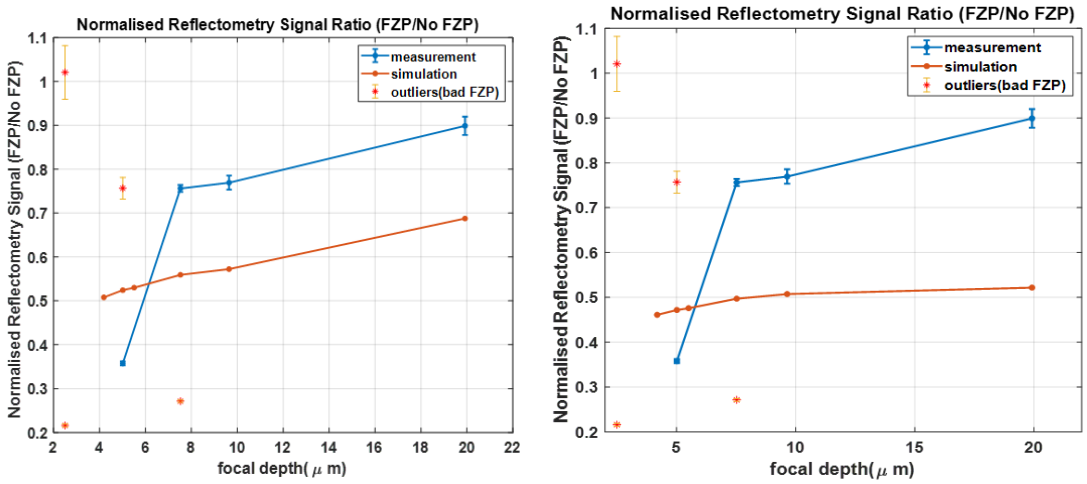

(a) Normalised Echo Amplitude Ratio(FZP/No FZP) for pump spot size r=4.5 μm

(b) Normalised Echo Amplitude Ratio(FZP/No FZP) for pump spot size r=9 μm

Figure 5.4: Amplitude ratio of first echo reflectometry signal between FZP and no FZP. Fig 5.4a: normalised amplitude ratio with $4.5\mu m$ pump spot size in simulations Fig 5.4b: normalised amplitude ratio with $8\mu m$ pump spot size on simulations. For the measurements, the signal is normalised by the thermal peak and for the simulations they are normalised by the input excitation pulse. The improper FZPs are marked as outliers here, and their images are shown in Figures 5.3a-5.3d

It should be mentioned that the normalised reflectometry ratio from simulation are a factor 1.3-1.5 lower than that in the measurements, the probable causes are discussed in section 6.1. Also the measurement on the FZP with f=2t seems to be almost a factor 2 smaller than expected. This can be attributed to the edges defects and the irregularities on the zones.However we find that with the same design, the improper FZP (outlier at 5 μm) follows a more consistent trend with the rest of the measurement points. For this particular FZP where the outer zones are etched away. As mentioned

before, this can be explained by the fact that the amplitude of the acoustic signal on the FZP is controlled by size of the central zones.

5.2. Measuring signals Near the tip

In the next step we perform measurements near the AFM tip. The main objective to do this is to estimate the position of the tip by studying the variation of the first echo signal around it. As shown in Fig. 5.5, the pump beam is swept from the cantilever body to the tip with the same relative alignment. We find that the echo amplitude drops as we move closer to the tip and appears back when we are beyond the tip.

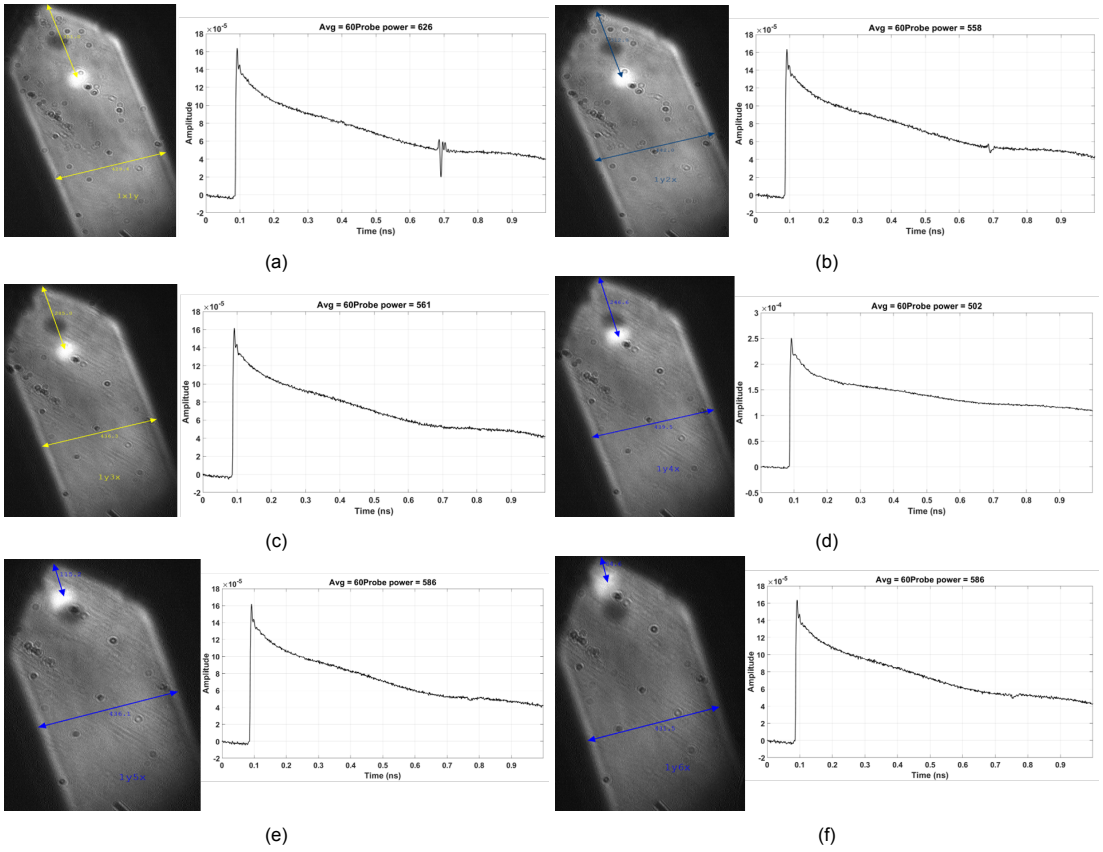

Figure 5.5: Sweeping pump-probe laser positions near the tip and finding the variation in the first echo signal. The camera images show the location of the pump-probe spot near the tip. The center of the tip is indicated by the position of the FZP, which is the dark spot on the cantilever body

The amplitude and time of acoustic echoes around the tip are compared in Fig. 5.6. Near the tip, part of the acoustic echoes get reflected from the intermediate etched region between the actual tip and the base, causing a reduction in signal amplitude. Furthermore because the intermediate region before the tip slopes downwards from the cantilever base, the part of the echoes are detected with a slight delay (few tens of ps). On the tip, the acoustic pulse undergoes loss in coherance due to phase changes from the reflections at the side of the tip, and therefore are not detected with a small pump and probe power. Beyond the tip the intermediate region slopes upwards to the thinner cantilever base, and therefore the echoes start arriving slightly earlier.

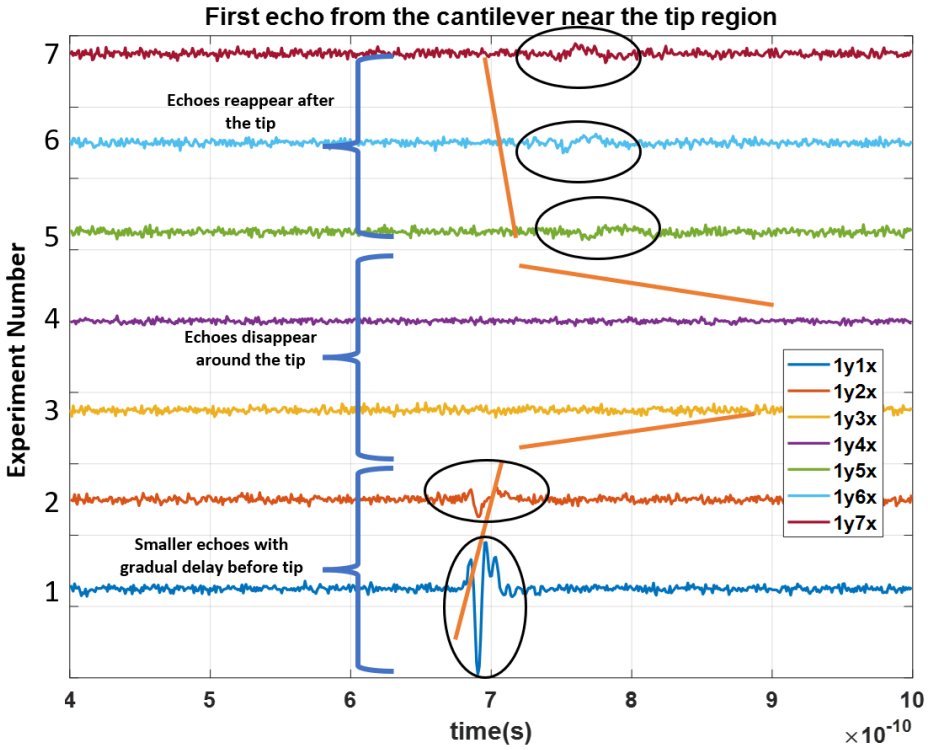

Figure 5.6: First echo signal variation near the tip. The legends indicate the numbers on the camera images in Fig. 5.5 corresponding to the position of the pump-probe spot with respect to the tip.

5.3. Signal Attenuation in AFM Cantilever

In this section, we study the damping of the acoustic signal as it traverses through the Si cantilever body. The ultrasonic attenuation of acoustic waves in crystalline Si at 300 k can be best described theoretically by phonon viscosity model put forward by Daly et al. [60, 61], under the approximation that the phonon velocity at this temperature is much smaller than the velocity at the frequency of the thermal phonons (50-80 Ghz in our case). The asymmetric shape of the acoustic echoes in Fig. 4.5 can be explained partly by the dispersion of the acoustic waves , which causes the higher frequency components components to come before the lower frequency components. The fact that we see the later echoes having a larger second part than the first part as compared the first echoes implies that the higher frequencies are attenuated for larger distance travelled inside the cantilever body. We can estimate the frequency dependent attenuation coefficient in Si directly from the measurements, using the fourier transform of the first 10 acoustic echoes (Fig. 5.7) detected on the cantilever body:

$$\alpha(f, d_i) = \frac{1}{d_i} \ln\left(\frac{|\Delta A_1(f)|}{|\Delta A_i(f)|}\right) \tag{5.1}$$

Where d is the round trip distance through the Si cantilever $(5\mu\mathrm{m})$, and $|\Delta A_i(\omega)|$ and $|\Delta R_1(\omega)|$ are the magnitudes of the Fourier transforms of the first and ith pulses. We should mention that this equation only takes into account the acoustic attenuation in Si and neglects the losses in the free surface or the interface between Al and Si. For estimating the attenuation coefficient α, we perform a linear regression fit of echo amplitudes for different frequencies at each height (Fig. 5.8). The main frequency range of the echo spectrum is selected between 0-140 Ghz to avoid the noise from the later echoes which are attenuated at higher frequencies.

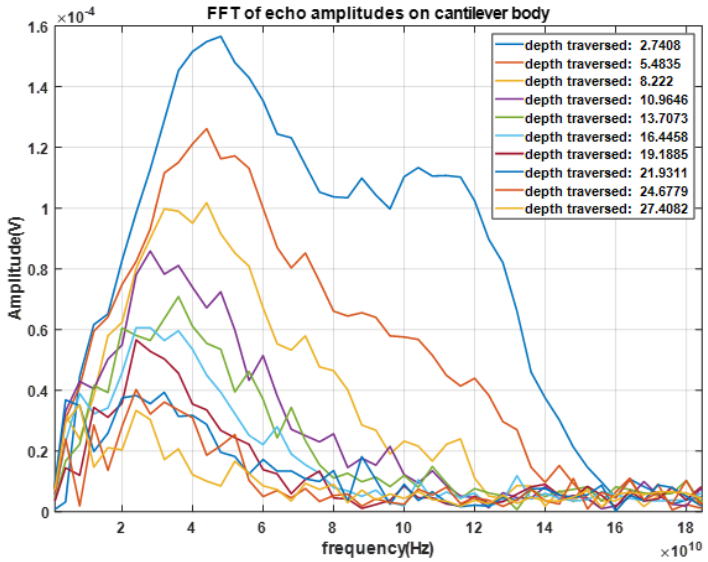

Figure 5.7: Frequency Spectrum of Acoustic Echoes on cantilever body at different depths traversed. The depth is equal half of the round trip distance

The calculated frequency dependent attenuation coefficient from the measurement is shown in Fig. 5.9. Despite some scatter within the data, the attenuation seems to have an increasing trend with frequency and is found to follow an approximately quadratic nature between frequency range 20-100 Ghz. This also agrees with the estimations of Daly et al., where the phonon damping is expected to follow a quadratic behaviour when $\omega\tau$ is approximately close 1 for propagation of acoustic waves in solids, where ω is the is the cycle frequency and τ is the pulse width of the acoustic wave.

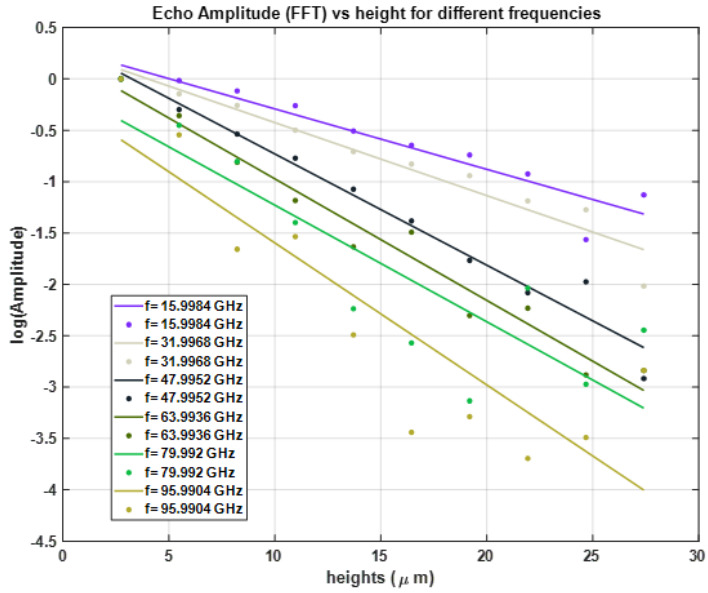

Figure 5.8: Logarithm of Echo amplitude vs distance traversed by the echoes for different frequencies. The data points are extracted from the spectrum of the acoustic echoes for different depths in Fig. 5.7

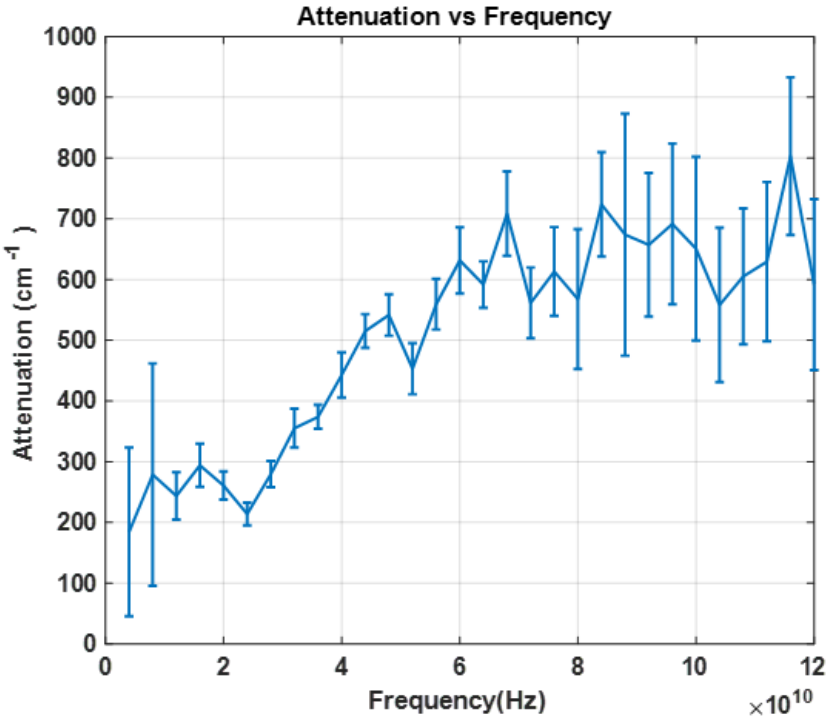

Figure 5.9: Estimated Attenuation coefficient vs frequency

However, we find that the α in our estimations is 4-5 times higher than the results of Daly et al. We expect that this huge shift could appear due to the improper adhesion between at the Al-Si interface. The finite interface stiffness from the imperfect adhesion causes more acoustic energy to reflect back within the Al layer, generating standing waves inside the film, which is indicated by the red circle in Fig. 5.10 . Lee et al.[62] showed that the reflection coefficient and interfacial stiffness at the coupling between material and substrate can be estimated from the amplitude and time constant of the damped oscillations. Here we extract the oscillations from the high-pass-filtered signals between 20-30 ps(blue circle in Fig. 5.10) and estimate the time constant and frequency of the breathing mode in Al. The reflection coefficient (R) at the Al-Si interface is calculated ([62, 63]) approximately around 13% as opposed 8% for perfect bonding between Al and Si. The ratio between two consecutive echoes is estimated to be 0.695 (in Fig 5.11), with attenuation α as 150cm^{-1} at 60Ghz in Si [61]. This is close to the ratio of the first and second echo measured in the setup with the new photodetector, which is also found to be 0.68. (Fig.4.7)

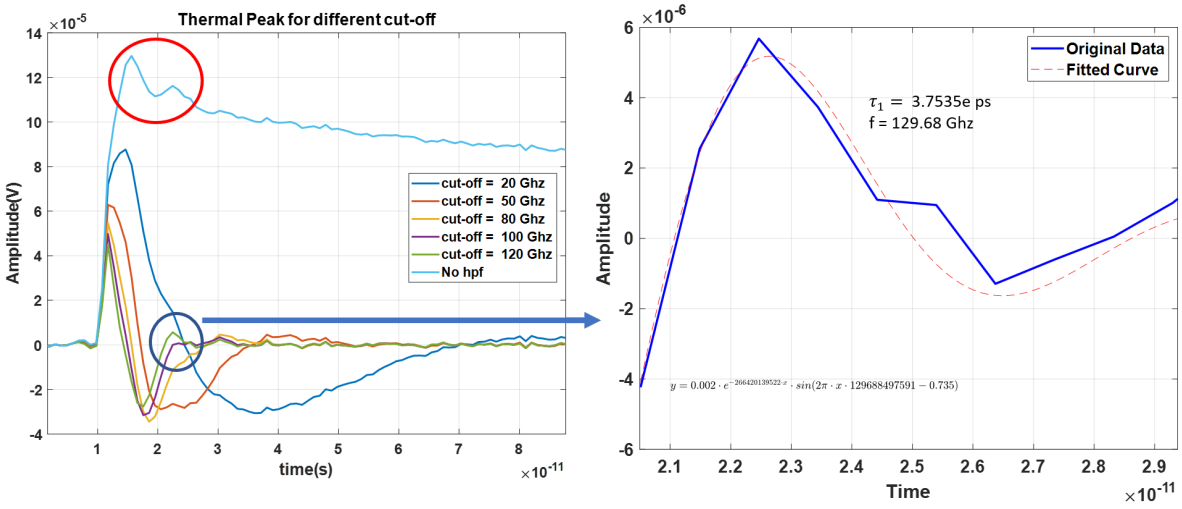

Figure 5.10: The right figure shows the actual thermal peak with oscillations from the standing waves in Al in the first 20ps (inside red circle).The damped oscillation component is extracted from the filtered thermal peak (blue circle) and fitted in the right figure

Although this difference in reflection coefficient is not very significant, it reduces amplitude of the acoustic waves by a factor of $(1-R)^2$ or 24% for every round trip distance in the cantilever body (Fig. 5.11). Hence after the 4^{th} or 5^{th} echo ($h \approx 10-13\mu m$, closer to the depth of the truncated tip), the acoustic amplitude will have already dropped to a factor 0.25-0.34 ($(1-R)^8-(1-R)^{10}$) because of the reflection. This additional loss factor is not expected in the truncated tip, where the acoustic wave only undergoes 1 round trip from the base to the tip and back.

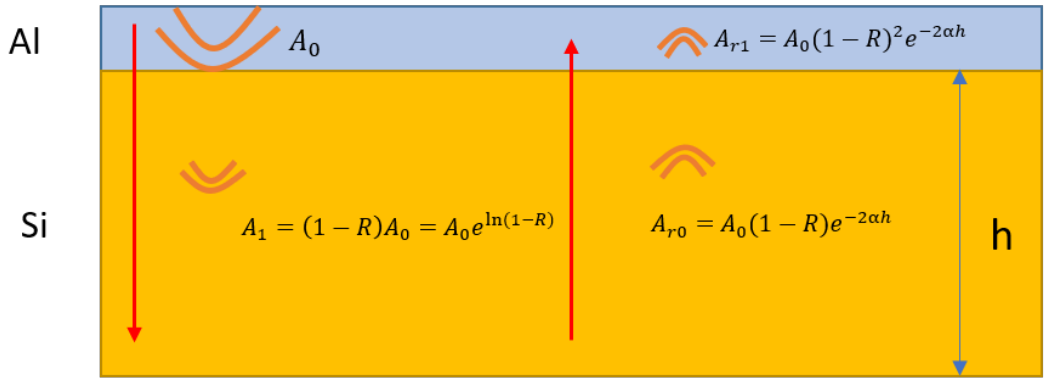

Figure 5.11: Losses in the acoustic echo amplitude due to reflections in the Al-Si interface and the attenuation inside the Si layer of thickness h . The effective loss factor between two consecutive echoes (A_{r1} and A_0) is a function of reflection coefficient (R) and attenuation coefficient α

6

Discussions and Outlook

In this chapter we provide a brief discussion and assessment on the modelling, fabrication and experimental work in this project. First we attempt to explain the the differences between the experimental and simulated results on the cantilever body, followed by the expected signal from the tip. Thereafter we discuss some of the challenges encountered during fabrication. Finally we give a short overview on the future scope of this project and possible improvement in designing ultrasound focusing devices on the AFM cantilevers.

6.1. Discrepancies in measurement and simulation on the cantilever body

From the measurements on the cantilever body in section 5.1 we find that the normalised reflectometry ratio on and off the FZP is around 30% higher than that the numerical results (Figures 5.4a and 5.4b). We hypothesize that the Si zones on the FZP could be contributing to the total reflectometry signal. This is neglected in the simulations as we probe only the volume of the Al zones to estimate the strain integral for the reflectometry signal.2.4 In order to assess the contribution of the acoustic strain in both Al and Si, we investigate the full reflectometry expression as derived by Matsuda et al. [17], as follows

$$\delta R(t) = \int_0^\infty f(z)\eta(z,t)dz,$$
$$\text{where } f(z) = f_0\left[\frac{dn}{d\eta}\sin\left(\frac{4\pi nz}{\lambda} - \psi\right) + \frac{d\kappa}{d\eta}\cos\left(\frac{4\pi nz}{\lambda} - \psi\right)\right]e^{-\frac{z}{\varepsilon}}, \tag{6.1}$$
$$f_0 = 8\frac{\omega\left[n^2\left(n^2+\kappa^2-1\right)+\kappa^2\left(n^2+\kappa^2+1\right)\right]^{1/2}}{c\left[(n+1)^2+\kappa^2\right]} \text{ and } \tan\psi = \frac{\kappa\left(n^2+\kappa^2+1\right)}{n\left(n^2+\kappa^2-1\right)}$$

where n and κ are the real and imaginary parts of the refractive index respectively. The real an imaginary part of the photoelastic constant is estimated from the photoelastic tensor component P_{12} as

$$\frac{d\tilde{n}}{d\eta} = \left(\frac{dn}{d\eta} + i\frac{d\kappa}{d\eta}\right) = \frac{P_{12}}{2\tilde{n}}, \text{ where } \tilde{n} = n + i\kappa \tag{6.2}$$

For the FZPs, the effective reflectometry depends on both the changes in reflectivity of Al and Si zones, and can be estimated separately for both these materials from eq. 6.1. Additionally, for the detection the change in the reflected probe laser power should also depend on the reflection coefficients of Al and Si at the probe wavelength, and hence the total detected signal on the FZP can be gived by the following weighted sum:

$$\delta R_{fzp}(t) = r_{Al} * \delta R_{Al}(t) + r_{Si} * \delta R_{Si}(t) \tag{6.3}$$

where r_{Al}, δR_{Al} and r_{Si}, δR_{Si} are the reflection coefficients and changes in reflectivity (from eq. 6.1) in the Al and Si zones respectively. The prefactor f_0 for Al and Si are around 60 and 40 respectively and the reflection coefficient at the probe laser wavelength is 87.5% and 30.30% respectively. Hence the

signal from the Si may still have a finite contribution to the total signal, and might explain the difference in the trends in simulation and measurement results.

6.2. Expected signal from the tip

From the measurements on the cantilever body with the new photodetector, we expect to find a visible signal on the tip upto truncation depths of approximately 11 μm, which corresponds to the scaled 4^{th} echo on the cantilever body (section 4.2.2). However as discussed in section 5.3, the losses in the acoustic signal on the cantilever body is a combined effect of ultrasonic attenuation in Si and reflection due to interfacial stiffness between Al and Si. Because of the latter effect the signal drops by an additional 25% for every round trip of the acoustic wave through the cantilever thickness, leading to almost 60% drop till the 4^{th} echo. Since the first echo on the trip only crosses the Al-Si interface twice in 1 round trip, that the scaled echo amplitude at the truncated tip in Fig 6.1a maybe an underestimation. By applying the correction factor for 1 round trip (Fig. 6.1b), we find that the estimated first echo amplitude almost doubles at 11 μm truncation and becomes higher than the noise level at 13.7 μm. Therefore we might see a higher signal on the tip than we expect if our hypothesis for imperfect adhesion between the Al-Si interface is true.

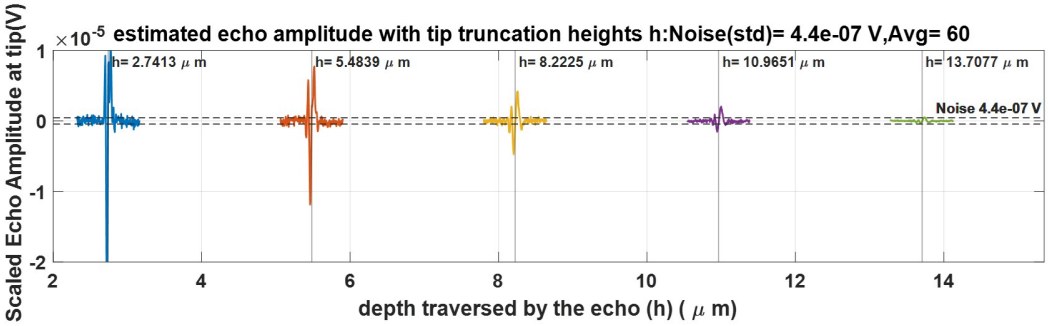

(a) Estimated echo amplitudes at the tip from the measured echoes on the cantilever body

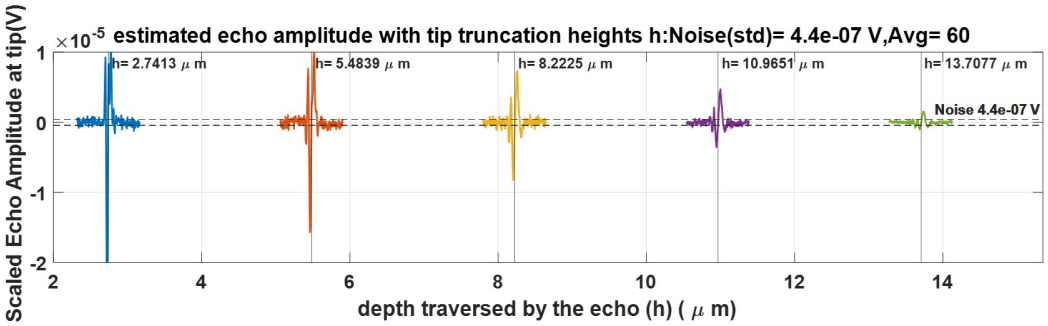

(b) Corrected first echo amplitudes, considering that it makes 1 round trip at the tip

Figure 6.1: a) First echo at the tip for different truncation depths, scaled from the measured echos on the cantilever body. The scaling (eq. 2.6) is applied on the measured echoes that has undergone additional transmission losses at the Al-Si interface by a factor $(1-R)^{2(i-1)}$ for the i^{th} echo. b) Corrected first echo amplitudes for 1 round trip at the tip, correction factor being $1/(1-R)^{2(i-1)}$ for the i^{th} echo in a)

6.3. General differences in Modelling and Experiment

In this section we briefly discuss some assumptions or general differences between the computational models and measurements.

- **The tip is not axisymmetric as assumed in the simulations.** In reality, the AFM tip has a pyramidal cross section, hence the reflections of edges of the circular acoustic spot from the sides of the tip might be slightly different than predicted. However we assume that if the surface area of the tip is slightly more than the axisymmetric tip for the same truncation height, there should not be a significant difference in relfectometry signal due to this effect.

- **Central frequency of the acoustic pulses is 50 Ghz. However the FZPs designed for 80 Ghz.** Although the spectrum of the detected acoustic pulses have a finite range between 10-160 Ghz, the peak frequency of the first echo from most of the measurements is found to be between 50-60 Ghz. For later echos this is lesser since the higher frequencies are attenuated more. However the simulations assume that the acoustic pulse is a symmetric Gaussian in time with a central frequency close to half the total spectrum, hence the FZPs were designed to focus a frequency of 80 Ghz or 105nm wavelength in Si. Simulations shows that the focal depth almost shifts by 550-700nm (70-80 ps is Si) if the presently designed FZP is used to focus an acoustic pulse of 50Ghz peak frequency (Fig. 6.2a) with the same pulse duration (approximately 45ps). If the tip is truncated to the focal depth of these FZPs at 80Ghz, the reflectometry signal seems to drop by a factor 1.3-1.5 with 50Ghz excitation, because the tip is out-of-focus (Fig. 6.2b). Hence the peak frequency of the acoustic pulses should be carefully taken into consideration for future FZP designs.

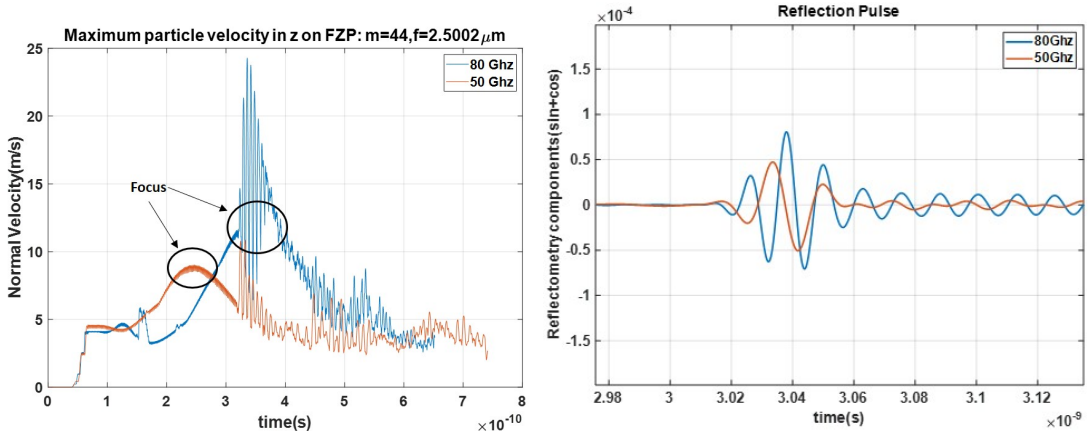

(a) Shift in maximum particle velocity at the central axis, implying shift in focus

(b) Drop in reflectometry signal amplitude with 50 GHz excitation for 12.7 μm tip truncation

Figure 6.2: a)Shift in focus and reduction in b)Reflectometry signal amplitude when FZPs designed for 80Ghz in Si are used to focus acoustic waves of 50 Ghz central frequency on

- **Damping of acoustic pulse in Si and effect of improper adhesion at the Al-Si interface.** The ultrasonic attenuation in Si and reflection coefficient at the Al-Si interface are estimated from measurements, and not included in the simulations.

6.4. Challenges in fabrication

Here we discuss some of the issues that were encountered during the fabrication process and possible measures to overcomes them in the future.

- **Angle on the truncated tip:** The AFM tip has an angle when truncated from the front, because of deflection of the ions at the back surface of the charged tip during fabrication. (Fig. 6.3a). The angular tip causes a shift in reflected acoustic spot at the base of the cantilever, which is roughly estimated in Fig. 6.3b We have estimated on the cantilever body that the thermal peak drops by upto 10-15% for a relative offset of 2 μm between the pump and probe spot. Although this reduction is not very significant, the signal may still be optimised by aligning the probe at an offset backward to compensate for the angle. Since the current setup configuration does not easily allow for moving the probe spot, this alignment can only be achieved by moving the sample and the pump spot by the same distance. In order to achieve this conveniently with the piezo controller on the Dichroic mirror, we have calibrated the number of steps required of the pump spot with the forward and reverse displacement in x and y axes. This shown in Appendix Section A.5

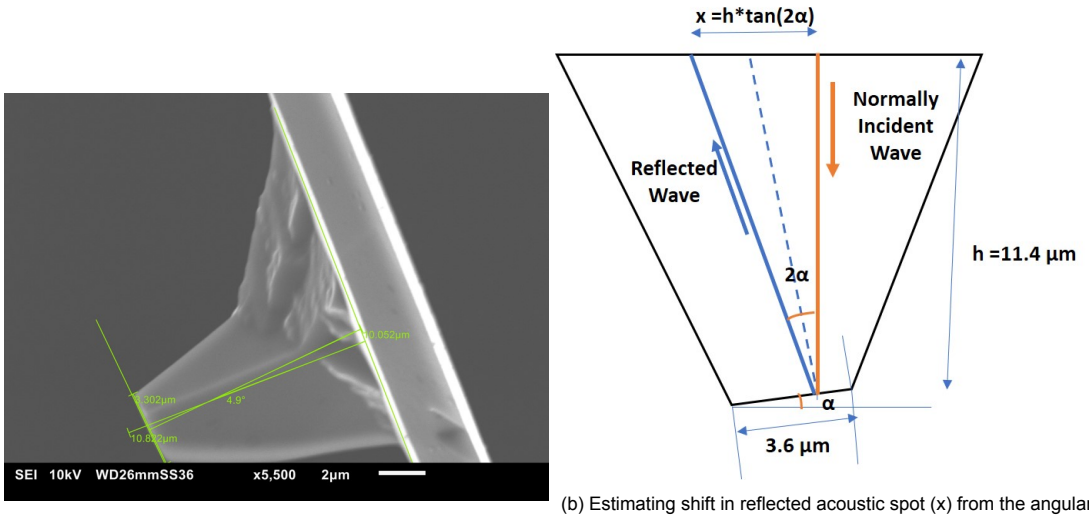

(a) SEM image of the tip from the side view

(b) Estimating shift in reflected acoustic spot (x) from the angular tip of height h

Figure 6.3: Shift in the reflected acoustic pulses due to angle at the tip. For 5° incline at the tip, the acoustic spot shifts by almost 2 μm

- **Cantilevers do not have the same total height.** Although most of them are between 17-17.7 μm, some might have a 2-3 μm larger. The tip area in that case would be larger than the one used for the simulation for the same focal depth, leading to some discrepancies between measurement and simulation.

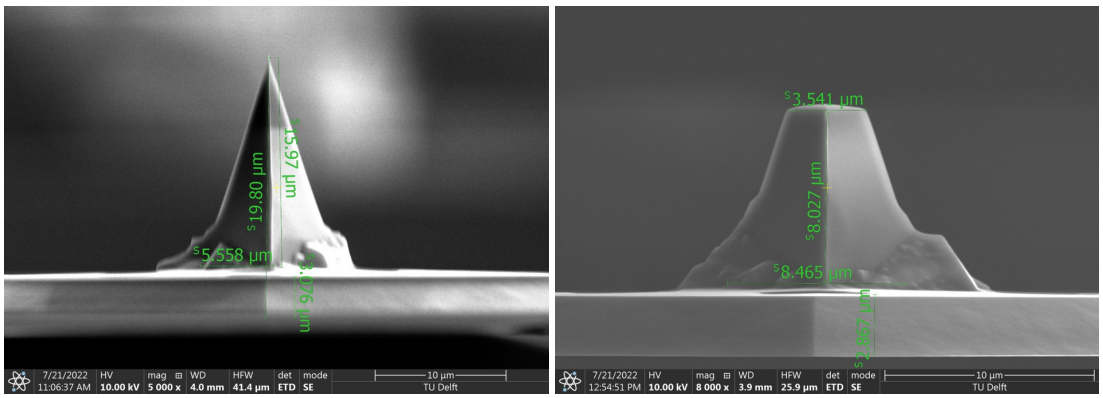

(a) AFM tip with longer heights

(b) Truncated tip with longer base height

Figure 6.4: SEM images of longer AFM tips and thicker cantilever body

- **Drift of the cantilever while imaging and milling** We observe this mainly while making the markers on the body where a current of 1nA is used. Also for some samples while making the FZPs this problem is found even at lower currents like 30pA. This causes an offset in relative position of the zones as well as edge defects on the zones which becomes more pronounced with longer milling times. This is caused by charging of the cantilever with the ion current, leading to displacement of the cantilever because of electrostatic repulsion. It is advisable to use a lower current of 10pA and a higher penetration depth of 140-160nm for fabricating the FZPs, or using a lower milling time. Since this problem is also found while using the SEM at higher current or larger magnification(6.5), it is also advisable to pause continuous SEM imaging while patterning with the ion beam. The drifting can also occur if the glue used to hold the cantilever weakens over time, causing cantilever to displace under gravity or under the force of the electrons in the SEM or the ion current. In that case it is advisable to use silver paste (conductive adhesive) for gluing or a new double sided tape before every session.

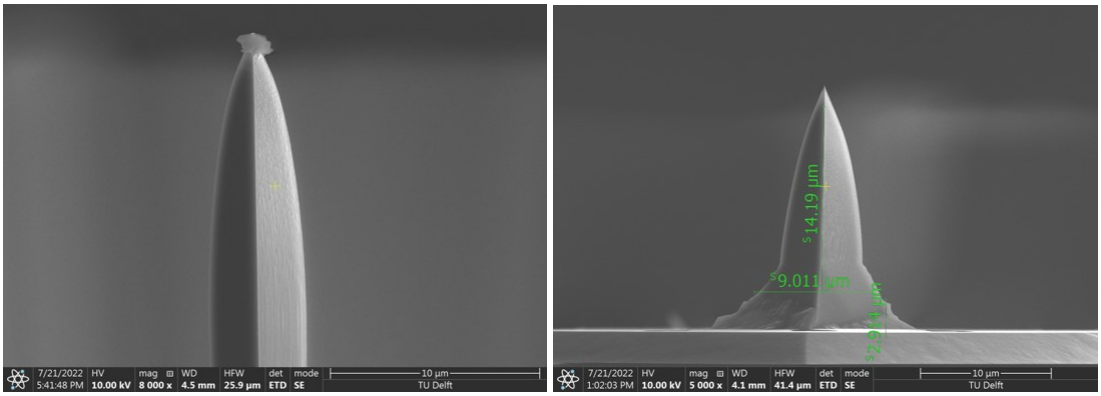

Figure 6.5: Distorted SEM images on tip due to drifting of the cantilever tip

- **Overtruncation due to higher current**: For larger truncation depths, a higher current of 4nA removes more material from the tip in the first stage that the target truncation depth (Fig. 6.6). Furthermore, since the scanning area of the ion beam is set for a smaller tip area, only a small energy from the ion beam can reach the edges of the increased tip area. This explains the presence of sharp ”horns” on the sides due to overtruncation. This can be avoided by localising the large current on a smaller scanning area or removing layers of materials in small steps, starting with at least 2.5 μm more than the target truncation depth. This avoids overtruncation as well as creates much smoother tip surface, as shown in Fig. 6.7

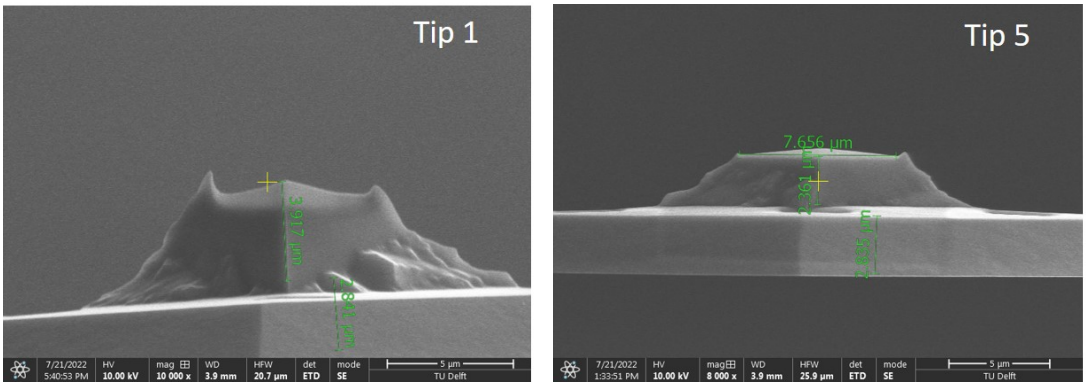

Figure 6.6: Overtruncation of tip for larger truncation depths. Ion Current is set at 4nA to remove more material first stage and 1nA for the second stage to remove remaining material

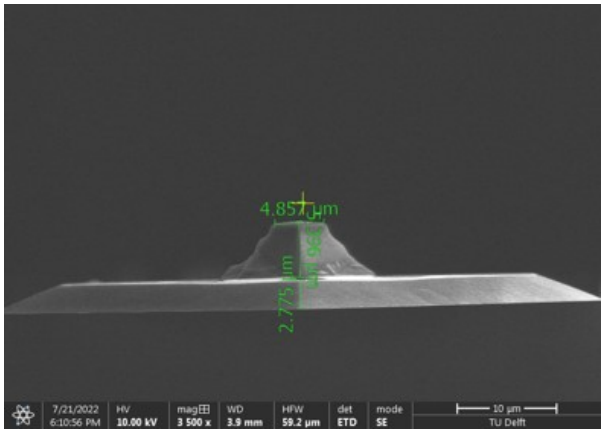

Figure 6.7: Tip at correct truncation depth with smoother surface by removing small layers of material in 2-3 stages. Current is 4nA for the first stage and 1-4nA for last stage

6.5. Outlook: Scope of Future work

Here we present the future scope for designing acoustic lenses to focus Ghz Ultrasound in AFM cantilever tip. These mostly include further experiments and possible techniques to optimise the design of the FZPs for improving signal at the tip

- **Measurements on the tip :** Firstly we are yet to measure the reflectometry signal on the newly truncated tips. We have fabricated tips with truncation depths 5.1, 6.5, 8.1 and 11.2 μm respectively, and fabricated an FZP on another sample with the last truncation depth. We will perform measurements on these samples with the improved setup and new photodetector in the future, and on obtaining a signal, attempt to compare with the results of Bryner et al. For the next step, it may be possible to truncate tips and fabricate FZPs at same or higher focal depths to proof the focusing capabilities as shown in Fig. 2.16b and Fig. 2.16a.

- **Difference in spot size between pump and aperture size of FZPs:** From the results on the cantilever body in section 5.1, we find that the improper FZP of f=2t with has smoother central zones but no outer zones follows a more consistent trend than the FZP of the same design with all zones fabricated, but with irregular edges due to smaller ion current. Hence we infer that the variation of reflectometry signal amplitude on the cantilever body is mainly governed by the size and shape of the central zones. In order to make the focusing from the outer zones contribute more to the signal amplitude, we can increase the pump laser spot size or reduce the size of the FZP. However, in either case we are unable to focus part of the acoustic energy that is generated outside the FZP. Hence it is required to optimise relative spot sizes of the pump with respect to the FZP to gain maximum signal amplitude due to focusing.

- **Phase Reversal FZP fabrication:** For the present study, we model and fabricate Soret FZPs which have alternate positive (Al) and negative (Si) zones, therefore only one half of the total area zones contribute to generating the acoustic waves and detecting majority of the reflectometry signal. Instead, Phase Reversal FZPs [40, 41] can be designed, where acoustic waves are generated on two layers of Al zones. The separation gap between each pair of zones induces a phase shift of π between waves diffracted from these layers, in order to have constructive interference at focus. Hence it is possible to obtain twice as high generation and detect larger reflectometry signal with the probe laser, because of the higher reflection coefficient of Al zones. However the fabrication of these kind of FZPs at nanometer resolution is challenging, as it would require sputtering Al on Si cantilever thickness (few 10s of nm) and FIB milling the the zones to the optimum thickness for best focusing.

- **Achromatic Lensing**: Since we generate a wideband acoustic pulse, it can be useful to focus the wavelengths corresponding to discrete frequencies in the spectrum. Guang et al. and Wang et al. [64, 65] designed Achromatic Plates by combining multiple FZP zonal plates with 5-6 focusing wavelengths near the central maximum frequency. This can also be implemented for the present work to optimise the focusing performance of FZPs over a wider range of frequencies and improving the detected signal at the tip.

- **Super-Oscillating Acoustic Lenses**: The Super-Oscillatory Acoustic Lensing, as introduced in section 1.2, is one of the most efficient and effective techniques for focusing of acoustic waves at subwavelength scales. The principle of SOAL is to oscillate the acoustic wave many times faster (theoretically 5-10 times) than the faster Fourier frequency near the center of the Gaussian spot. The results of Hyun et al. [32] achieved subwavelength focusing of $\lambda/6$ at mm scale in fluids with this technique. In principle SOAL can be achieved by optimising the size of the binary rings of the FZP to vary the phase and amplitude of the diffracted acoustic waves. However the implementation of the optimisation algorithm with commercial time-explicit solvers for elastic waves in solids is found to be computationally intensive and time consuming. Furthermore, implementation of gradient based algorithms on the transient analytical Rayleigh Somerfeld model (2.2) did not reach an optimum design in the timeframe of the project. Other algorithms like Method of Moving Asymptotes could be applied as future research [66]. Furthermore, random methods like Genetic Algorithm or Particle Swarm Algorithm [28] could be investigated for better computational efficiency with acceptable discretisation of the design domain. Other derivative-free methods

like Bayesian Optimisation, which uses Machine Learning models, could also be implemented to achieve optimum design parameters.

7

Conclusion

In this research, we modeled and designed AFM cantilever tips with acoustic lensing feature based on Fresnel Zonal Plate theory. Using numerical models with time-explicit discontinuous Galerkin algorithm, we showed that the optimum focusing capabilities with FZP in anisotropic Si is around 300-400nm resolution (FWHM), which is of the order of wavelength of the acoustic pulse. Consequently, we estimated a gain factor of 5-6 in the detected acoustic signal with focusing on truncated AFM tips. With Focused Ion Beam Milling, we fabricated FZP structures on an AFM cantilever body to experimentally study the variation in detected acoustic signal on FZPs of different focal depths, and verify the simulation results. From the acoustic echos measured on the cantilever body without the FZP, we also estimated the maximum truncation height where we can expect to measure a signal over the noise level, which is around 10-12 μm and tip size of 3.3-3.5 μm. Using these estimations we truncated the AFM tips with the FIB, and fabricate FZPs opposite the tip to experimentally study the focusing capabilities in the tip and verified with simulations. However we would first like to measure a signal from the truncated AFM tips without focusing, to compare with the results of Bryner et al. [21] In this regard, we increased the pump power density on the sample by moving the pump collimator position in the setup such that pump beam looses minimum power by crossing less optical components. To detect the signal with larger probe power density and smaller measurement noise, we installed the DET10A2 unamplified photodetector with higher optical saturation limit than the old photodetector. Because of these improvements we can now expect to have an improved SNR to detect a signal at the tip upto 11 μm truncation depth without the FZPs and even higher with FZPs. Furthermore we discovered that the losses in the acoustic echoes on the cantilever body not only comes from the ultrasonic damping in Si, but is also due to the imperfect adhesion at the Al-Si interface. The latter effect induces an additional loss factor of roughly 24% with every round trip of the acoustic echo on the cantilever body, but because there is only one round trip on the tip, the transmission loss at the interface will take place only once there. Hence we can expect to detect a higher signal on the tip than we estimate from the echoes on the cantilever body. In the upcoming weeks, we will continue our experiments to measure a signal on the truncated tips and eventually attempt to measure on the on the Fresnel Lenses fabricated on these tips to prove their focusing capabilities of Ghz Ultrasound waves at a few hundreds of nm resolution.

Self-reflection

I briefly summarise the important lessons I have learnt throughout the course of this project and areas that could have been done better. Firstly I would like to convey that this project has been a valuable experience for me, from both scientific and non-scientific aspects of research. As a researcher, I am always aspired to work on novel and challenging fields on engineering micro and nanosystems that can benefit human society. Also I am interested in extending my research in developing new technology for Bio-medical imaging and diagnosis at micro and nanoscale, and therefore this project was a relevant experience for me. I have gained a lot of technical skills in computational modelling of Ghz acoustic lensing, fabrication at micro and nanoscale, and experiments, particularly working with optical and electronic components. I had a lot of exposure in planning, time management, and handling various challenges with every new steps taken. These experiences have further motivated me to pursue research in my future career.

I would also like to mention some important takeaways, and areas I think could have been improved. Firstly, the planning of the project could have been more efficient. I spent a considerable amount of time to find an optimum design for the Acoustic lenses. This required extensive research on different Optimisation algorithms and computationally intensive inverse design calculations, and eventually I didn't reach a feasible solution within the fabrication limits. I think that with more time and better tuning of hyper-parameters, it might still be possible to push the conventional Fresnel lenses to focus smaller resolution. Instead it would have been better to focus more on the fabrication and experimental realisation of focusing capabilities of FZP on different truncated tip geometries. Hopefully I can still do more of these measurements in the coming weeks, and eventually verify the improvement of acoustic signal from the tip with focusing. Furthermore I should also work on my stress management and tendency to overplan my research. My supervisors think I do a good job but I should have more confidence on myself and the ideas I come up with.

8

Acknowledgement

I would like to convey that this project wouldn't have been possible without the support from some very special people, whom I was lucky to have as my supervisors this year.

Gerard. You are not only a great supervisor, but also a really caring mentor and role model for me. I am inspired by your critical thinking skills and ability to address clearly the most important points in a few words. You are also an exceptional leader, and is capable of seeing the positive outcome from any situation, no matter how negative it is. Working under your supervision has been a privilege and a great learning opportunity for me, and has helped me improve myself as a researcher. I aspire to learn from your knowledge, leadership and organisational skills.

Martin. You have been the perfect mentor and an excellent support system for me. Despite your busy schedule, you have always found the time for the many weekly meetings and technical discussions we used to have. Outside meetings, you always supported me and helped me with my stress management. I really appreciate your honesty and caring nature, because of which I always felt free to open myself up to you about my thoughts and ideas. I also enjoyed the nice gatherings and trips you invited me after work or during the weekend, the dinners at your place and the philosophical discussions we used to have. I will always remember your kindness, the same way we remember your marked spots in the department with your tea ;).

Ruben. You have been more like a friend than a supervisor. Thank you for your kindness, positivity and patience in putting up with me. Even though we don't always agree with each other, I really admire your experimental skills and enjoy the technical discussions we have both inside and outside of work. I hope we can continue to work together after my graduation, and find good measurements on the tip for our future publication.

I would like to thank my supervisors from ASML, **Umit Arabul** and **Zili Zhou**, for their technical discussions and valuable feedback during the meetings, which helped a lot in both the theoretical and experimental parts of the project. i would also like to thank my parents and my friends for their constant mental support during the project.

Thank you,
Gourab Chakraborty

Bibliography

[1] Milan Delor et al. “Imaging material functionality through three-dimensional nanoscale tracking of energy flow”. In: *Nature Materials* 19.1 (2020), pp. 56–62. ISSN: 14764660. DOI: 10.1038/s41563-019-0498-x. URL: http://dx.doi.org/10.1038/s41563-019-0498-x.

[2] Yongdeng Zhang et al. “Nanoscale subcellular architecture revealed by multicolor three-dimensional salvaged fluorescence imaging”. In: *Nature Methods* 17.2 (2020), pp. 225–231. ISSN: 15487105. DOI: 10.1038/s41592-019-0676-4. URL: http://dx.doi.org/10.1038/s41592-019-0676-4.

[3] Hossein J. Sharahi et al. “Acoustic subsurface-atomic force microscopy: Three-dimensional imaging at the nanoscale”. In: *Journal of Applied Physics* 129.3 (2021). ISSN: 10897550. DOI: 10.1063/5.0035151.

[4] David Maresca et al. “Nonlinear ultrasound imaging of nanoscale acoustic biomolecules”. In: *Applied Physics Letters* 110.7 (2017). ISSN: 00036951. DOI: 10.1063/1.4976105.

[5] Jessi E.S. Van Der Hoeven et al. “Bridging the gap: 3D real-space characterization of colloidal assemblies: Via FIB-SEM tomography”. In: *Nanoscale* 11.12 (2019), pp. 5304–5316. ISSN: 20403372. DOI: 10.1039/c8nr09753d.

[6] Camille Stavrakas et al. “Visualizing Buried Local Carrier Diffusion in Halide Perovskite Crystals via Two-Photon Microscopy”. In: *ACS Energy Letters* 5.1 (2020), pp. 117–123. ISSN: 23808195. DOI: 10.1021/acsenergylett.9b02244.

[7] Kaan Orhan. *Micro-computed Tomography (micro-CT) in Medicine and Engineering*. 2020. ISBN: 9783030166403. DOI: 10.1007/978-3-030-16641-0.

[8] Jeffrey Holzgrafe et al. “Nanoscale NMR Spectroscopy Using Nanodiamond Quantum Sensors”. In: *Physical Review Applied* 13.4 (2020), p. 1. ISSN: 23317019. DOI: 10.1103/PhysRevApplied.13.044004. URL: https://doi.org/10.1103/PhysRevApplied.13.044004.

[9] Jérémie Mathurin et al. “How to unravel the chemical structure and component localization of individual drug-loaded polymeric nanoparticles by using tapping AFM-IR”. In: *Analyst* 143.24 (2018), pp. 5940–5949. ISSN: 13645528. DOI: 10.1039/c8an01239c.

[10] Ji Xin Cheng and X. Sunney Xie. “Vibrational spectroscopic imaging of living systems: An emerging platform for biology and medicine”. In: *Science* 350.6264 (2015). ISSN: 10959203. DOI: 10.1126/science.aaa8870.

[11] L. Tetard et al. “Opto-nanomechanical spectroscopic material characterization”. In: *Nature Nanotechnology* 10.10 (2015), pp. 870–877. ISSN: 17483395. DOI: 10.1038/nnano.2015.168.

[12] Chengfu Ma and Walter Arnold. “Nanoscale ultrasonic subsurface imaging with atomic force microscopy”. In: *Journal of Applied Physics* 128.18 (2020). ISSN: 10897550. DOI: 10.1063/5.0019042.

[13] O. B. Wright and K. Kawashima. “Coherent phonon detection from ultrafast surface vibrations”. In: *Physical Review Letters* 69.11 (1992), pp. 1668–1671. ISSN: 00319007. DOI: 10.1103/PHYSREVLETT.69.1668.

[14] N. Chigarev et al. “Coherent phonon emission in the supersonic expansion of photoexcited electron-hole plasma in Ge”. In: *Physical Review B - Condensed Matter and Materials Physics* 61.23 (2000), pp. 15837–15840. ISSN: 1550235X. DOI: 10.1103/PHYSREVB.61.15837.

[15] O B Wright et al. “Ultrafast carrier diffusion in gallium arsenide probed with picosecond acoustic pulses”. In: (). DOI: 10.1103/PhysRevB.64.081202.

[16] O. Matsuda et al. “Acoustic phonon generation and detection in GaAs/Al 0.3Ga 0.7As quantum wells with picosecond laser pulses”. In: *Physical Review B - Condensed Matter and Materials Physics* 71.11 (Mar. 2005), p. 115330. ISSN: 10980121. DOI: 10.1103/PHYSREVB.71.115330/FIGURES/12/MEDIUM. URL: https://journals.aps.org/prb/abstract/10.1103/PhysRevB.71.115330.

[17] Osamu Matsuda et al. “Fundamentals of picosecond laser ultrasonics”. In: *Ultrasonics* 56 (Feb. 2015), pp. 3–20. ISSN: 0041624X. DOI: 10.1016/j.ultras.2014.06.005.

[18] W Nowacki. *Thermoelasticity*. 2013. URL: https://books.google.com/books?hl=en&lr=&id=muEgBQAAQBAJ&oi=fnd&pg=PP1&ots=hHwDk33XGD&sig=X59kP-krByOncrH1ahSe_ASWV7k.

[19] C Thomsen et al. *Surface generation and detection of phonons by picosecond light pulses*. Tech. rep. 6. 1986.

[20] Phillip Ahn et al. “Optical detection of ultrasound using an apertureless near-field scanning optical microscopy system”. In: *AIP Conference Proceedings* 1511.January 2013 (2013), pp. 360–366. ISSN: 15517616. DOI: 10.1063/1.4789070.

[21] J. Bryner et al. “Wave propagation in pyramidal tip-like structures with cubic material properties”. In: *Wave Motion* 47.1 (2010), pp. 33–44. ISSN: 01652125. DOI: 10.1016/j.wavemoti.2009.07.003.

[22] Jürg Bryner. “Applications of GHz Ultrasound Material Characterization and Wave Propagation in Microstructures”. In: (2009). DOI: 10.3929/ethz-a-005902021. URL: https://doi.org/10.3929/ethz-a-005902021.

[23] Nicholas Fang et al. “Sub-diffraction-limited optical imaging with a silver superlens”. In: *Science (New York, N.Y.)* 308.5721 (Apr. 2005), pp. 534–537. ISSN: 1095-9203. DOI: 10.1126/SCIENCE.1108759. URL: https://pubmed.ncbi.nlm.nih.gov/15845849/.

[24] M. V. Berry and S. Fishman. “Escaping superoscillations”. In: *Journal of Physics A: Mathematical and Theoretical* 51.2 (Dec. 2017), p. 025205. ISSN: 1751-8121. DOI: 10.1088/1751-8121/AA9B50. URL: https://iopscience.iop.org/article/10.1088/1751-8121/aa9b50%20https://iopscience.iop.org/article/10.1088/1751-8121/aa9b50/meta.

[25] Fu Min Huang et al. “Optical super-resolution through super-oscillations”. In: *Journal of Optics A: Pure and Applied Optics*. Vol. 9. 9. Sept. 2007. DOI: 10.1088/1464-4258/9/9/S01.

[26] G. Toraldo Di Francia. “Super-gain antennas and optical resolving power”. In: *Il Nuovo Cimento* 9.3 Supplement (1952), pp. 426–438. ISSN: 00296341. DOI: 10.1007/BF02903413.

[27] Paulo J.S.G. Ferreira and Achim Kempf. “Superoscillations: Faster than the Nyquist rate”. In: *IEEE Transactions on Signal Processing* 54.10 (2006), pp. 3732–3740. ISSN: 1053587X. DOI: 10.1109/TSP.2006.877642.

[28] Edward T.F. Rogers et al. “A super-oscillatory lens optical microscope for subwavelength imaging”. In: *Nature Materials* 11.5 (2012), pp. 432–435. ISSN: 14764660. DOI: 10.1038/nmat3280.

[29] J. Zhu et al. “A holey-structured metamaterial for acoustic deep-subwavelength imaging”. In: *Nature Physics* 7.1 (2011), pp. 52–55. ISSN: 17452481. DOI: 10.1038/nphys1804.

[30] Lucian Zigoneanu, Bogdan-ioan Popa, and Steven A Cummer. “Design and measurements of a broadband two-dimensional acoustic lens”. In: 024305.March (2011), pp. 1–5. DOI: 10.1103/PhysRevB.84.024305.

[31] Appl Phys. “Acoustic focusing by coiling up space”. In: 233508.November 2012 (2016). DOI: 10.1063/1.4769984.

[32] Jaeyub Hyun et al. “Realization of an ultrathin acoustic lens for subwavelength focusing in the megasonic range”. In: *Scientific Reports* 8.1 (Dec. 2018). ISSN: 20452322. DOI: 10.1038/s41598-018-27312-5.

[33] D W Schindel and A G Bashford. “Focussing of ultrasonic waves in air using a micromachined Fresnel zone-plate”. In: 35 (1997), pp. 275–285.

[34] Michael Z. Sleva, William D. Hunt, and Ronald D. Briggs. “Focusing performance of epoxy- and air-backed polyvinylidene fluoride Fresnel zone plates”. In: *Journal of the Acoustical Society of America* 96.3 (1994), pp. 1627–1633. ISSN: NA. DOI: 10.1121/1.410242.

[35] David C. Calvo et al. “Thin Fresnel zone plate lenses for focusing underwater sound”. In: *Applied Physics Letters* 107.1 (2015). ISSN: 00036951. DOI: 10.1063/1.4926607. URL: http://dx.doi.org/10.1063/1.4926607.

[36] Jiajun Zhao et al. “Manipulation of acoustic focusing with an active and configurable planar metasurface transducer”. In: *Scientific Reports* 4 (2014), pp. 1–6. ISSN: 20452322. DOI: 10.1038/srep06257.

[37] Sergio Pérez-López et al. “Transient Analysis of Fresnel Zone Plates for Ultrasound Focusing Applications.” In: *Sensors (Basel, Switzerland)* 20.23 (Nov. 2020), pp. 1–9. ISSN: 1424-8220. DOI: 10.3390/s20236824. URL: http://www.ncbi.nlm.nih.gov/pubmed/33260339%20http://www.pubmedcentral.nih.gov/articlerender.fcgi?artid=PMC7730605.

[38] John T Welter et al. “Focusing of longitudinal ultrasonic waves in air with an aperiodic flat lens”. In: 2789.2011 (2019). DOI: 10.1121/1.3640841.

[39] Appl Phys. “Acoustic Fresnel lenses with extraordinary transmission”. In: 114109.August 2014 (2016). DOI: 10.1063/1.4896276. URL: http://dx.doi.org/10.1063/1.4896276.

[40] Xiangxiang Xia et al. “Ultrasonic tunable focusing by a stretchable phase-reversal Fresnel zone plate”. In: *Applied Physics Letters* 117.2 (2020). ISSN: 00036951. DOI: 10.1063/5.0018663.

[41] Min Su et al. “High frequency focal transducer with a Fresnel zone plate for intravascular ultrasound”. In: *Applied Physics Letters* 119.14 (Oct. 2021), p. 143702. ISSN: 0003-6951. DOI: 10.1063/5.0070313. URL: https://aip.scitation.org/doi/10.1063/5.0070313.

[42] Daniel Tarrazó-serrano et al. “Acoustic Focusing Enhancement In Fresnel Zone Plate Lenses”. In: April (2019), pp. 1–10. DOI: 10.1038/s41598-019-43495-x.

[43] Rakesh G Mote et al. “Near-field focusing properties of zone plates in visible regime – New insights”. In: *Optics Express, Vol. 16, Issue 13, pp. 9554-9564* 16.13 (June 2008), pp. 9554–9564. ISSN: 1094-4087. DOI: 10.1364/OE.16.009554. URL: https://www-osapublishing-org.tudelft.idm.oclc.org/viewmedia.cfm?uri=oe-16-13-9554&seq=0&html=true%20https://www-osapublishing-org.tudelft.idm.oclc.org/abstract.cfm?uri=oe-16-13-9554%20https://www-osapublishing-org.tudelft.idm.oclc.org/oe/abstract.cfm?uri=oe-.

[44] Guofeng Zhang et al. “Investigation of axial and transverse focal spot sizes of Fresnel zone plates”. In: *Applied Optics, Vol. 56, Issue 13, pp. 3725-3729* 56.13 (May 2017), pp. 3725–3729. ISSN: 2155-3165. DOI: 10.1364/AO.56.003725. URL: https://www-osapublishing-org.tudelft.idm.oclc.org/viewmedia.cfm?uri=ao-56-13-3725&seq=0&html=true%20https://www-osapublishing-org.tudelft.idm.oclc.org/abstract.cfm?uri=ao-56-13-3725%20https://www-osapublishing-org.tudelft.idm.oclc.org/ao/abstract.cfm?uri=ao-.

[45] Qiang Liu et al. “Axial intensity distribution of a micro-Fresnel zone plate at an arbitrary numerical aperture”. In: *Optics Express* 29.8 (Apr. 2021), p. 12093. ISSN: 1094-4087. DOI: 10.1364/oe.419978.

[46] Mads Herring Jensen. *How to Simulate Elastic Waves in the Time Domain 2020 COMSOL*. Tech. rep.

[47] Yaoju Zhang and Chongwei Zheng. “Axial intensity distribution behind a Fresnel zone plate”. In: *Optics & Laser Technology* 37.1 (Feb. 2005), pp. 77–80. ISSN: 0030-3992. DOI: 10.1016/J.OPTLASTEC.2004.02.015.

[48] N. Chigarev, C. Rossignol, and B. Audoin. “Surface displacement measured by beam distortion detection technique: Application to picosecond ultrasonics”. In: *Review of Scientific Instruments* 77.11 (2006). ISSN: 00346748. DOI: 10.1063/1.2372739.

[49] *Document Connect*. URL: https://www.thermofisher.com/document-connect/document-connect.html?url=https%3A%2F%2Fassets.thermofisher.com%2FTFS-Assets%2FMSD%2FDatasheets%2FHelios-G4-PFIB-UXe-Materials-Science.pdf.

[50] David C Cox. "Focused ion beam". In: *Introduction to Focused Ion Beam Nanometrology* (2015), pp. 5–33. DOI: 10.1088/978-1-6817-4084-3ch2.

[51] Dieter M Profunser. *Laserbased Ultrasound for Characterization of Thin Films and Microstructures and Resulting Applications*. Tech. rep.

[52] Liwang Liu, Yannick Guillet, and Bertrand Audoin. "Common-path conoscopic interferometry for enhanced picosecond ultrasound detection". In: *Journal of Applied Physics* 123.17 (May 2018). ISSN: 10897550. DOI: 10.1063/1.5016279.

[53] T. Dekorsy et al. "Coherent acoustic phonons in nanostructures investigated by asynchronous optical sampling". In: *Nanophotonics for Communication: Materials, Devices, and Systems III* 6393.October 2006 (2006), 63930H. ISSN: 0277786X. DOI: 10.1117/12.687052.

[54] A. Bartels et al. "Ultrafast time-domain spectroscopy based on high-speed asynchronous optical sampling". In: *Review of Scientific Instruments* 78.3 (2007). ISSN: 00346748. DOI: 10.1063/1.2714048.

[55] *Periodic Waveform Analyzer | Zurich Instruments*. URL: https://www.zhinst.com/europe/en/periodic-waveform-analyzer.

[56] Haralambos Sarimveis et al. "A new algorithm for developing dynamic radial basis function neural network models based on genetic algorithms". In: *Computer Aided Chemical Engineering* 10.C (2002), pp. 949–954. ISSN: 15707946. DOI: 10.1016/S1570-7946(02)80186-9.

[57] *Radial Basis Neural Networks - MATLAB & Simulink - MathWorks Benelux*. URL: https://nl.mathworks.com/help/deeplearning/ug/radial-basis-neural-networks.html.

[58] Davide Chicco, Matthijs J. Warrens, and Giuseppe Jurman. "The coefficient of determination R-squared is more informative than SMAPE, MAE, MAPE, MSE and RMSE in regression analysis evaluation". In: *PeerJ Computer Science* 7 (2021), pp. 1–24. ISSN: 23765992. DOI: 10.7717/PEERJ-CS.623/SUPP-1. URL: /pmc/articles/PMC8279135/%20/pmc/articles/PMC8279135/?report=abstract%20https://www-ncbi-nlm-nih-gov.tudelft.idm.oclc.org/pmc/articles/PMC8279135/.

[59] Denis Constales et al. "Experimental Data Analysis". In: *Advanced Data Analysis & Modelling in Chemical Engineering* (2017), pp. 285–306. DOI: 10.1016/b978-0-444-59485-3.00009-6.

[60] Brian C Daly, Kwangu Kang, and David G Cahill. "Attenuation of Picosecond Ultrasonic Pulses in a thin Silicon Wafer". In: *1st Int. Symposium on Laser Ultrasonics: Science, Technology and Applications* (2008), p. 6.

[61] B. C. Daly et al. "Picosecond ultrasonic measurements of attenuation of longitudinal acoustic phonons in silicon". In: *Physical Review B - Condensed Matter and Materials Physics* 80.17 (2009). ISSN: 10980121. DOI: 10.1103/PhysRevB.80.174112.

[62] Martin Lee et al. "Self-Sealing Complex Oxide Resonators". In: *Nano Letters* 22.4 (2022), pp. 1475–1482. ISSN: 15306992. DOI: 10.1021/acs.nanolett.1c03498.

[63] Jake D.G. Greener et al. "High-Frequency Elastic Coupling at the Interface of van der Waals Nanolayers Imaged by Picosecond Ultrasonics". In: *ACS Nano* 13.10 (Oct. 2019), pp. 11530–11537. ISSN: 1936086X. DOI: 10.1021/ACSNANO.9B05052.

[64] Guang Hui Yuan, Edward TF Rogers, and Nikolay I. Zheludev. "Achromatic super-oscillatory lenses with sub-wavelength focusing". In: *Light: Science & Applications 2017 6:9* 6.9 (Mar. 2017), e17036–e17036. ISSN: 2047-7538. DOI: 10.1038/lsa.2017.36. URL: https://www.nature.com/articles/lsa201736.

[65] Jiayi Wang et al. "Topologically tuned terahertz confinement in a nonlinear photonic chip". In: *arXiv* (2021). DOI: 10.1038/s41377-022-00823-7.

[66] Krister Svanberg. “The method of moving asymptotes—a new method for structural optimization”. In: *International Journal for Numerical Methods in Engineering* 24.2 (1987), pp. 359–373. ISSN: 10970207. DOI: 10.1002/NME.1620240207.

[67] Baoguo Yuan, Ying Cheng, and Xiaojun Liu. “Conversion of sound radiation pattern via gradient acoustic metasurface with space-coiling structure”. In: *Applied Physics Express* 8 (2015), p. 27301. DOI: 10.7567/APEX.8.027301. URL: http://dx.doi.org/10.7567/APEX.8.027301.

[68] Tomás E. Gómez Álvarez-Arenas, Jorge Camacho, and Carlos Fritsch. “Passive focusing techniques for piezoelectric air-coupled ultrasonic transducers”. In: *Ultrasonics* 67 (Apr. 2016), pp. 85–93. ISSN: 1874-9968. DOI: 10.1016/J.ULTRAS.2016.01.001. URL: https://pubmed-ncbi-nlm-nih-gov.tudelft.idm.oclc.org/26799129/.

A

Appendix

A.1. Calculation of Important Focusing Parameters

The focal parameters introduced in section 2.2 are estimated from the numerical model as shown in Fig. A.1. The height of the cantilever is chosen such that the reflections from the boundary takes place beyond the pre-estimated focal depth. Because of the Gaussian excitation, radial pressure distribution of the propagating wavefront at any instant has a maximum at the central line, which can plotted over time as the bottom left plot. The maximum of this profile (without the interference due to reflection) gives time of focus, denoted by $\mathrm{t}(\mathrm{P_{max}})$. The pressure Envelope along the axial (z) direction, shown in the bottom right plot then gives the focal depth $\mathrm{f}(\mathrm{P_{max}})$. From the pressure envelope the tail-width parameter can also be calculated as the Full Width Half Maximum (FWHM) denoted by $\mathrm{W_{full}}$. The leftward skewness of this envelope is due to the diffraction of the acoustic pulses from the outer Fresnel zones and due to the delay in arrival at the centre [37], leading to elongation of the main wavefront. Hence the Half Pressure Half Width of the longer tail ($\mathrm{W_{half}}$) could also be and important parameter in quantifying the axial tail width.

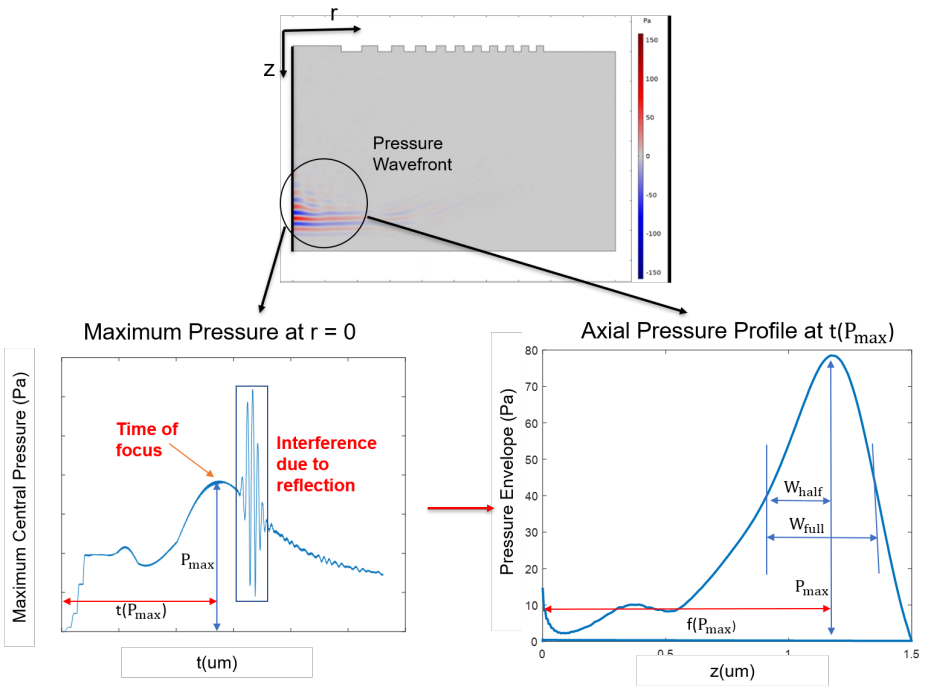

Figure A.1: Calculation of focusing parameters

A.2. Comparison of Focusing Behaviour from previous acoustic lens studies

In this section, a review of focusing characteristics in previous planar acoustic lens designs is presented. The lateral resolutions (FWHM) is obtained in terms of wavelength at KHz frequency range by previous Acoustic Lens designs . It is found that the acoustic lens with extraordinary transmission designed by Moleron et al. [39] and the meta-surface based space-coiled structure of Yuan et al. [67] (marked in yellow) obtained some of the smallest FWHM. However those designs were based on very low operational frequency range and the feasibility of fabrication similar lens configuration with nanometer feature size at GHz frequency range might be an issue. Furthermore the focal depth is much smaller compared to the aperture size (radius of the source transducer) for these configurations, whereas for the present work, the focusing should take place at a truncated cantilever tip whose depth of the same order or a few μms higher than that the radius of the aperture. In contrast the optimized Super-Oscillatory Acoustic Lens (SOAL) by Hyun et al. [32] achieved one of the most optimum lateral resolutions, with comparable aperture size and focal depth. For the present work, numerical simulations show that conventional Soret-FZP patterns can focus ultrashort acoustic pulses around 180 nm inside Si, with a spot size of around 1.5λ, with the aperture radius and focal depth of the order of 4 μm and 3 μm respectively. Hence it is worth to further investigate optimised versions of these designs, and their effect on detection of reflected acoustic pulses at the cantilever base.

Reference	**Operational Medium**	**Operational Frequency (kHz)**	**Lens thickness (mm)**	**Radius of source transducer (mm)**	**Target Focal length (mm)**	**Achieved Lateral Resoulution**
D.W. Schindel (1997)[33]	air	580	0.125	8.14	7.5	1.36λ
T.E.G. AlvarezArenas (2016)[68]	air	400	0.1	15	33.5	2.91λ
J.T. Welter (2011)[38]	air	85	3	20	2.5	0.88λ
M. Moleren (2014)[39]	air	5.85	25	210	71	0.61λ
B. Yuan (2015) [67]	air	2	16	165	100	0.70λ
Y. Li(2014)[31]	air	0.82	47	675	1,400	1.20λ
M.Z. Sleva (1994)[34]	water	5,000	0.111	17.3	52	3.02λ
Hyun (2018)[32]	water	1,000	0.2	25	25	0.57λ

Table A.1: Review of focusing charecteristics of previous studies of planar acoustic lens

A.3. Uncertainty Analysis and error propagation

The funcational form of the RBF approximation, representing the fitted acoustic amplitude at each time point is given by:

$$\mathrm{f}(t_j, b_i, c_i, w_i) = b_0 + \sum_{i=1}^{5} b_i * e^{-\left((t_j - c_i)^2 * w_i^2\right)} \quad (t_j = t_1 : t_N \text{ are the time points}) \tag{A.1}$$

where b_i, c_i, w_i are represent the amplitude, input weights and spread parameters of the i^{th} neuron. The spread parameter is an input parameter which is optimised with respect to the standard error of the model with a linear regression analysis, and is treated as constant in this case. We calculate the corelation between the model parameters using the non-linear least squares method, which requires

the gradiant information of the model given by the Jacobian of the uncertainty parameters:

$$J_{j,i}(i=1-11)=\begin{cases}\frac{\partial f}{\partial b_i}=e^{-\left(\left(t_j-c_i\right)^2*w_i^2\right)}, i=1-5\\ \frac{\partial f}{\partial c_i}=-2b_i*e^{-\left(\left(t_j-c_i\right)^2*w_i^2\right)}*\left(\left(t_j-c_i\right)*w_i^2\right), i=6-10\\ \frac{\partial f}{\partial b_0}=1\ (b_0 \text{ is constant over all the rbfs })\end{cases} \tag{A.2}$$

The covariance matrix M can be estimated using Gauss-Newton Method and it's first order approximation is related to the Jacobian of the uncertainty parameters:

$$M^{(11\times 11)}=\left(J^T*J\right)^{-1}*se \tag{A.3}$$

where se is the standard error of the measurement noise. The standard error of the i^{th} model parameter is given by the ixi^{th}diagonal element of the Covariance Matrix.

Since we compare the ratio between the echo amplitudes with and without the FZP, the effective uncertainty is computed by error propagation of the model parameters associated with these two measurements. The peak-to-peak amplitude ratio is given by

$$r=\frac{f_{FZP}\left(t_{\max},b_i,c_i,w_i\right)-f_{FZP}\left(t_{\min},b_i,c_i,w_i\right)}{f_{noFZP}\left(t_{\max},b_i,c_i,w_i\right)-fnoFZP\left(t_{\min},b_i,c_i,w_i\right)} \tag{A.4}$$

where ($t_{\max}$ and $t_{\min}$ are the times for max and min signal) The propagated uncertainty of σ_r can be calculated as the root-mean-square-error over the parameter uncertainties with derivative weights:

$$\begin{aligned}\sigma_r^2=&\sum_{i=1}^{5}\left(\frac{\partial r}{\partial b_{i\_fzp}}\sigma_{b_{i\_fzp}}\right)^2+\sum_{i=1}^{5}\left(\frac{\partial r}{\partial c_{i\_FZP}}\sigma_{c_{i\_FZP}}\right)^2+\sum_{i=1}^{5}\left(\frac{\partial r}{\partial b_{0\_FZP}}\sigma_{b_{0\_FZP}}\right)^2+\\&\sum_{i=1}^{5}\left(\frac{\partial r}{\partial b_{i\_nofzp}}\sigma_{b_{i\_nofzp}}\right)^2+\sum_{i=1}^{5}\left(\frac{\partial r}{\partial c_{i\_noFZP}}\sigma_{c_{i\_noFZP}}\right)^2+\sum_{i=1}^{5}\left(\frac{\partial r}{\partial b_{0\_FZP}}\sigma_{b_{0\_noFZP}}\right)^2\end{aligned} \tag{A.5}$$

Here σ_{b_i}, σ_{c_i} and σ_{b_0} are the standard errors of the model parameters, which are the diagonal elements of the covariance matrix in eqn A.3. The derivatives of the amplitude can be calculated in terms of the Jacobian parameters in eqn A.2 with suitable prefactors, an example shown below as shown below:

$$\frac{\partial r}{\partial b_{i\_fzp}}=\frac{1}{f_{nofzp}\left(t_{\max},b_i,c_i,w_i\right)-f_{nofzp}\left(t_{\min},b_i,c_i,w_i\right)}*\left(\frac{\partial f_{\max fzp}}{\partial b_{i\_fzp}}+\frac{\partial f_{\max fzp}}{\partial b_{i\_fzp}}\right) \tag{A.6}$$

and

$$\frac{\partial f}{\partial b_{i\_nofzp}}=-\frac{f_{fzp}\left(t_{\max},b_i,c_i,w_i\right)-f_{fzp}\left(t_{\min},b_i,c_i,w_i\right)}{\left(f_{nofzp}\left(t_{\max},b_i,c_i,w_i\right)-f_{nofzp}\left(t_{\min},b_i,c_i,w_i\right)\right)^2}*\left(\frac{\partial f_{nofzp}}{\partial b_{i\_nofzp}}+\frac{\partial f_{nofzp}}{\partial b_{i\_nofzp}}\right) \tag{A.7}$$

A.4. Time-table for one Fabrication session

Operation	Time taken (mins) (rough estimation)
Height Measurement: • Placing the Cantilever on the holder • Venting the Chamber and placing the holder • Aligning cantilever + Height Measurement	Total :58 5 20 25+4(2) = 33
Alignment Markers • Venting out the chamber • Transferring the cantilever upside down (Broke 1 cantilever) + Pumping in • Aligning cantilever w.r.t Ion Beam (offsets position while changing current) • Making Markers + Moving to next one (alignment problems due to angle between two adjacent cantilevers)	Total: 131 15 20 +15 25 15+25+8+8 = 56
Truncation • Venting out the chamber • Transferring the cantilever upside down + Pumping in • Measuring total height for confirmation (aligning w.r.t SEM) • Aligning cantilever w.r.t Ion Beam • Truncating tip + Moving to next one (alignment problems due to angle between two adjacent cantilevers)	Total: 195 15 10+15 10 15 45+30+25+30 = 130
Making FZPs • Venting out the chamber +Rotating holder +pumping in • Aligning w.r.t Ion Beam + Aligning FZP centre w.r.t Marker • Making first FZP (wrong starting overlap) • Moving to the next sample (refocused because of previous problem) + making FZP	Total: 135 30 30 40 15+20 = 35

Figure A.2: Time-table for 1 Fabrication session involving all steps for truncation of AFM tips and patterning FZPs on tips. In this session, 4 tips were truncated and FZPs patterned on two of them.

A.5. Calibrating motion of pump spot with number of steps on the piezo-inertial motor on the dichroic mirror

Channel 1

Direction	Steps	Distance(Pix)	Distance(microns)	Least count(steps/pix)
+x	2000	153	19.16856	13.07189542
-x	2000	66	8.268793	30.3030303

Channel 2

Direction	Steps	Distance(Pix)	Distance(microns)	Least count(steps/pix)
+y	2000	118	14.78359909	16.94915254
-y	2000	85	10.64920273	23.52941176

Figure A.3: Calibrating the number of steps on the inertial motor with the distance moved by the pump spot on the sample. This is done by calculating the number of pixels moved by the pump spot on the camera in forward and reverse x and y. The calibration factor in the last column helps to correct for the backlash in the piezo-inertial motor during aligning

A.6. Ambitious timeline at the beginning of the project

- **M1**: Completed Optimised Design of Super-Oscillatory Acoustic Lens with understanding of Focusing Parameters, and numerically studied the effects of new design on sensitivity of probe beam measurement

- **M2.1**: Completed Fabrication of Preliminary Acoustic Lens with conventional FZP for first measurements
- **M2.2**: Completed Fabrication of Optimised SOAL and Alternative Designs of Fresnel Lens with SEM figures
- **M3.1**: Completed Experiments on Generation and Focusing of acoustic wave inside the AFM cantilever with conventional FZP and experimentally verified its effect on the probe beam sensitivity
- **M3.2**: Completed similar experiments as in M3.2 with final design, and verified with theory and simulations
- **M4**: Review and finish the Msc thesis and write our potential Publication Paper on this research

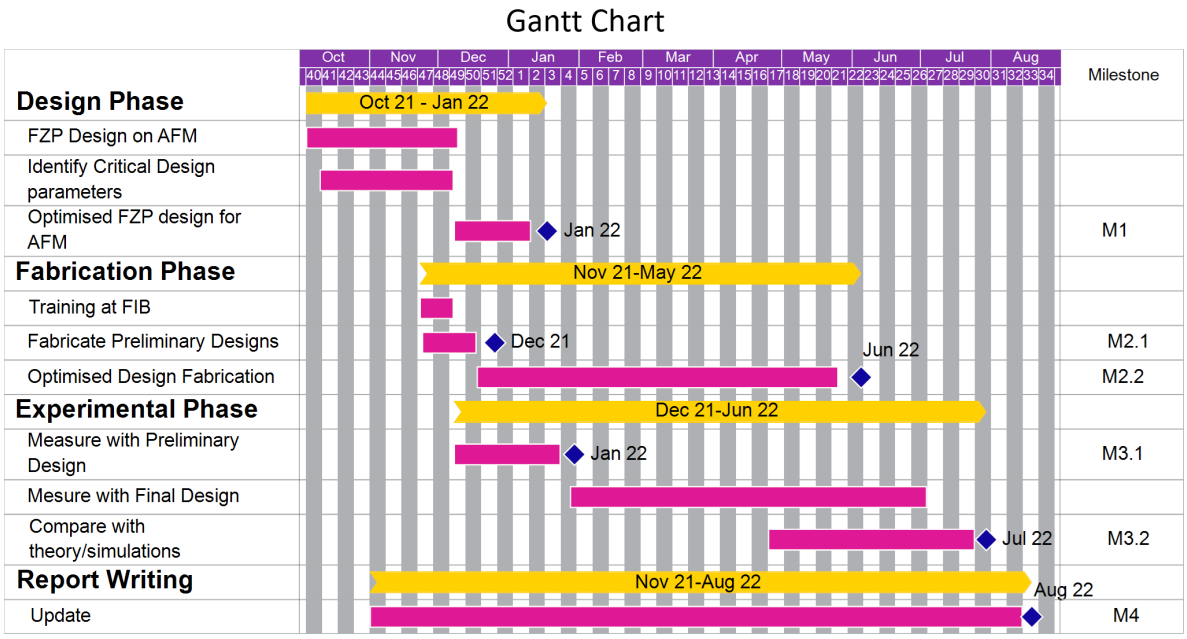

Figure A.4: Gantt Chart for Planning